

Search for displaced leptons in proton-proton collisions at  
 $\sqrt{s} = 13 \text{ TeV}$

Dissertation

Presented in Partial Fulfillment of the Requirements for the Degree  
Doctor of Philosophy in the Graduate School of The Ohio State  
University

By

Bryan Cardwell, B.S., M.S.

Graduate Program in Physics

The Ohio State University

2021

Dissertation Committee:

Christopher Hill, Advisor

Stanley Durkin

Linda Carpenter

Andrew Heckler

© Copyright by

Bryan Cardwell

2021

## Abstract

A search is presented for new long-lived particles that propagate a measurable distance through the CMS detector before decaying to leptons. The search is performed in  $113\text{--}118\text{ fb}^{-1}$  of proton-proton collision data produced by the CERN LHC at a center-of-mass energy of 13 TeV and collected by the CMS detector in 2016, 2017, and 2018. Events are selected with two leptons (an electron and a muon, two electrons, or two muons) that both have transverse impact parameter values between 0.01 cm and 10 cm. Using transverse impact parameter as the discriminating variable allows for sensitivity to displaced decays without requiring that the leptons form a common vertex. The search is designed to be sensitive to a wide range of new physics models that produce displaced di-lepton final states. The observation is consistent with the background-only hypothesis, and limits are set on the product of the cross-section of top squark pair production and the branching fraction to a lepton and a b or d quark through an R-parity-violating vertex. For a proper decay length hypothesis of 2 cm, top squarks with masses up 1500 GeV are excluded at the 95 % confidence level.

For Cristiana and Montague.

## Vita

2015 .....	B.S. Physics, North Central College
2015-2017 .....	Graduate Teaching Associate, The Ohio State University
2017 .....	M.S. Physics, The Ohio State University
2017-present .....	Graduate Research Associate, The Ohio State University

## Publications

### Research Publications

Included in author list of **FIXME** publications from CMS.

## Fields of Study

Major Field: Physics

## Table of Contents

	Page
Abstract . . . . .	ii
Dedication . . . . .	iii
Vita . . . . .	iv
List of Tables . . . . .	viii
List of Figures . . . . .	xi
1. Introduction . . . . .	1
1.1 The Standard Model . . . . .	2
1.1.1 Quantum chromodynamics . . . . .	4
1.1.2 The electroweak theory . . . . .	4
1.1.3 The Higgs mechanism . . . . .	5
1.1.4 Current status . . . . .	7
1.2 Beyond the Standard Model . . . . .	10
1.2.1 Supersymmetry . . . . .	10
1.2.2 Long-lived particles . . . . .	12
1.2.3 Displaced supersymmetry . . . . .	15
2. The Large Hadron Collider and Compact Muon Solenoid experiment . .	18
2.1 The Large Hadron Collider . . . . .	18
2.1.1 Injection chain . . . . .	19
2.1.2 Main ring . . . . .	20
2.2 The Compact Muon Solenoid experiment . . . . .	25
2.2.1 Solenoid magnet . . . . .	26
2.2.2 Tracker . . . . .	27

2.2.3	Electromagnetic calorimeter . . . . .	32
2.2.4	Hadronic calorimeter . . . . .	34
2.2.5	Muon system . . . . .	35
2.2.6	Trigger . . . . .	38
2.2.7	Physics object reconstruction . . . . .	38
3.	Search for displaced leptons . . . . .	43
3.1	Overview . . . . .	44
3.1.1	Long-lived particles at the LHC . . . . .	44
3.1.2	Displaced leptons signature . . . . .	46
3.1.3	Analysis strategy . . . . .	49
3.2	Data and simulated samples . . . . .	52
3.2.1	Experimental data . . . . .	52
3.2.2	Simulated background events . . . . .	52
3.2.3	Simulated signal events . . . . .	53
3.3	Event selection . . . . .	55
3.3.1	Triggers . . . . .	55
3.3.2	Preselection . . . . .	57
3.3.3	Prompt control region . . . . .	66
3.3.4	Inclusive signal region . . . . .	69
3.4	Corrections to simulation . . . . .	73
3.4.1	Event pileup . . . . .	73
3.4.2	Lepton ID . . . . .	73
3.4.3	Lepton $d_0$ resolution . . . . .	73
3.4.4	Trigger efficiency . . . . .	78
3.5	Background estimation . . . . .	80
3.5.1	Background sources . . . . .	80
3.5.2	Data-driven ABCD method . . . . .	82
3.5.3	Closure tests in control regions . . . . .	85
3.5.4	ABCD correction and systematic uncertainty . . . . .	87
3.5.5	Testing full background estimation procedure . . . . .	94
3.5.6	Additional background checks . . . . .	96
3.6	Systematic uncertainties . . . . .	102
3.6.1	Integrated luminosity . . . . .	102
3.6.2	Pileup . . . . .	102
3.6.3	Displaced tracking efficiency . . . . .	104
3.6.4	Trigger efficiency . . . . .	104
3.6.5	Lepton ID and isolation . . . . .	104
3.6.6	Muon pixel hit efficiency . . . . .	105
3.6.7	Lepton $d_0$ resolution . . . . .	106
3.7	Results . . . . .	107

3.7.1	Observed events . . . . .	107
3.7.2	Limits . . . . .	112
3.7.3	Additional likelihood tests . . . . .	116
4.	Conclusion . . . . .	120
Appendices		123
A.	Impact of APV25 saturation on displaced tracking . . . . .	123
B.	Poorly measured lepton $ d_0 $ at large $ \eta $ . . . . .	127
C.	Displaced tracking efficiency . . . . .	129
Bibliography . . . . .		138

## List of Tables

Table	Page
2.1 Luminosity parameters used in Eq. (2.1). . . . .	21
3.1 The $e\mu$ preselection criteria. The electron and muon $p_T$ thresholds increase in 2017 in accordance with the increased HLT electron and muon $p_T$ thresholds. . . . .	58
3.2 The $ee$ preselection criteria. The electron $p_T$ threshold increase in 2017 and 2018 in accordance with the increased HLT electron $p_T$ threshold. . . . .	59
3.3 The $\mu\mu$ preselection criteria. The muon $p_T$ threshold increase in 2017 and 2018 in accordance with the increased HLT muon $p_T$ threshold. . . . .	60
3.4 The electron tight ID requirements, which are identical to the tight cut-based ID from the CMS EGamma Physics Object Group with the $d_0$ and longitudinal impact parameter requirements removed. . . . .	61
3.5 The muon tight ID requirements, which are identical to the tight cut-based ID from the CMS Muon Physics Object Group with the requirements on $d_0$ and the longitudinal impact parameter removed. . . . .	62
3.6 The cumulative efficiency for simulated $\tilde{t}\bar{t} \rightarrow \bar{l}b\bar{l}b$ signal events to pass the 2018 inclusive signal region selection, for several choices of $\tilde{t}$ mass and $c\tau$ . The corrections described in Section 3.4 are applied. . . . .	72
3.7 The average $\sigma_{align}$ for electrons and muons, for the 2017 and 2018 analyses. . . . .	75
3.8 The unprescaled $p_T^{\text{miss}}$ triggers used to create an orthogonal data sample for the trigger efficiency calculation. . . . .	79

3.9 The $p_T$ boundaries between the low- and high- $p_T$ bins of SR I in each channel. . . . .	85
3.10 Closure test results in background simulation (with and without $Z \rightarrow \tau\tau \rightarrow ll$ events) and in data, in the 100–500 $\mu\text{m}$ region. The average extrapolated ratios and their statistical uncertainties are given. The A, B, C, and D regions are defined as follows: A is 20–30 $\mu\text{m}$ in prompt lepton $ d_0 $ and 20–100 $\mu\text{m}$ in displaced lepton $ d_0 $ , B is 20–30 $\mu\text{m}$ in prompt lepton $ d_0 $ and 100–500 $\mu\text{m}$ in displaced lepton $ d_0 $ , C is always 20–100 $\mu\text{m}$ in displaced lepton $ d_0 $ , D (the test region) is always 100–500 $\mu\text{m}$ in displaced lepton $ d_0 $ , and we perform repeated tests while simultaneously varying the C and D prompt lepton $ d_0 $ s within the 30–100 $\mu\text{m}$ range. . . . .	87
3.11 Closure test results in data and background simulation (with and without $Z \rightarrow \tau\tau \rightarrow ll$ events), in the 500 $\mu\text{m}$ –10 cm region. The ratios of the actual yield to the estimated yield and their statistical uncertainties are given. The A, B, C, and D regions are defined as follows: A is 20–30 $\mu\text{m}$ in prompt lepton $ d_0 $ and 20–100 $\mu\text{m}$ in displaced lepton $ d_0 $ , B is 20–30 $\mu\text{m}$ in prompt lepton $ d_0 $ and 500 $\mu\text{m}$ –10 cm in displaced lepton $ d_0 $ , C is 30–100 $\mu\text{m}$ in prompt lepton $ d_0 $ and 20–100 $\mu\text{m}$ in displaced lepton $ d_0 $ , and D (the test region) is 30–100 $\mu\text{m}$ in prompt lepton $ d_0 $ and 500 $\mu\text{m}$ –10 cm in displaced lepton $ d_0 $ . . . . .	88
3.12 The correction factors and the uncorrected and corrected background estimates in SR I. The correction factor uncertainties include both the uncertainty in the average and the additional uncertainty obtained from varying the fit extrapolation point. The total uncertainty (statistical plus systematic) is given for the corrected background estimates.	93
3.13 The systematic uncertainty and the background estimates in SRs II, III, and IV. The total uncertainty (statistical plus systematic) is given for each estimate. . . . .	94
3.14 Closure test results in background simulation in the SRs, with the correction applied. The estimated number of events, the actual number of events, and their total uncertainties (statistical plus systematic) are given. In cases where the actual number of events is zero, the uncertainty is given by the product of the average background simulation event weight and the upper bound of the 68% Poisson interval given by a single observation of zero events. . . . .	95

3.15 Some properties of the seven events found in data with the material interactions selection inverted. . . . .	96
3.16 Background estimates in data while applying the 2018 $\mu\mu$ preselection and the additional requirement of at least one medium $b$ -tagged jet. The estimates with at least one $b$ jet are about an order of magnitude below the nominal prediction. . . . .	98
3.17 A closure test of the ABCD method in 2018 QCD simulation in the $\mu\mu$ channel with the muon isolation criterion inverted. The estimates from the ABCD method, the actual yields in simulation, and the ratios of the actual to the estimated yields are shown. . . . .	99
3.18 Systematic uncertainties in the signal efficiency for all three years and the three channels. The mean is provided in cases where the uncertainty varies by signal sample. Uncertainties in the same row are treated as correlated among the years of data taking, except for the displaced tracking and muon pixel hit efficiencies, where the 2016 uncertainty is treated as uncorrelated with the 2017 and 2018 uncertainties.	103
3.19 The number of estimated background and observed events in each channel and SR. For each estimate, the total uncertainty is given. The $p_T$ boundaries that separate the low- and high- $p_T$ bins of SR I are listed in Table 3.9. . . . .	108
3.20 The pre- and post-fit predictions for each signal region bin. . . . .	117
C.1 Cosmic ray muon arrival time requirements used when measuring displaced tracking efficiency in data and simulation. . . . .	132
C.2 Mean measured efficiency to reconstruct both lepton tracks in simulated $t\bar{t} \rightarrow l\bar{b} l\bar{b}$ events in data and simulation and the resulting systematic uncertainty. The top squark mass and proper decay length are assumed to be 1800 GeV and 100 cm. . . . .	137

## List of Figures

Figure	Page
1.1 The SM particle content. . . . .	3
1.2 Summary of Standard Model production cross section measurements from the CMS experiment [1]. . . . .	8
1.3 The Higgs boson mass corrected by a fermion loop (left) and a fermion mass corrected by photon loop (right). . . . .	10
1.4 Corrections to the Higgs boson mass from the top quark (left) and top squark (right) cancel in exact SUSY. The top quark and top squark contributions are enhanced by the large coupling between the large Higgs-top quark coupling. . . . .	11
1.5 Mass limits at 95 % CL for a simplified model of gluino pair production with gluino decays to pairs of top quarks and the LSP (left) and top squark pair production with squark decays to a top quark and the LSP (right) from several CMS analyses [2]. . . . .	12
1.6 Masses and proper decay lengths of many Standard Model particles. Particles with proper decay lengths above approximately $10^{-4}$ m will be noticeably long-lived in collider detectors such as CMS. . . . .	13
1.7 Long-lived decays of the neutron (left) and muon (right). . . . .	14
1.8 Pair-produced top squarks that each decay to a bottom quark and a lepton through an R-parity-violating $LQD$ vertex. . . . .	17
2.1 Layout of the LHC experiments [3]. . . . .	19

2.2	A diagram of the CERN accelerator complex. The analysis presented in Chapter 3 utilizes protons accelerated by LINAC 2, BOOSTER (also known as PSB), PS, SPS, and finally the LHC before their ultimate collision inside CMS [4]. . . . .	20
2.3	The peak instantaneous (top) and integrated (bottom) luminosity delivered by the LHC during proton operation between 2011 and 2018 [5]. . . . .	22
2.4	Diagram of an LHC dipole magnet in cross-section [6]. . . . .	23
2.5	The CMS detector [7]. . . . .	26
2.6	The stored-energy-over-mass ratio, E/M, for several detector magnets (left), and a cross-sectional view of the four-layer winding of reinforced conductor in the CMS superconducting solenoid (right) [8]. . . . .	28
2.7	Measured single hit efficiency per layer as a function of the instantaneous luminosity (left) and inelastic collisions per bunch crossing (right) in data taken with the original CMS pixel detector in 2016 [9]. . . . .	30
2.8	Comparison of the original and Phase-1 CMS pixel detector layouts in $y$ - $z$ plane [10]. . . . .	31
2.9	Layout of the CMS silicon tracker. TIB, TOB, TID, and TEC refer to subdetectors of the strip detector while PIXEL refers to the original pixel detector. The Phase-1 pixel detector is contained within the same volume [8]. . . . .	32
2.10	The observed local p-value for the five decay modes and the overall combination as a function of the SM Higgs boson mass showing the importance of the ECAL mass resolution in the discovery of the Higgs boson by the CMS experiment. The dashed line shows the expected local p-values for a SM Higgs boson with a mass $m_H$ [11]. . . . .	33
2.11	Layout of the hadron calorimeter barrel (HB), outer (HO), endcap (HE), and forward (HF) subdetectors [8]. . . . .	35
2.12	Muon momentum resolution as a function of momentum when using the CMS muon system, the CMS inner tracker, and the combination of the two subdetectors in two different $\eta$ ranges [12]. . . . .	37

2.13 Sketch of a CMS muon system drift cell showing drift lines and isochrones. The plates at the top and bottom of the cell are at ground potential while the voltages applied to the electrodes are +3600 V for wires, +1800 V for strips, and -1200 V for cathodes [8]. . . . .	37
2.14 A sketch of a transverse slice of the CMS detector showing representative particle interactions used to identify and reconstruct particles with the CMS Particle Flow algorithm [13]. . . . .	42
3.1 Illustration of several possible experimental signatures of long-lived particles [14]. . . . .	45
3.2 Illustration of the displaced leptons signature showing the definition of $d_0$ in a transverse view of the CMS interaction point. $X$ denotes a new long-lived particle, $\ell$ denotes an electron or muon, and $Y$ denotes any other decay products of the new long-lived particle. When interpreting the results of the Displaced Leptons analysis with the Displaced SUSY model, $X$ refers to a top squark and $Y$ refers to a b or d quark. . . . .	47
3.3 Distribution of data (colors) and simulated Displaced SUSY events (black boxes) in the plane defined by electron $ d_0 $ and muon $ d_0 $ . The size of the black boxes are proportional to the bin content, and the bins along the x and y axes include underflow. All events are required to pass the $e\mu$ preselection defined in Section 3.3. . . . .	50
3.4 The muon isolation pileup correction term, for the standard muon isolation and the modified muon isolation in simulated $t\bar{t}$ events that pass the $e\mu$ preselection in 2018 conditions. The plot on the left is for muon $ d_0  < 100 \mu\text{m}$ , and the plot on the right is for muon $500 <  d_0  < 1000 \mu\text{m}$ . . . . .	63
3.5 The electron $ d_0 $ versus the muon $ d_0 $ , for $t\bar{t}$ simulated events that pass the $e\mu$ preselection and where at least one lepton comes from a heavy-flavor meson. The plot on the left uses the standard isolation, and the plot on the right uses the modified isolation. . . . .	64
3.6 The muon custom isolation distribution for simulated $t\bar{t}$ background and $\tilde{t}\tilde{t} \rightarrow \bar{l}b l\bar{b}$ signal events in 2018 conditions. . . . .	64

3.7	The electron $\eta - \phi$ distribution in a prompt-muon, displaced-electron control region in 2017 (left) and 2018 (right) data before vetoing the regions affected by pixel power-supply issues. . . . .	65
3.8	The electron (left) and muon (right) $ d_0 $ distributions for 2018 simulation events that pass the $e\mu$ preselection criteria. The upper two plots show $\tilde{t}\bar{t} \rightarrow l\bar{l}l\bar{l}$ simulation for a single $\tilde{t}$ mass and four different proper decay lengths; each histogram is normalized to unity. The lower two plots show the background simulation normalized to the integrated luminosity. In all of the histograms, the last bin includes the overflow. All of the corrections from Section 3.4 are applied. . . . .	67
3.9	The cumulative number of events that pass each criterion in the $e\mu$ (upper), $ee$ (middle), and $\mu\mu$ (lower) preselection, using 2018 signal simulation. Several $\tilde{t}$ proper decay lengths are shown. The jet criteria do not exclude any events and are simply an artifact of the analysis framework. . . . .	68
3.10	The electron (top) and muon (bottom) $p_T$ (left), $\eta$ (center), and $ d_0 $ (right) distributions in the $e\mu$ prompt control region for 2016 data and MC simulation. The rightmost bin in each plot contains the overflow entries. . . . .	70
3.11	The electron $p_T$ (left), $\eta$ (center), and $ d_0 $ (right) distributions in the $ee$ prompt control region for 2016 data and MC simulation. The rightmost bin in each plot contains the overflow entries. . . . .	70
3.12	The muon $p_T$ (left), $\eta$ (center), and $ d_0 $ (right) distributions in the $\mu\mu$ prompt control region for 2016 data and MC simulation. The rightmost bin in each plot contains the overflow entries. . . . .	71
3.13	The uncorrected lepton $ d_0 $ distributions in the $e\mu$ prompt control region, for electrons (left) and muons (right), for 2017 data and simulation (upper), and 2018 data and simulation (lower). The rightmost bin in each plot contains the overflow entries. . . . .	74
3.14	The average lepton $ d_0 $ as a function of $\phi$ in the $e\mu$ prompt control region, for electrons (left) and muons (right), for 2017 data and simulation. . . . .	76

3.15 The lepton $d_0$ distributions with Gaussian fits in the 2017 $e\mu$ prompt control region for (working from left to right) electrons in data, electrons in background simulation, muons in data, and muons in background simulation. . . . .	76
3.16 The lepton $d_0$ distributions with Gaussian fits in the 2018 $e\mu$ prompt control region for (working from left to right) electrons in data, electrons in background simulation, muons in data, and muons in background simulation. . . . .	76
3.17 The corrected lepton $ d_0 $ distributions in the $e\mu$ prompt control region, for electrons (left) and muons (right), for 2017 data and simulation (upper), and 2018 data and simulation (lower). The rightmost bin in each plot contains the overflow entries. . . . .	77
3.18 The fraction of electrons (left) and muons (right) from different parents as a function of lepton $ d_0 $ , for simulated $t\bar{t}$ events that pass the 2018 $e\mu$ channel preselection. In $t\bar{t}$ events, the vast majority of leptons whose parent is a W boson are produced in a prompt decay. . . . .	81
3.19 The fraction of muons from different parents as a function of muon $ d_0 $ , for simulated DY events that pass the 2018 $\mu\mu$ channel preselection and the additional constraint that the leading and subleading muon both come from the same type of parent particle. . . . .	82
3.20 A diagram of the ABCD method overlaid on simulated background events passing the 2018 $e\mu$ preselection. A, B, and C are control regions, and D corresponds to the inclusive SR, which includes SRs I, II, III, and IV. Underflow events are included in the bins along the left and bottom edges. When performing the background estimate, regions B and C are further subdivided to coincide with the SR for which the estimate is being performed. . . . .	83
3.21 Background estimation closure tests in data, in 100–500 $\mu\text{m}$ subregions of regions B (left) and C (right) in the $e\mu$ channel. Each plot shows the ratio of the actual to the estimated number of events as a function of the prompt lepton $ d_0 $ in 2016 (top) and 2017–18 (bottom). A linear fit is shown in black along with the 68 % and 95 % confidence intervals of the extrapolated fit value. . . . .	90

3.22 Background estimation closure tests in data, in 100–500 $\mu\text{m}$ subregions of regions B (left) and C (right) in the $ee$ channel. Each plot shows the ratio of the actual to the estimated number of events as a function of the prompt lepton $ d_0 $ in 2016 (top) and 2017–18 (bottom). A linear fit is shown in black along with the 68 % and 95 % confidence intervals of the extrapolated fit value. . . . .	91
3.23 Background estimation closure tests in data, in 100–500 $\mu\text{m}$ subregions of regions B (left) and C (right) in the $\mu\mu$ channel. Each plot shows the ratio of the actual to the estimated number of events as a function of the prompt lepton $ d_0 $ in 2016 (top) and 2017–18 (bottom). A linear fit is shown in black along with the 68 % and 95 % confidence intervals of the extrapolated fit value. . . . .	92
3.24 The dimuon invariant mass distribution in the $\mu\mu$ channel with the muon isolation criterion inverted, for 2018 data and QCD multijet simulation. . . . .	99
3.25 The dimuon invariant mass distribution in 2018 data in the $\mu\mu$ channel, in the prompt control region (black), SR I (blue), SR IV (red), with the muon isolation and di-muon $\Delta R$ criteria inverted. The equivalent distribution from the prompt control region is also shown in green. . . . .	100
3.26 The pixel hit efficiency as a function of muon $ d_0 $ , for cosmic simulation and NoBPTX data in 2016 (left), 2017 (middle), and 2018 (right) conditions. . . . .	106
3.27 The number of estimated background and observed events in each channel and SR, with a representative signal overlaid, for 2016 (top) and 2017–2018 (bottom). For each background estimate and signal yield, the total uncertainty is given. . . . .	109
3.28 The number of estimated background and observed events in each channel and SR, with a representative signal overlaid, for 2016–2018. For each background estimate and signal yield, the total uncertainty is given. . . . .	110
3.29 Two-dimensional distributions of $ d_0^a $ and $ d_0^b $ , for the events in data that pass the $e\mu$ (left), $ee$ (middle), and $\mu\mu$ (right) preselection. The bins along the x and y axes contain underflow. The inclusive signal region covers the region between 100 $\mu\text{m}$ and 10 cm in each $ d_0 $ variable shown. . . . .	110

3.30 Two-dimensional distributions of $ d_0^a $ and $ d_0^b $ , for data events in the inclusive SR in the $e\mu$ (left), $ee$ (middle), and $\mu\mu$ (right) channels. . . . .	111
3.31 Muon $\phi$ and di-muon invariant mass distributions for data and composite background simulation in the $\mu\mu$ channel in the inclusive SR. The background simulation is normalized to the ABCD method background prediction. . . . .	112
3.32 The 95% CL upper limits on the long-lived particle mass ( $m_{\tilde{t}}$ ) as a function of its lifetime ( $c\tau$ ), for the $e\mu$ , $ee$ , and $\mu\mu$ channels. The $\tilde{t}\bar{t} \rightarrow \bar{l}b\bar{l}b$ (top) and $\tilde{t}\bar{t} \rightarrow \bar{l}d\bar{l}d$ (bottom) processes are shown. . . . .	114
3.33 The 95% CL upper limits on the long-lived particle mass ( $m_{\tilde{t}}$ ) as a function of its lifetime ( $c\tau$ ). The colors indicate the observed 95% CL upper limit on the cross section. The $\tilde{t}\bar{t} \rightarrow \bar{l}b\bar{l}b$ (left) and $\tilde{t}\bar{t} \rightarrow \bar{l}d\bar{l}d$ (right) processes are shown. . . . .	115
3.34 The distribution of pulls for each signal region bin, where pulls are calculated as the difference between the post-fit background yield and the pre-fit background yield divided by the pre-fit background uncertainty (left). The distribution of pulls for each background nuisance parameter, where pulls are calculated as the difference between the post-fit value and the pre-fit value divided by the pre-fit uncertainty (right). . . . .	118
3.35 The observed asymptotic significances for the $\tilde{t}\bar{t} \rightarrow \bar{l}b\bar{l}b$ process as a function of $\tilde{t}$ mass and lifetime using the combined results. . . . .	119
3.36 The observed asymptotic significances for the $\tilde{t}\bar{t} \rightarrow \bar{l}b\bar{l}b$ process as a function of $\tilde{t}$ mass and lifetime in the $ee$ (left), $e\mu$ (center), $\mu\mu$ channels (right). . . . .	119

A.1 Transverse decay length distribution of reconstructed $K_S^0 \rightarrow \pi^+\pi^-$ candidates for various runs in 2016 (top left), 2017 (top right) and 2018 (bottom). The peak instantaneous luminosity of each run is indicated in the legend, and each distribution is normalized to the integrated luminosity of the run. In the 2016 plot, runs taken before (after) the APV25 saturation effect was mitigated are shown by solid (dashed) lines. In the 2017 plot, the run with lowest (highest) instantaneous luminosity examined in each data taking era is plotted with a dashed (solid) line. Towards the end of 2017 (orange and black lines) the LHC ran with approximately 20% fewer proton bunches, meaning that the instantaneous luminosity per bunch crossing was higher than one might naively expect from the instantaneous luminosities shown in the legend.	126
B.1 The standard deviation of the leading muon $d_0$ as a function of the leading muon $\eta$ for simulated background events (left). To ensure that the variation in width is purely due to $d_0$ resolution effects, we use a sample of simulated Drell-Yan events from which the $Z \rightarrow \tau\tau \rightarrow ll$ events have been removed. Muon $\eta$ distribution for simulated $\tilde{t}\tilde{t} \rightarrow \bar{l}b\bar{l}\bar{b}$ events (right). The $\mu\mu$ preselection with a loosened $ \eta $ requirement is applied in both plots. . . . .	128
B.2 Electron $\eta$ distribution for simulated background events in which the electron parent particles are required to be SM mesons (left). Electron $\eta$ distribution for simulated $\tilde{t}\tilde{t} \rightarrow \bar{l}b\bar{l}\bar{b}$ events (right). The $e\mu$ preselection with a loosened $\eta$ requirement is applied in both plots. .	128
C.1 Distribution of the arrival time of cosmic rays at their point of closest approach to the beamline as measured by the muon system in 2016 (top left), 2017 (top right), and 2018 (bottom) in data and simulation. Only cosmic ray muons with $ d_0  < 8$ cm and $ z_0  < 20$ cm are considered.	133
C.2 Measured downward tracking efficiency versus cosmic ray muon arrival time in 2016 (top left), 2017 (top right), and 2018 (bottom) in data and simulation. Only cosmic ray muons with $ d_0  < 8$ cm and $ z_0  < 20$ cm are considered. . . . .	134

C.3 Measured downward tracking efficiency in 2016 (top), 2017 (middle), and 2018 (bottom) versus transverse impact parameter (left) and lon- gitudinal impact parameter (right) in data and simulation. The longi- tudinal (transverse) impact parameter is constrained to less than 20 cm (1.2 cm) when plotting against the transverse (longitudinal) impact pa- rameter. . . . .	136
--	-----

## Chapter 1: Introduction

2 Particle physics seeks to understand the fundamental constituents of nature and  
3 their interactions. At the present moment, the Standard Model of particle physics  
4 (along with the general theory of relativity) represents the most complete understand-  
5 ing humanity has yet achieved. At the same time, the Standard Model cannot explain  
6 gravity or several observed but not yet understood aspects of nature and therefore  
7 must give way to a more complete theory at a higher energy scale. One approach  
8 to understanding what might be hiding beneath the Standard Model is to use high-  
9 energy particle collisions to probe nature at ever smaller length scales. This thesis  
10 presents a search for beyond the Standard Model physics in 13 TeV proton-proton col-  
11 lision data collected by the Compact Muon Solenoid experiment at the Large Hadron  
12 Collider, which is the highest-energy particle collider ever constructed.

13 The search presented in this thesis targets new long-lived particles that produce  
14 displaced leptons, a unique signature that could evade many existing searches for new  
15 physics. In this chapter, I present theoretical context in the form of a brief overview  
16 of the Standard Model and targeted discussion of beyond the Standard Model physics  
17 and long-lived particles. I then present the experimental context with an overview of  
18 the Large Hadron Collider and the Compact Muon Solenoid detector in Chapter 2,  
19 present the search itself in Chapter 3, and conclude in Chapter 4.

<sup>20</sup> **1.1 The Standard Model**

<sup>21</sup> The Standard Model of particle physics (SM) describes all known particles and  
<sup>22</sup> their non-gravitational interactions. Developed and experimentally verified over the  
<sup>23</sup> past six decades, the SM posits the existence of twelve spin- $\frac{1}{2}$  particles, the fermions,  
<sup>24</sup> that make up all observed matter; twelve spin-1 particles, the gauge bosons, that  
<sup>25</sup> communicate the electromagnetic, weak, and strong forces; and one fundamental  
<sup>26</sup> scalar, the Higgs boson, which breaks electroweak symmetry, giving mass to the  
<sup>27</sup> gauge bosons and fermions.

<sup>28</sup> The fermions and gauge bosons can be classified according to the forces with which  
<sup>29</sup> they interact. The fermions are divided into six quarks, which carry color and interact  
<sup>30</sup> via the strong force, and six leptons, which do not. Furthermore, all six quarks  
<sup>31</sup> and three of the leptons carry electric charge and interact electromagnetically. The  
<sup>32</sup> charged leptons include the electron, muon, and tau, and the neutral leptons are called  
<sup>33</sup> neutrinos. All fermions interact via the weak force. The gauge bosons include the  
<sup>34</sup> photon, which communicates the electromagnetic force; the  $W^+$ ,  $W^-$ , and  $Z^0$  bosons,  
<sup>35</sup> which communicate the weak force; and eight gluons that communicate the strong  
<sup>36</sup> force. Of these, only the  $W^+$  and  $W^-$  are electrically charged and only the gluons  
<sup>37</sup> carry color charge. Finally, the fermions are grouped into three generations, each  
<sup>38</sup> with two quarks, one charged leptons, and one neutral lepton. Figure 1.1 diagrams  
<sup>39</sup> the grouping of the SM particles and lists some of their properties.

<sup>40</sup> In the SM, the interactions between particles are governed by two theories: quan-  
<sup>41</sup> tum chromodynamics, which describes the strong force, and the electroweak theory,  
<sup>42</sup> which describes the electromagnetic and weak forces. The following sections provide  
<sup>43</sup> a brief overview of these theories.

# Standard Model of Elementary Particles

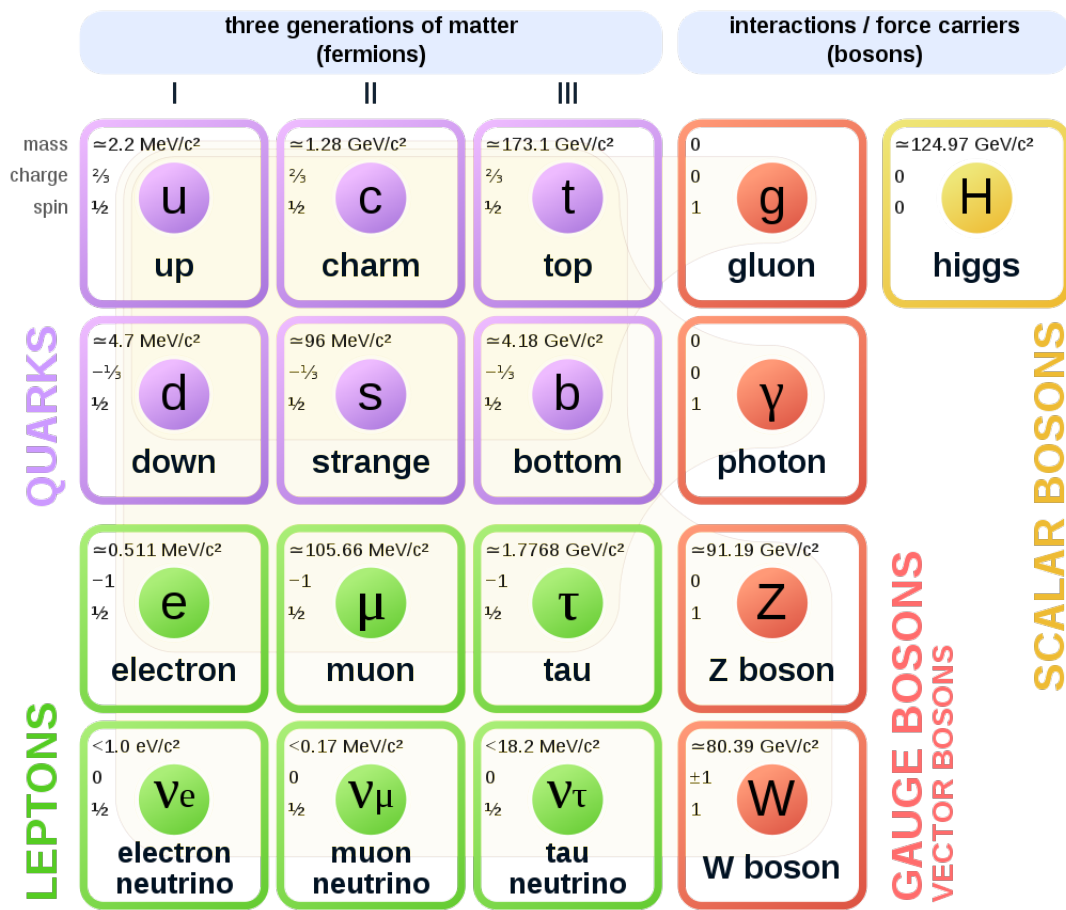


Figure 1.1: The SM particle content.

<sup>44</sup> **1.1.1 Quantum chromodynamics**

<sup>45</sup> Quantum chromodynamics (QCD) describes the strong interactions between  
<sup>46</sup> quarks and gluons and is based on the  $SU(3)_c$  symmetry group, where the subscript c  
<sup>47</sup> refers to color charge. In QCD, all quarks and gluons carry color charge, which allows  
<sup>48</sup> interactions between two quarks of the same generation and a gluon, three gluons, or  
<sup>49</sup> four gluons. QCD is responsible for the formation of all hadrons (such as protons and  
<sup>50</sup> neutrons), and leads to two unique phenomena: confinement and asymptotic freedom  
<sup>51</sup> [15, 16].

<sup>52</sup> Confinement refers to the experimental fact that an isolated particle with color  
<sup>53</sup> charge has never been directly observed. Composite particles composed of quarks  
<sup>54</sup> and gluons are always neutral under color, and attempts to separate the constituent  
<sup>55</sup> particles will only produce new hadrons. This phenomenon is the result of the unique  
<sup>56</sup> running of the strong coupling constant, which increases with decreasing energy (and  
<sup>57</sup> therefore increasing distance).

<sup>58</sup> Asymptotic freedom is the other side of the coin: if the strong coupling constant  
<sup>59</sup> decreases as the interaction energy increases, then the strong interaction becomes  
<sup>60</sup> more and more feeble at high energies. In high energy interactions (such as those  
<sup>61</sup> at the Large Hadron Collider), the strong coupling constant is in fact small enough  
<sup>62</sup> to render the quarks nearly free. In this regime, perturbative calculations become  
<sup>63</sup> possible.

<sup>64</sup> **1.1.2 The electroweak theory**

<sup>65</sup> The electroweak theory unifies the electromagnetic and weak interactions and is  
<sup>66</sup> based on the  $SU(2)_L \otimes U(1)_Y$  symmetry group. It posits two new charges: weak

67 isospin, which has three components  $T_{1,2,3}$ , and hypercharge,  $Y$ .  $T_3$  is  $\pm\frac{1}{2}$  for all left-  
 68 handed fermions and 0 otherwise, while  $Y$  varies according to  $Q = T_3 + \frac{1}{2}Y$ , where  $Q$   
 69 is the familiar electric charge. Each generation of left-handed quarks or leptons forms  
 70 an  $SU(2)$  doublet. The first generation doublets, for example, are:

$$\begin{pmatrix} \nu_e \\ e^- \end{pmatrix}_L, \begin{pmatrix} u \\ d \end{pmatrix}_L \quad (1.1)$$

71 where, as in  $SU(2)_L$ , the L denotes left-handed chiral states. The three generators  
 72 of  $SU(2)_L$  result in three massless spin-1 bosons:  $W^1$ ,  $W^2$ , and  $W^3$ , while  $U(1)_Y$   
 73 gives rise to one massless spin-1 boson,  $B^0$ . After electroweak symmetry is broken  
 74 by the mechanism explained in the following subsection, the physical  $W^\pm$  bosons are  
 75 identified as superpositions of  $W^1$  and  $W^2$  while the  $Z$  boson and the photon are  
 76 identified as superpositions of  $W^3$  and  $B^0$  [17].

77 Terms in the electroweak Lagrangian involve either two left-handed fermions and a  
 78  $W^\pm$  or  $Z$  boson, two electrically charged particles and a photon, or charge-conserving  
 79 combinations of  $W^\pm$ s,  $Z$ s, and photons that include three or four particles. Con-  
 80 spicuously missing, however, are mass terms for the electroweak gauge bosons or  
 81 fermions.

### 82 **1.1.3 The Higgs mechanism**

83 As shown in Fig. 1.1, the fermions and  $W^\pm$  and  $Z$  bosons all have nonzero mass.  
 84 Accounting for this fact within the context of the electroweak theory is difficult be-  
 85 cause explicit mass terms violate the gauge and chiral symmetry of  $SU(2)_L \otimes U(1)_Y$ .  
 86 For example, a term such as

$$\frac{1}{2}m_A^2 A^\mu A_\mu, \quad (1.2)$$

<sup>87</sup> which assigns mass  $m_A$  to gauge boson  $A$ , becomes

$$\frac{1}{2}m^2(A^\mu - \partial^\mu\alpha)(A_\mu - \partial_\mu\alpha) \neq \frac{1}{2}m^2A^\mu A_\mu \quad (1.3)$$

<sup>88</sup> under a  $U(1)$  gauge transformation, and a term such as

$$m_f\bar{f}f = m_f(\bar{f}_R f_L + \bar{f}_L f_R), \quad (1.4)$$

<sup>89</sup> which assigns mass  $m_f$  to fermion  $f$ , breaks chiral symmetry by coupling the right-  
<sup>90</sup> and left-handed components of the fermion.

<sup>91</sup> If the gauge and chiral symmetries of  $SU(3)_c \otimes SU(2)_L \otimes U(1)_Y$  truly are sym-  
<sup>92</sup> metries of nature and the fermions and  $W^\pm$  and  $Z$  bosons truly have nonzero mass,  
<sup>93</sup> then another mechanism must be at work. Spontaneous symmetry breaking, which  
<sup>94</sup> occurs when the vacuum state does not exhibit all of the symmetries of the underlying  
<sup>95</sup> theory. In such a situation, each spontaneously broken continuous symmetry gives  
<sup>96</sup> rise to a massless scalar particle [18]. In the case of spontaneously broken continuous  
<sup>97</sup> *gauge* symmetries, however, there exists a mechanism by which the massless bosons  
<sup>98</sup> are removed and some of the gauge bosons associated with the generators of the sym-  
<sup>99</sup> metries acquire mass [19, 20, 21]. In the SM, this mechanism, known as the Higgs  
<sup>100</sup> mechanism, breaks electroweak symmetry, gives mass to the fermions and  $W^\pm$  and  $Z$   
<sup>101</sup> bosons, and results in one massive scalar particle, the Higgs boson.

<sup>102</sup> The Higgs mechanism adds the scalar doublet

$$\Phi = \begin{pmatrix} \phi^+ \\ \phi^0 \end{pmatrix}, \quad (1.5)$$

<sup>103</sup> whose potential is given by

$$V(\Phi^\dagger\Phi) = \mu^2\Phi^\dagger\Phi + \lambda(\Phi^\dagger\Phi)^2, \quad (1.6)$$

104 to the SM. If  $\mu^2 < 0$  and  $\lambda > 0$ , then  $\Phi^\dagger \Phi = -\frac{\mu^2}{2\lambda}$  defines a circle of minima in the  $\phi^+ -$   
105  $\phi^0$  plane. Even though the potential remains invariant under  $SU(2)_L \otimes U(1)_Y$ , nature  
106 must spontaneously choose a vacuum state somewhere along this circle. Because  
107 the vacuum state does not respect  $SU(2)_L \otimes U(1)_Y$ , the symmetry is said to be  
108 spontaneously broken.

109 This procedure has three significant consequences. First, three of the four degrees  
110 of freedom originally associated with  $\Phi$  are now associated with the longitudinal  
111 components of the  $W^\pm$  and  $Z$  bosons, which causes them to acquire mass while the  
112 photon remains massless. Second,  $\Phi$ 's remaining degree of freedom adds a single  
113 massive scalar, the Higgs boson, to the theory. Third, the interaction between the  
114 fermions and the nonzero vacuum state of the scalar field produces fermion mass  
115 terms that obey chiral symmetry.

#### 116 1.1.4 Current status

117 The SM is remarkably successful. It describes all known particles and their non-  
118 gravitational interactions, and it has passed countless experimental tests over the last  
119 several decades. Figure 1.2 gives an idea of the scale of this success by comparing  
120 theoretical predictions of SM production cross sections with measurements performed  
121 by the CMS experiment: theory and experiment agree across 41 different SM processes  
122 at 7, 8, and 13 TeV. In 2012, the CMS and ATLAS experiments independently  
123 discovered an approximately 125 GeV scalar particle with properties consistent with  
124 the SM Higgs boson [11, 22]. Further measurements in 7, 8, and 13 TeV proton-proton  
125 collisions at the Large Hadron Collider continue to agree with SM predictions of the  
126 Higgs boson properties [23, 24]. We finally have meaningful evidence as to the origin

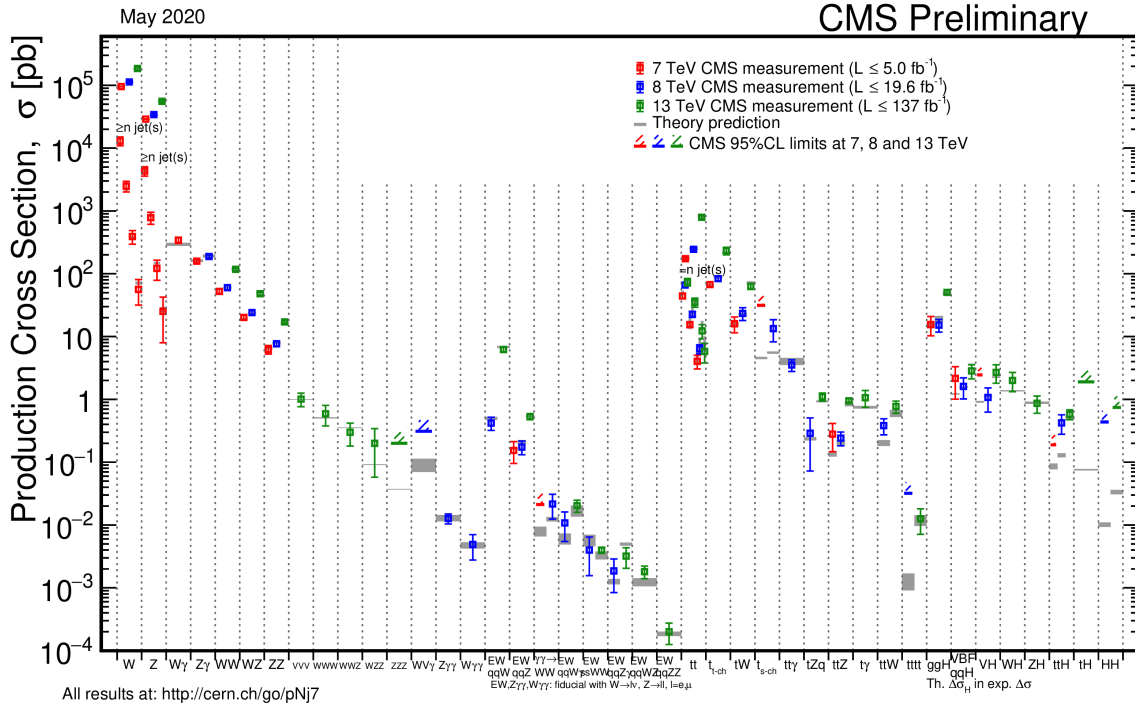


Figure 1.2: Summary of Standard Model production cross section measurements from the CMS experiment [1].

<sup>127</sup> of electroweak symmetry breaking, and all current evidence indicates that the SM  
<sup>128</sup> Higgs mechanism is indeed responsible.

Despite this remarkable success, the SM is not without problems. For one, it cannot be the whole story: it says nothing on the subjects of gravity, dark matter, or dark energy, which implies that it only describes about 5% of the energy content of the universe [25] and that a more complete theory must take over at or below the energy scale where gravity becomes important ( $M_P \approx 10^{19}$  GeV) [26]. Furthermore, many aspects of the SM seem arbitrary and unmotivated. It offers no explanation, for example, for why three generations of fermions are necessary or why its many parameters take the values they do. It could be that these unmotivated values are

137 simply experimental facts of nature without explanation, but the history of science  
138 implies that a deeper understanding is likely hiding beneath the surface. Finally, the  
139 observed value of the Higgs boson mass is not only unexplained, it is unnatural. This  
140 final issue, which is explained in the following paragraphs, is a powerful motivation  
141 to search for new physics at currently accessible energy scales.

142 **Naturalness**

143 The naturalness criterion states that an effective theory such as the SM must  
144 not be overly sensitive to the details of the underlying higher energy theory. Put  
145 another way, it requires that any dimensionless parameter much smaller than one  
146 must be protected by a custodial symmetry [27]. Such a criterion may or may not be  
147 respected by nature, but history and simple probability are on its side.

148 The dimensionless parameter in question is the mass of the Higgs boson, which is  
149 quadratically sensitive to  $\Lambda$ , the energy scale at which a new theory takes over. All SM  
150 parameters are affected by interactions with virtual particles through loop diagrams  
151 such as those shown in Fig. 1.3, but the Higgs boson mass is particularly sensitive.  
152 As a fundamental scalar, the Higgs boson lacks the chiral and gauge symmetries  
153 enjoyed by the fermions and gauge bosons. These symmetries, known as custodial  
154 symmetries, protect the fermion and gauge boson masses by guaranteeing that all  
155 corrections are proportional to the bare masses themselves. If the SM is indeed valid  
156 up to  $M_P$ , then the bare mass of the Higgs boson must be coincidentally equal and  
157 opposite to the sum of the terms that correct it to approximately one part in  $10^{32}$   
158 [26]. Such miraculous fine tuning is technically possible, but it could also be strong  
159 evidence that a deeper physical mechanism is at work.

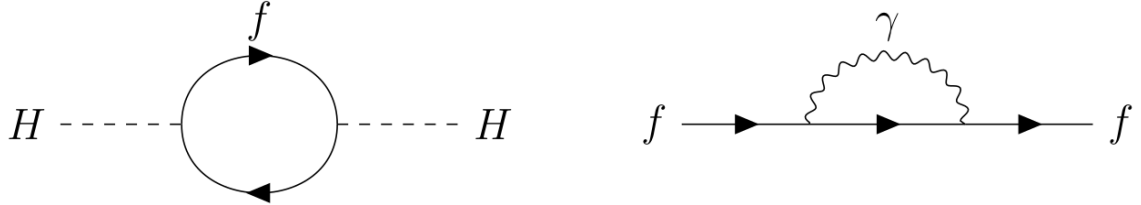


Figure 1.3: The Higgs boson mass corrected by a fermion loop (left) and a fermion mass corrected by photon loop (right).

## 160 1.2 Beyond the Standard Model

161 Many beyond the SM (BSM) theories have been proposed to address the issues  
162 discussed in Section 1.1.4. Theories such as large extra dimensions address the unnat-  
163 ural Higgs boson mass by allowing gravity to spread across more than three spatial  
164 dimensions, which lowers  $M_P$  and therefore the size of the Higgs boson mass correc-  
165 tions [28]. Other theories posit new symmetries that protect the Higgs boson mass  
166 from large corrections. The following section explains supersymmetry, which protects  
167 the Higgs boson mass with a new symmetry between bosons and fermions.

### 168 1.2.1 Supersymmetry

169 Supersymmetry (SUSY) introduces a new symmetry in which every SM particle  
170 fits into a larger multiplet with an inherent symmetry between bosons and fermions.  
171 In its simplest form, SUSY predicts one new boson for every SM fermion, one new  
172 fermion for every SM boson, and one new Higgs doublet. The increase in particle  
173 multiplicity necessitates a new naming convention: the spin-0 superpartners of the SM  
174 fermions are called sfermions (e.g. sleptons or squarks) while the spin- $\frac{1}{2}$  superpartners

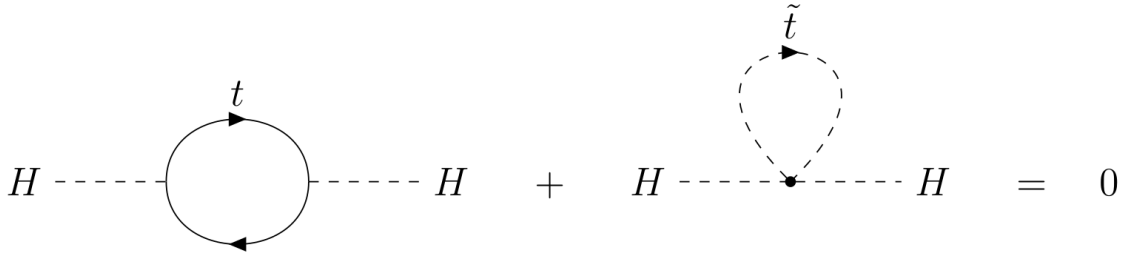


Figure 1.4: Corrections to the Higgs boson mass from the top quark (left) and top squark (right) cancel in exact SUSY. The top quark and top squark contributions are enhanced by the large coupling between the large Higgs-top quark coupling.

175 to the SM bosons add "ino" to the end of their SM counterpart (e.g. Higgsino or  
176 wino).

177 When calculating contributions to the Higgs boson mass from loop diagrams, one  
178 finds that fermion loops differ in sign from boson loops, which means that in SUSY  
179 every bosonic correction to the Higgs boson mass is cancelled by a fermionic correction  
180 and vice versa. If SUSY were an exact symmetry of nature, the cancellation would  
181 be perfect, and the observed Higgs boson mass would match the bare Higgs boson  
182 mass exactly [29]. Figure 1.4 shows a sample leading-order cancellation.

183 Exact SUSY also requires that SUSY particles have the same mass as their SM  
184 counterparts, so the uniformly null results in collider searches imply that if SUSY  
185 exists, it must be a broken symmetry. In broken SUSY, the diagrams in Fig. 1.4 no  
186 longer exactly cancel. Instead, the resulting correction is proportional to the mass of  
187 the top squark [30], which means that broken SUSY can still resolve the naturalness  
188 problem if the masses of the SUSY particles that correct the Higgs boson mass are  
189 themselves approximately at the weak scale (say  $\mathcal{O}(250 \text{ GeV})$ ). Many natural SUSY  
190 scenarios are therefore excluded as collider experiments set increasingly large lower

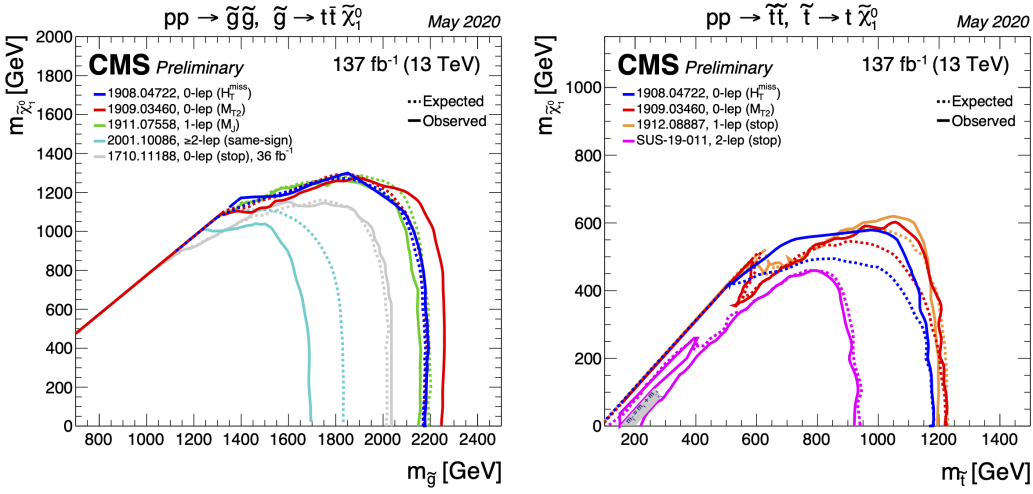


Figure 1.5: Mass limits at 95 % CL for a simplified model of gluino pair production with gluino decays to pairs of top quarks and the LSP (left) and top squark pair production with squark decays to a top quark and the LSP (right) from several CMS analyses [2].

<sup>191</sup> bounds on SUSY particle masses. Figure 1.5, for example, shows that the exclusion  
<sup>192</sup> bounds on top squark and gluino masses extend above 1 TeV in several recent CMS  
<sup>193</sup> analyses.

<sup>194</sup> As the available natural SUSY parameter space is further constricted, it is im-  
<sup>195</sup> portant to investigate signatures of new physics that conventional analyses may be  
<sup>196</sup> missing. One possibility, new long-lived particles, is presented in the following section.

### <sup>197</sup> 1.2.2 Long-lived particles

<sup>198</sup> In the context of collider physics, long-lived particles (LLPs) are particles whose  
<sup>199</sup> lifetimes are such that they decay a measurable distance from the collision point. This  
<sup>200</sup> category includes everything from particles that decay less than 1 mm away from the

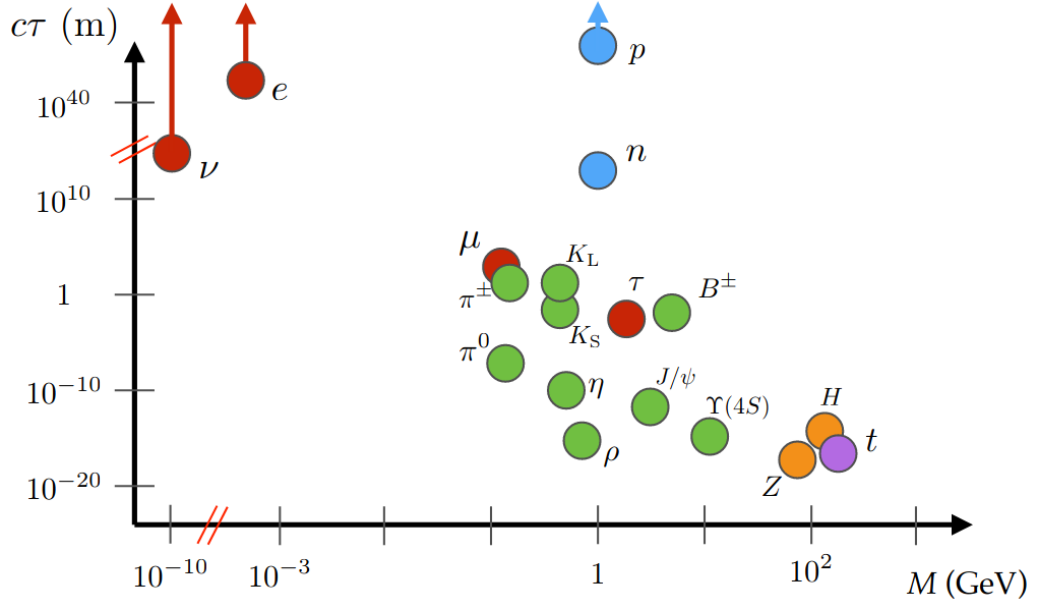


Figure 1.6: Masses and proper decay lengths of many Standard Model particles. Particles with proper decay lengths above approximately  $10^{-4}$  m will be noticeably long-lived in collider detectors such as CMS.

201 collision to particles that propagate through the entire detector. As shown in Fig 1.6,  
202 long-lived particles are common in the SM.

203 Long-lived SM particles arise from several mechanisms. First, symmetries such as  
204 charge and baryon number conservation ensure that particles such as electrons and  
205 protons are absolutely stable. Second, small coupling constants and highly virtual  
206 intermediate states decrease the decay rate of particles such as muons, whose  $2.2\ \mu\text{s}$   
207 lifetime is the product of a weak decay through a virtual  $W$  boson (the  $W$  boson mass  
208 is about 760 times that of the muon). Finally, limited decay phase space increases  
209 the lifetime of particles such as the neutron, whose decay into a proton, an electron,  
210 and an electron neutrino is slowed by the near mass degeneracy of the neutron and

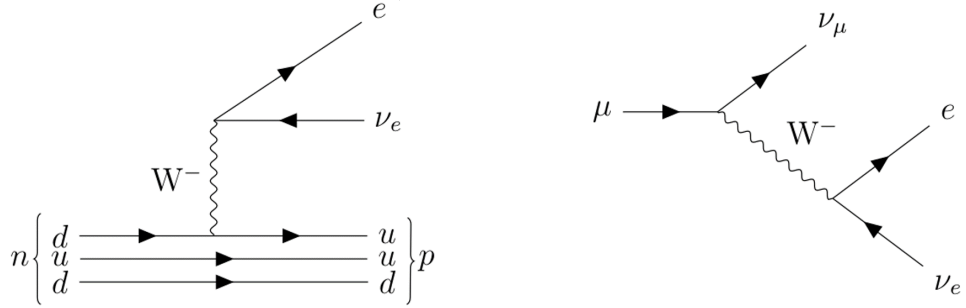


Figure 1.7: Long-lived decays of the neutron (left) and muon (right).

the proton. The mass difference between the neutron and its decay products is less than 1 MeV. The muon and neutron decays are diagrammed in Fig. 1.7.

In BSM physics, the same fundamental mechanisms could very well produce new long-lived particles. Many SUSY scenarios, for example, introduce a symmetry known as R parity that prevents proton decay. In models with exact R-parity conservation, SM particles are assigned R-parity 1 and SUSY particles are assigned R-parity  $-1$ . Conserving the product of R-parity at each vertex has two phenomenological consequences: SUSY particles must be produced in pairs, and the lightest SUSY particle (LSP) must be absolutely stable. A neutral, weakly interacting LSP would therefore pass through most detectors (including the CMS detector described in Section 2.2) without interacting. The resulting momentum imbalance is a standard signature in many SUSY searches [31].

On the other hand, SUSY models with weakly coupled R-parity violating (RPV) terms produce long-lived but not perfectly stable LSPs. The following section will give a detailed overview of one such model. A similar situation arises in gauge-mediated SUSY breaking models where the gravitino is the LSP. The strength of the

227 coupling between the next-to-LSP (NLSP) and the gravitino is inversely proportional  
228 to the energy scale at which SUSY is broken. A high SUSY breaking scale therefore  
229 suppresses the NLSP decay rate, making it long lived [32].

230 LLPs also arise from particular SUSY mass spectra. Models in the Split SUSY  
231 paradigm, for example, propose that the spin-0 SUSY particles are significantly more  
232 massive than the spin- $\frac{1}{2}$  SUSY particles. In these models, the gluino becomes long  
233 lived when its decay to two quarks and a neutral spin- $\frac{1}{2}$  SUSY particle is suppressed  
234 by a highly virtual intermediate squark [33]. Other SUSY models produce long-lived  
235 particles by limiting decay phase space. Some anomaly-mediated SUSY breaking  
236 models, for example, predict that the NLSP and LSP are nearly degenerate in mass.  
237 Just like the neutron decaying into a proton, the lack of available phase space sup-  
238 presses the decay and produces a long-lived NLSP [34].

239 In summary, LLPs are a general feature of the SM, and it is reasonable to assume  
240 that the same mechanisms that produce SM LLPs will also manifest in BSM physics.  
241 The following subsection gives an overview of the phenomenology of the SUSY model  
242 most relevant to the analysis presented in Chapter 3, while the experimental details  
243 of this model and LLP searches at the LHC will be saved until after presenting the  
244 LHC and CMS experiment in Chapter 2.

### 245 1.2.3 Displaced supersymmetry

246 As mentioned in Section 1.2.1, weak-scale SUSY has the potential to explain the  
247 seemingly unnatural observed value of the Higgs boson mass. With this appealing  
248 outcome in mind, experimental physicists have been searching for signs of SUSY  
249 in high-energy particle collisions for the last few decades. In particular, searches

250 at the Large Hadron Collider, where the 7, 8, and 13 TeV proton-proton collisions  
 251 could potentially be producing SUSY particles with masses above 1 TeV, are actively  
 252 excluding large swaths of the natural SUSY parameter space. By examining the  
 253 common assumptions behind a majority of these searches, the proponents of the  
 254 Displaced SUSY model find an approach that avoids proton decay constraints while  
 255 naturally producing long-lived SUSY particles that would be undetected by most  
 256 collider searches [35].

257 Displaced SUSY is an RPV SUSY model that respects proton lifetime constraints  
 258 by allowing terms that violate lepton number but not baryon number. The Minimal  
 259 Supersymmetric Standard Model, which is a simple supersymmetric extension of the  
 260 SM, allows the following baryon and lepton violating operators:

$$\frac{1}{2}\lambda''_{ijk}U_iD_jD_k, \frac{1}{2}\lambda_{ijk}L_iL_jE_k, \lambda'_{ijk}L_iQ_jD_k, \epsilon_iL_iH_u \quad (1.7)$$

261 where the first term violates baryon number and the remaining terms violate lepton  
 262 number. The i, j, and k indices run over the three generations of fermions and  $U$ ,  $D$ ,  $L$ ,  
 263  $E$ ,  $Q$ , and  $H$  refer to the SUSY multiplets whose SM components are right-handed  
 264 up-type quarks, right-handed down-type quarks, left-handed leptons, right-handed  
 265 leptons, left-handed quarks, and Higgs bosons, respectively [29]. Most SUSY models  
 266 introduce R-parity to forbid all of these terms and therefore disallow proton decay,  
 267 but this approach may be overkill: separately conserving either lepton number or  
 268 baryon number is sufficient to prevent proton decay.

269 Such a situation can arise naturally if a gauge-unifying, R-parity-conserving  $SU(5)$   
 270 theory exists at high energies but is broken at lower energies [36]. In this scenario, the  
 271 baryon-number-violating terms are suppressed and mixing between  $L$  and  $H$  becomes  
 272 possible. The final term in expression (1.7) then dominates, and we are left with the

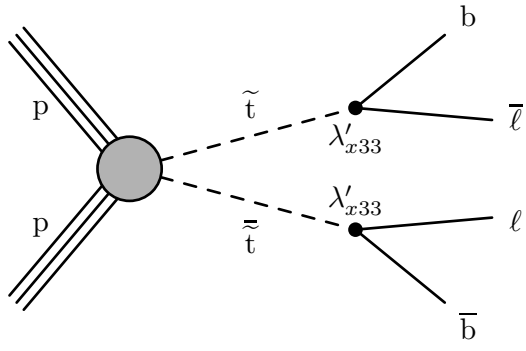


Figure 1.8: Pair-produced top squarks that each decay to a bottom quark and a lepton through an R-parity-violating  $LQD$  vertex.

<sup>273</sup> following lepton-number-violating terms after rotating to the mass basis:

$$\epsilon_i y_{jk}^d L_i Q_j D_k, \quad \epsilon_i y_{jk}^e L_i L_j E_k \quad (1.8)$$

<sup>274</sup> where the  $\epsilon$  factors are lepton-Higgs mixing angles and the  $y$  factors are the SM  
<sup>275</sup> Yukawa coupling constants. The presence of the Yukawa coupling constants implies  
<sup>276</sup> that lepton-violating processes will favor third-generation fermions.

<sup>277</sup> The dimensionless lepton-Higgs mixing angles are protected by the custodial R-  
<sup>278</sup> parity conservation of the higher-energy theory and can therefore naturally be small.  
<sup>279</sup> Just as in the SM, these small coupling constants can lead to macroscopic SUSY  
<sup>280</sup> particle lifetimes that would evade most collider searches. In particular, long-lived  
<sup>281</sup> LSP squarks can decay to a quark and charged lepton though a displaced vertex, as  
<sup>282</sup> in Fig. 1.8.

<sup>283</sup> The unique experimental signature of processes such as the one shown in Fig. 1.8 is  
<sup>284</sup> a major motivating factor behind the analysis presented in Chapter 3. The particular  
<sup>285</sup> experimental consequences of such processes will be further explored in that context.

## 286 Chapter 2: The Large Hadron Collider and Compact Muon 287 Solenoid experiment

## **288** 2.1 The Large Hadron Collider

The Large Hadron Collider (LHC) is the highest-energy particle collider ever constructed. Located at the European Organization for Nuclear Research (CERN) and housed in a 27 km ring approximately 100 m below the French/Swiss countryside, the LHC is designed to accelerate two counter-rotating beams of protons to 7 TeV (and sometimes beams of heavy ions to 2.8 TeV) and collide them at four points around the ring. Each collision point is instrumented with a dedicated detector: the ATLAS (A Toroidal LHC Apparatus) and CMS (Compact Muon Solenoid) experiments are general purpose detectors designed to reconstruct the remnants of proton-proton collisions at the highest collision rates offered by the LHC, LHCb (LHC beauty) studies b-quark decays from proton-proton collisions produced at lower collision rates, and ALICE (A Large Ion Collider Experiment) studies heavy-ion collisions [3]. Figure 2.1 shows the location of each experiment around the LHC ring. The analysis presented in Chapter 3 utilizes proton-proton collision data collected by the CMS experiment, and the following discussion is focused accordingly.

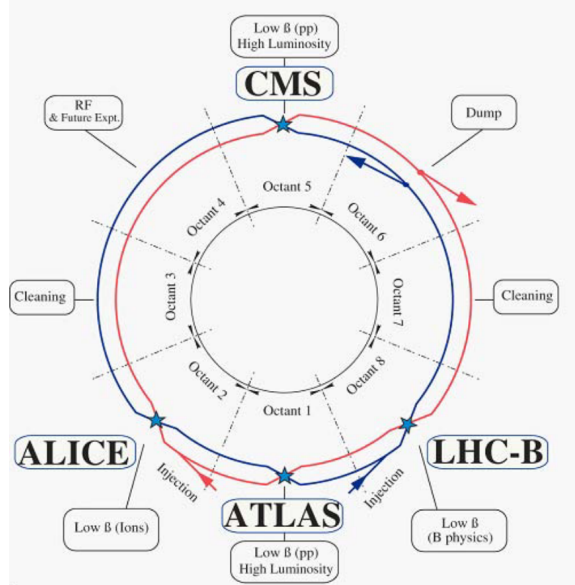


Figure 2.1: Layout of the LHC experiments [3].

### **2.1.1 Injection chain**

The protons ultimately collided by the LHC must first travel through much of the CERN accelerator complex, which is diagrammed in Fig. 2.2. The 6.5 TeV proton beams relevant to this thesis start their journey as the nuclei of hydrogen atoms in a bottle of hydrogen gas. After having their electrons stripped away with an electric field, the protons are accelerated to an energy of 50 MeV with the Linac 2 linear accelerator [37]. The Proton Synchrotron Booster (PSB) next accelerates the protons to an energy of 1.4 GeV before injecting them into the Proton Synchrotron (PS) [38]. The PS was the first synchrotron constructed at CERN and was the highest-energy particle accelerator in the world at the time of its first operation [39]. Today, it accelerates protons to an energy of 25 GeV before passing them along to the Super Proton Synchrotron (SPS), which is the 7 km proton-antiproton collider at which the

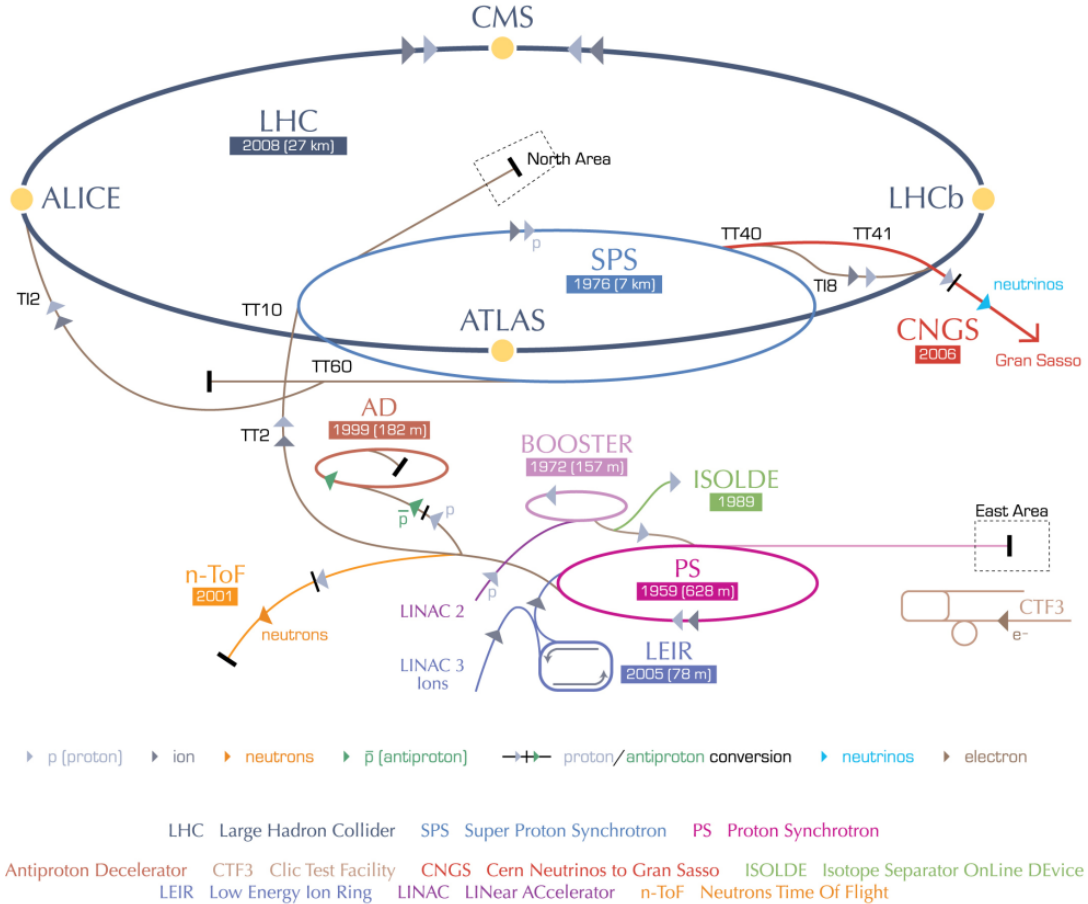


Figure 2.2: A diagram of the CERN accelerator complex. The analysis presented in Chapter 3 utilizes protons accelerated by LINAC 2, BOOSTER (also known as PSB), PS, SPS, and finally the LHC before their ultimate collision inside CMS [4].

<sup>315</sup> W and Z bosons were discovered in 1983 [40]. As the final step in the LHC injection  
<sup>316</sup> chain, SPS accelerates protons to an energy of 450 GeV before injecting them into  
<sup>317</sup> the LHC [3].

### <sup>318</sup> 2.1.2 Main ring

<sup>319</sup> Maximizing the physics potential of the LHC requires simultaneously maximizing  
<sup>320</sup> the collision energy and the number of interesting collisions per unit time. The main

Table 2.1: Luminosity parameters used in Eq. (2.1).

Parameter	Description
$N_b$	Number of particles per bunch
$n_b$	Number of bunches per beam
$f_{rev}$	Revolution frequency
$\gamma_r$	Relativistic gamma factor
$\epsilon_n$	Normalized transverse beam emittance
$\beta^*$	Beta function at collision point
$F$	Geometric luminosity reduction factor

321 LHC ring is therefore designed to accelerate the 450 GeV protons it receives from  
 322 SPS to 7 GeV and collimate them into intense beams to be collided at high rates.  
 323 The number of interesting collisions per unit time is ultimately the product of the  
 324 total cross-section of the processes one deems interesting,  $\sigma$ , and the instantaneous  
 325 luminosity,  $L$ , which is given by:

$$L = \frac{N_b^2 n_b f_{rev} \gamma_r}{4\pi \epsilon_n \beta^*} F \quad (2.1)$$

326 where the parameters are defined as in Table 2.1 [3].

327 The LHC is designed to deliver a maximum instantaneous luminosity of  
 328  $10^{34} \text{ cm}^{-2} \text{ s}^{-1}$  to ATLAS and CMS, but operational improvements, most notably a  
 329 reduction in  $\epsilon_n$  and  $\beta^*$ , have allowed the LHC to exceed this goal by up to a factor of  
 330 approximately two in the 2016, 2017, and 2018 data-taking periods [5]. As shown in  
 331 Fig. 2.3, the total integrated luminosity delivered during this period is approximately  
 332 a factor of five times greater than that of the 2011–2012 period.

333 The ability to produce high-energy proton collisions at such high rates depends  
 334 on several impressive technological feats, notably the superconducting magnets that

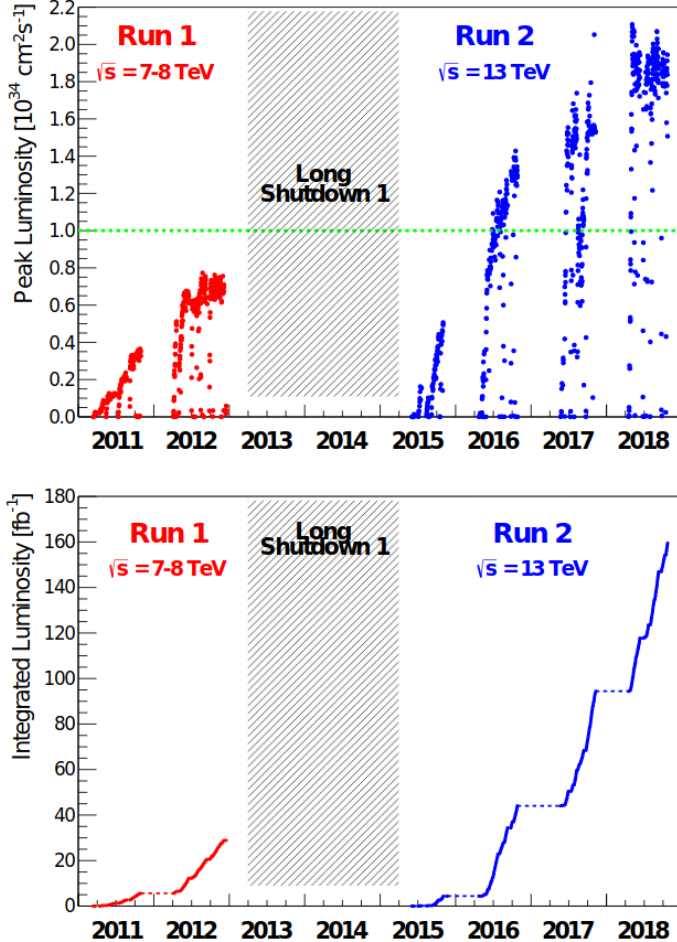


Figure 2.3: The peak instantaneous (top) and integrated (bottom) luminosity delivered by the LHC during proton operation between 2011 and 2018 [5].

335 steer and shape the beams and the superconducting radio-frequency (RF) cavities  
 336 that accelerate the protons and determine their bunch structure.

### 337 Superconducting magnets

338 The LHC magnet system relies on superconducting NbTi magnets that are cooled  
 339 to below 2K with superfluid helium and are capable of producing fields in excess  
 340 of 8 T. The design of the main dipole magnets that are responsible for keeping the

## LHC DIPOLE : STANDARD CROSS-SECTION

CERN AC/DI/MM - HE107 - 30.04.1999

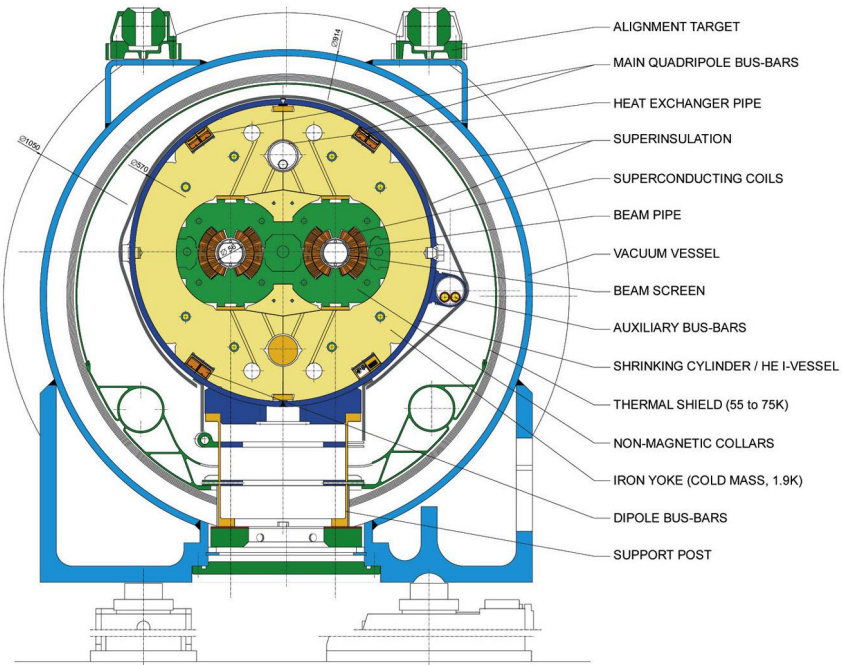


Figure 2.4: Diagram of an LHC dipole magnet in cross-section [6].

341 beams in a circular trajectory is heavily influenced by the size of the LHC tunnel,  
 342 which originally housed the Large Electron-Positron Collider (LEP). Unlike LEP,  
 343 which collided particles and antiparticles, the LHC requires two separate beam pipes,  
 344 each with its own dipole magnetic field. This requirement, along with the limited  
 345 tunnel cross section, motivates the "two-in-one" magnet design in which both super-  
 346 conducting magnets share a common cold mass and cryostat, as shown in Fig. 2.4  
 347 [3].

348 In addition to the main dipole magnets, the LHC also employs quadrupole magnets  
 349 for beam focusing and sextupole, octupole, and decapole magnets to correct the field  
 350 at the edges of the dipoles [3].

351 **Radio-frequency cavities**

352 An RF superconducting cavity system is responsible for capturing the 450 GeV  
353 protons injected into the LHC from SPS, accelerating them to the full collision energy,  
354 defining their bunch structure, and storing them. The main RF system operates  
355 at 400 MHz and is located in Octant 4 (see Fig.2.1). Each RF cavity contains an  
356 oscillating electromagnetic field whose phase is synchronized with the arrival of the  
357 proton bunches such that the protons passing through the cavity always feel a force  
358 in the direction of their motion. The applied force naturally varies for protons that  
359 are slightly out of phase in such a way as to keep the protons tightly bunched in the  
360 longitudinal direction [3].

361 **2.2 The Compact Muon Solenoid experiment**

362 The Compact Muon Solenoid experiment (CMS) is designed for the general study  
363 of the highest-energy, highest-luminosity proton-proton (and heavy ion) collisions the  
364 LHC can provide. The detector design is driven by the particular goals of exploring  
365 physics at the TeV scale and discovering the origin of electroweak symmetry breaking  
366 [41]. More than 4000 collaborators from institutions across more than forty countries  
367 work together to collect and analyze the data using a global computing grid [42].

368 To reconstruct the variety of particles that emerge from high-energy proton-proton  
369 collisions, CMS uses several complimentary subdetectors nested radially about the  
370 collision point. A 4 T superconducting solenoid magnet provides a powerful magnetic  
371 field to bend the trajectories of charged particles, thus enabling the determination  
372 of their momenta. Working from the center out, the CMS detector consists of an  
373 all-silicon tracker, a lead-tungstate scintillating crystal electromagnetic calorimeter,  
374 a sampling hadronic calorimeter composed of brass absorber and plastic scintillator  
375 tiles, the superconducting solenoid magnet, and a muon system with three varieties  
376 of gaseous detectors. Figure 2.5 shows the detector layout, and the remainder of this  
377 chapter is devoted to a brief overview of each subsystem as well as the triggering and  
378 reconstruction strategies employed by CMS.

379 CMS uses a right-handed coordinate system centered on the nominal collision  
380 point with positive  $x$  direction pointing towards the center of the LHC ring and the  
381 positive  $y$  direction pointing vertically upward. The azimuthal angle in the  $x$ - $y$  plane,  
382 denoted  $\phi$ , is measured from the positive  $x$  axis, and the polar angle  $\theta$  is measured  
383 from the positive  $z$  axis. The angle from the  $z$  axis is more commonly described  
384 in terms of the pseudorapidity  $\eta = -\ln \tan(\theta/2)$ . Distances in the  $\eta$ - $\phi$  plane are

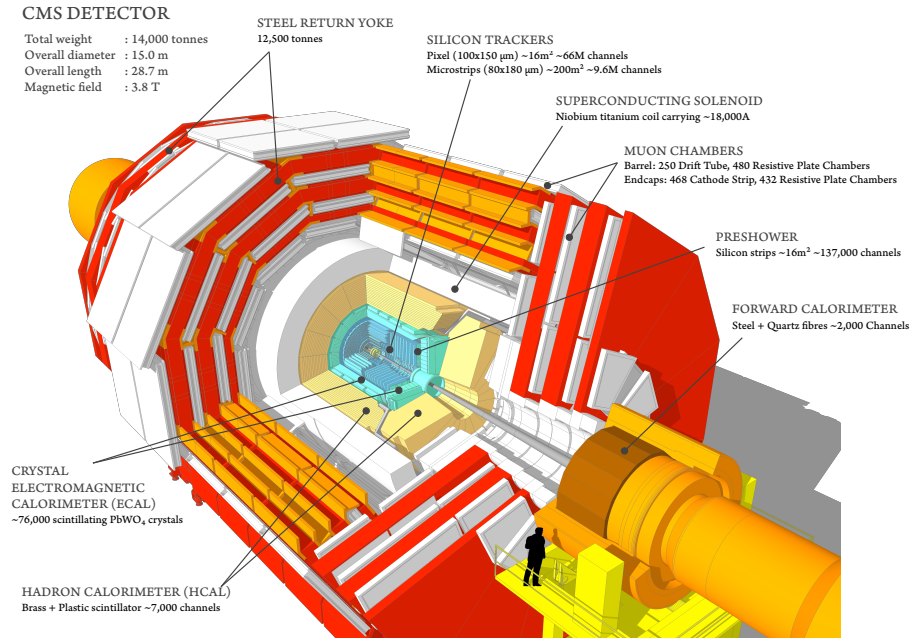


Figure 2.5: The CMS detector [7].

385 commonly referred to as  $\Delta R = \sqrt{(\Delta\eta)^2 + (\Delta\phi)^2}$ . The component of the momentum  
 386 that is transverse to the beam direction (i.e., in the  $x$ - $y$  plane) is denoted  $p_T$ , and the  
 387 magnitude of the negative vector sum of the  $p_T$  of all the reconstructed particles in  
 388 an event is denoted  $p_T^{\text{miss}}$  [12, 8].

389 The CMS detector has undergone several upgrades since its initial construction.  
 390 The description presented here will focus on the detector conditions relevant to the  
 391 analysis presented in Section 3.

### 392 2.2.1 Solenoid magnet

393 The superconducting solenoid is designed to produce a 4 T magnetic field through-  
 394 out the 6.3 m diameter, 12.5 m long cylindrical volume that contains the tracker and  
 395 calorimeters. The magnetic field is produced by running 19 kA through 2168 turns

396 of NbTi superconducting cable that are cooled with liquid helium. The flux returns  
397 through an iron yoke that also houses the muon system [8].

398 The strong magnetic field is critical to CMS’s ability to unambiguously distinguish  
399 muons and anti-muons with transverse momenta up to 1 TeV [12], and much of the  
400 overall detector design is guided by the choice of a large superconducting solenoid.  
401 The uniform magnetic field alters the trajectories of charged particles immediately  
402 upon their production, which results in significant bending power within a relatively  
403 small radius and therefore enables a compact detector.

404 The CMS solenoid stores a uniquely large amount of energy in its magnetic field  
405 when compared to other collider detector magnets, especially when viewed relative to  
406 its mass. To avoid deformations from the strong magnetic field, the superconducting  
407 coils are reinforced with an aluminium alloy so that the coil layers themselves han-  
408 dle 70% of the magnetic hoop stress. Figure 2.6 compares several collider detector  
409 magnets in the energy/mass vs energy plane and shows a cross-sectional view of the  
410 reinforced conductor coils in cross section. This approach allows for a relatively thin  
411 solenoid that is less likely to scatter muons before they reach the muon system [8].

### 412 2.2.2 Tracker

413 In the region closest to the proton collisions, CMS employs a silicon tracker to re-  
414 construct particle trajectories along with primary and secondary vertices. Efficiently  
415 and accurately performing these tasks allows CMS to measure charged particle mo-  
416 menta, distinguish between particles from the primary and pileup vertices, and iden-  
417 tify heavy-flavor decays. The high particle flux necessitates a highly granular, fast,  
418 and radiation hard detector that introduces the smallest possible amount of material

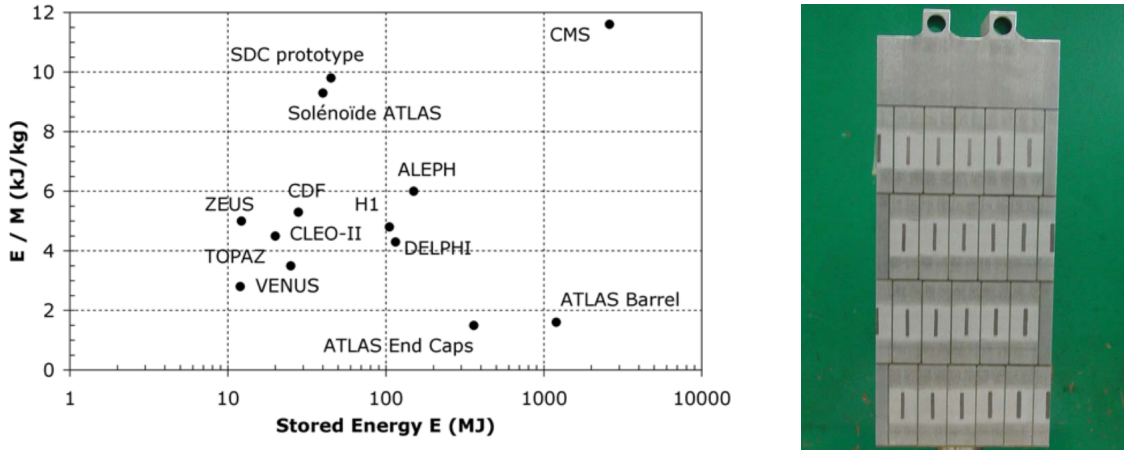


Figure 2.6: The stored-energy-over-mass ratio,  $E/M$ , for several detector magnets (left), and a cross-sectional view of the four-layer winding of reinforced conductor in the CMS superconducting solenoid (right) [8].

419 to the region inside the calorimeters. The resulting detector contains over  $200\text{ m}^2$  of  
 420 active silicon, making it the largest silicon tracker ever built. The tracker has a length  
 421 of  $5.8\text{ m}$ , a diameter of  $2.5\text{ m}$ , and is divided into two subdetectors. Inside a radius  
 422 of  $20\text{ cm}$ , the particle flux demands the use of silicon pixel detectors, while silicon  
 423 micro-strip detectors suffice in the region beyond  $20\text{ cm}$  [8].

424 The pixel and strip detectors both utilize the same fundamental detection mech-  
 425 anism: the energy depositions of incident charged particles form electron-hole pairs  
 426 when passing through the depletion region of a reverse-biased p-n junction, and the  
 427 resulting induced current signifies the presence of a charged particle. The reverse bias  
 428 voltage sweeps away charge carriers to reduce thermal noise and maximize the sen-  
 429 sitive volume. The fine two-dimensional segmentation of the pixel detector provides  
 430 precise two-dimensional position measurements from a single detector layer, while  
 431 each strip detector layer only provides a one-dimensional location measurement. In

432 both cases, the detector planes are tilted to allow the charge liberated by a single  
433 incident particle to spread across multiple pixels or strips. This scheme significantly  
434 improves the position resolution by combining the charge measurements of multiple  
435 adjacent pixels or strips.

436 The original pixel detector was replaced between the 2016 and 2017 data-taking  
437 periods in preparation for higher luminosities [10]. As the analysis presented in Sec-  
438 tion 3 uses data collected in 2016–2018 and is particularly dependent on tracker  
439 measurements, the original pixel detector, 2017–2018 (Phase-1) pixel detector, and  
440 strip detector are described separately below.

441 **Original pixel detector**

442 The original CMS pixel detector covers the  $|\eta| < 2.5$  region and is composed of  
443 three cylindrical barrel layers at  $r = 4.4$ , 7.3, and 10.2 cm and four endcap disks 34.5  
444 and 46.5 cm up and down the beamline from the nominal collision point. Each layer  
445 or disk is instrumented with several pixel modules that are composed of a silicon  
446 sensor bump bonded to custom ASIC read-out chips (ROCs). Each sensor is 285  $\mu\text{m}$   
447 thick and typically comprises 66 560  $100 \times 150 \mu\text{m}$  pixels. The nearly square pixel  
448 shape enables approximately 15  $\mu\text{m}$  hit resolution in both the  $r$ - $\phi$  and  $z$  directions  
449 [12, 8].

450 The original pixel detector was designed for a maximum instantaneous luminosity  
451 of  $10^{34} \text{ cm}^{-2} \text{ s}^{-1}$ , which corresponds to approximately 25 pileup collisions per bunch  
452 crossing in CMS. As shown in Fig. 2.3, the LHC first exceeded this instantaneous  
453 luminosity in 2016. Figure 2.7 shows the resulting hit efficiency loss in the innermost  
454 layer of the pixel detector as a function of instantaneous luminosity and number of  
455 pileup collisions per bunch crossing. While the higher-radius pixel layers are less

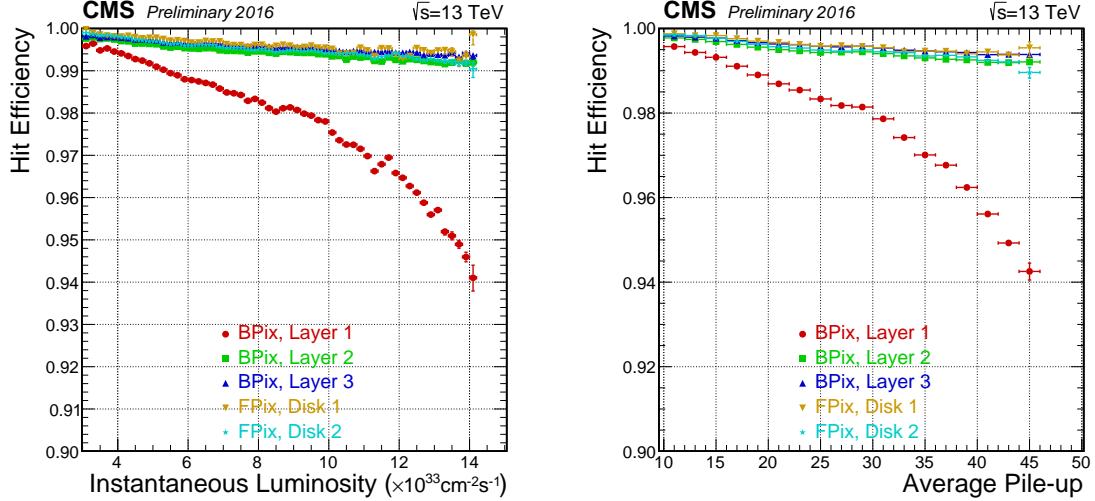


Figure 2.7: Measured single hit efficiency per layer as a function of the instantaneous luminosity (left) and inelastic collisions per bunch crossing (right) in data taken with the original CMS pixel detector in 2016 [9].

456 affected, important quantities such as the transverse impact parameter resolution are  
 457 highly dependent on the measurements of the layer closest to the interaction. To  
 458 mitigate this effect, CMS replaced the original pixel detector between the 2016 and  
 459 2017 data-taking periods.

#### 460 Phase-1 pixel detector

461 The Phase-1 pixel detector represents an incremental improvement over the orig-  
 462 inal CMS pixel detector: the same fundamental technology fills the same physical  
 463 footprint and reuses many of the existing services but nevertheless achieves higher  
 464 rate capabilities, improved radiation tolerance, and more robust tracking [10]. This is  
 465 achieved by adding one additional layer to the barrel and each endcap, decreasing the  
 466 radius of the innermost barrel layer to 2.9 cm, upgrading the ROCs, and reducing the

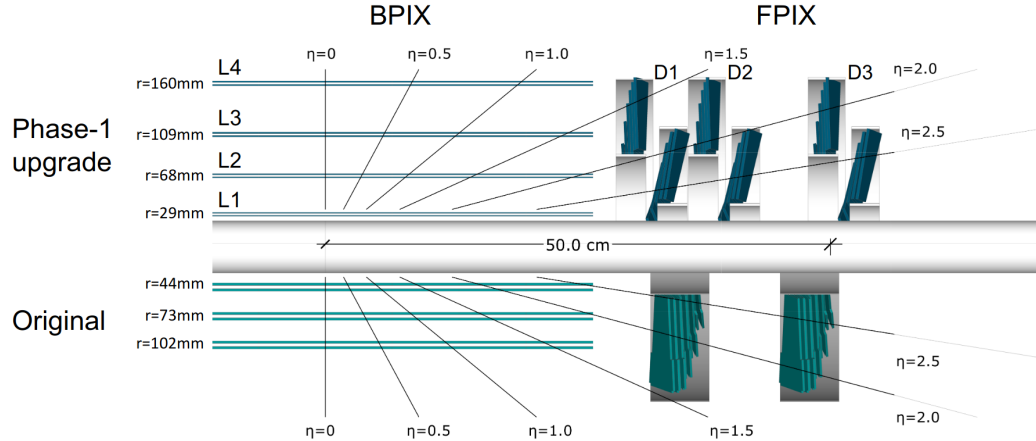


Figure 2.8: Comparison of the original and Phase-1 CMS pixel detector layouts in  $y$ - $z$  plane [10].

material budget of the cooling system and mechanical structure [10, 43]. Figure 2.8 compares the geometries of the original and Phase-1 pixel detectors.

The loss of hit efficiency at high instantaneous luminosity observed in the original pixel detector is significantly reduced in the Phase-1 pixel detector. Despite the higher particle flux that accompanies the shift to a smaller radius, the Phase-1 innermost pixel layer maintains a single hit efficiency well over 98 % when operating at an instantaneous luminosity of  $1.4 \times 10^{34} \text{ cm}^{-2} \text{ s}^{-1}$  during the 2017 data-taking period [44]. Looking at Fig. 2.7, the equivalent quantity for the original pixel detector is approximately 94 %.

#### 476 Strip tracker

The strip tracker surrounds the pixel detector with silicon micro-strip sensors in 10 cylindrical barrel layers between  $r = 20 \text{ cm}$  and  $r = 110 \text{ cm}$  and 12 disks on each side of the barrel detector that extend to  $|z| < 282 \text{ cm}$  and cover up to  $|\eta| < 2.5$ .

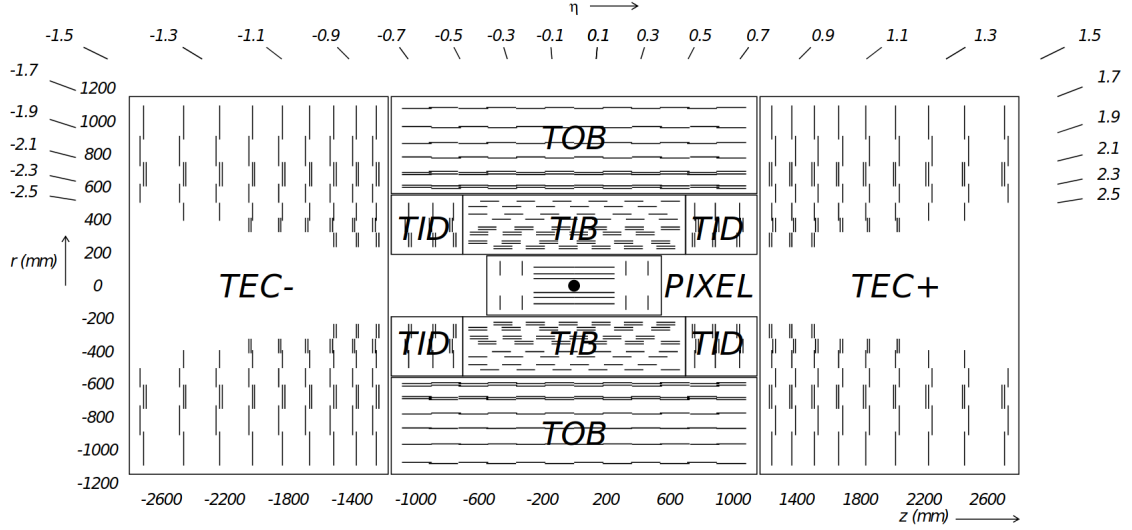


Figure 2.9: Layout of the CMS silicon tracker. TIB, TOB, TID, and TEC refer to subdetectors of the strip detector while PIXEL refers to the original pixel detector. The Phase-1 pixel detector is contained within the same volume [8].

480 The strip pitch generally increases with radius and results in hit resolutions that vary  
 481 from 23 to 530  $\mu\text{m}$  [8]. Figure 2.9 shows the layout of the entire silicon tracker.

### 482 2.2.3 Electromagnetic calorimeter

483 After traversing the inner tracker, particles next encounter the electromagnetic  
 484 calorimeter (ECAL). As a homogeneous scintillation calorimeter, ECAL uses 61 200  
 485 lead tungstate crystals in the barrel and 7324 in each endcap to reconstruct the en-  
 486 ergy deposited during electromagnetic showers. Lead tungstate crystals allow for  
 487 a fast (80 % of light emitted within 25 ns), compact (radiation length = 0.89 cm),  
 488 fine-grained (Molière radius = 2.2 cm), and radiation hard (up to 10 Mrad) calorime-  
 489 ter. The main drawback is the relatively low light yield (30 photon/MeV), which  
 490 necessitates photodetectors with intrinsic gain that work in magnetic fields [8, 12].

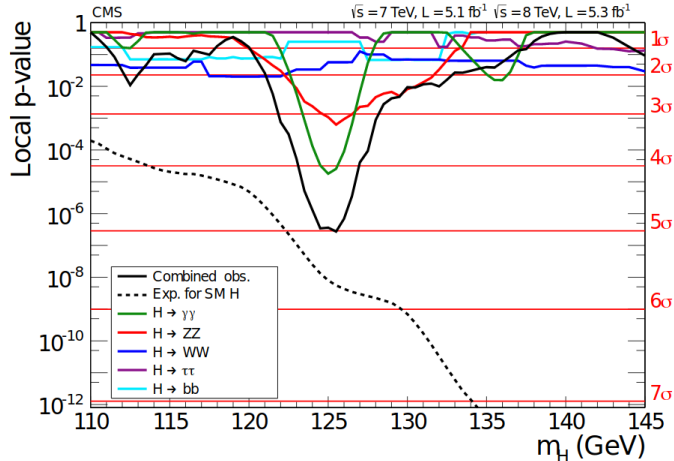


Figure 2.10: The observed local p-value for the five decay modes and the overall combination as a function of the SM Higgs boson mass showing the importance of the ECAL mass resolution in the discovery of the Higgs boson by the CMS experiment. The dashed line shows the expected local p-values for a SM Higgs boson with a mass  $m_H$  [11].

The ECAL performance requirements were heavily influenced by the possibility to reconstruct the decay of a Higgs boson to two photons [41]. Despite the small branching fraction and irreducible background, this decay channel provides a clean signature of a narrow mass peak on top of a smoothly falling background. Thanks in large part to the excellent ECAL energy resolution, the diphoton channel provided the largest significance and best mass resolution (approximately 1 GeV resolution at 125 GeV) in the CMS Higgs boson discovery in 2012, as shown in Fig. 2.10 [11].

The barrel section extends radially from 129 to 177 cm and covers up to  $|\eta| < 1.479$ . The crystals are tapered to approximately project back to the nominal collision point but not so perfectly that likely particle trajectories align with cracks. Each crystal is approximately one Molière radius wide and 25 radiation lengths deep. The crystals

502 in each endcap section are arranged in an  $x$ - $y$  grid that starts at  $|z| = 315$  cm and  
503 covers  $1.479 < |\eta| < 3.0$ .

#### 504 2.2.4 Hadronic calorimeter

505 Particles that survive the ECAL will next encounter the hadronic calorimeter  
506 (HCAL). As the ECAL constitutes approximately 25 radiation lengths but only one  
507 interaction length, all but the particles that decay through the strong force will be  
508 filtered out before reaching the HCAL. In addition to reconstructing the decays of  
509 hadrons, the HCAL plays a particularly important role in measuring  $p_T^{\text{miss}}$ . By max-  
510 imizing the coverage in  $\eta$  and overall amount of material in terms of interaction  
511 lengths, HCAL ensures that nearly all particles (other than muons, neutrinos, and  
512 hypothetical BSM particles) decay and deposit all their energy before reaching the  
513 solenoid. Muon momentum is reconstructed with the tracker and muon system, so  
514 only neutrinos and hypothetical BSM particles will contribute to  $p_T^{\text{miss}}$ . Reliable  $p_T^{\text{miss}}$   
515 measurements are particularly important when searching for new weakly interacting  
516 particles with large lifetimes such as potential dark matter candidates or R-parity-  
517 conserving LSPs.

518 With these goals and the constraint of fitting within the solenoid volume in mind,  
519 HCAL is designed as a sampling calorimeter that uses 3.7 mm thick plates of plastic  
520 scintillator interspersed within approximately 5 cm thick brass absorber plates to  
521 reconstruct the energy deposited during hadronic showers. Embedded wavelength-  
522 shifting fibers capture the scintillation light and transfer it to clear fibers to be read  
523 out by hybrid photodiodes.



Figure 2.11: Layout of the hadron calorimeter barrel (HB), outer (HO), endcap (HE), and forward (HF) subdetectors [8].

524     The barrel section ( $|\eta| < 1.4$ ) is segmented into 32 towers in  $\eta$  and 64 in  $\phi$  that  
 525    each contain 17 active scintillator layers. In the  $|\eta| < 1.26$  range, an extra layer  
 526    of scintillator tiles (or two at  $\eta = 0$ ) sits just outside the solenoid and increases  
 527    the minimum effective HCAL interaction length to greater than 11.8. Each endcap  
 528    spans a pseudorapidity range of 1.3 to 3.0 with 14 towers in eta and 5 to 10°  $\phi$   
 529    segmentation. Also, a steel and quartz fiber forward calorimeter (HF) sits 11.2 m from  
 530    the interaction point and covers  $3 < |\eta| < 5$ . In HF, particles produce Cherenkov  
 531    light when traversing the quartz fibers that run parallel to the beamline. Figure 2.11  
 532    shows the layout of the barrel, endcap, and forward HCAL subdetectors.

### 533    **2.2.5 Muon system**

534     The CMS muon system is composed of three varieties of gaseous detectors em-  
 535    bedded in the iron return yoke outside the superconducting solenoid. In the central

536 region ( $|\eta| < 1.2$ ), the low muon and neutron rates along with the lower magnetic field  
537 allow the use of drift tube (DT) chambers. At higher  $\eta$  ( $0.9 \leq |\eta| < 2.4$ ), cathode  
538 strip chambers (CSCs) are required to handle the higher rates and larger magnetic  
539 field. Finally, resistive plate chambers (RPCs), which provide more accurate time  
540 measurements and worse spatial resolution than the DTs and CSCs, complement the  
541 other detectors out to  $|\eta| < 1.9$  [12, 45].

542 As shown in Fig. 2.12, the muon momentum resolution of the inner tracker is about  
543 an order of magnitude better than that of the muon system for low- $p_T$  muons. The  
544 muon system is critical, however, for maintaining the  $< 10\%$  momentum resolution  
545 that is necessary to unambiguously differentiate muons and anti-muons up to 1 TeV.  
546 In addition to improving muon reconstruction, the muon system provides information  
547 to the L1 trigger (see Section 2.2.6) and is capable of triggering on muons with good  
548 efficiency, high background rejection, and about 15–25%  $p_T$  resolution without input  
549 from the rest of the detector.

550 The DTs are organized into four stations, each of which contain up to 70 DT  
551 chambers that each measure the muon hit position in either the  $r$ - $\phi$  or  $z$  direction.  
552 Each chamber is composed of two or three collections of four-layer groupings of 13  
553 by 42 mm drift cells. As diagrammed in Fig. 2.13, a 2–4 m anode wire runs down the  
554 center of each drift cell while electrode and cathode strips line the top, bottom,  
555 and walls of the cell. The cells are filled with an Ar/CO<sub>2</sub> gas mixture that is ionized  
556 by charged particles traversing the cell. The liberated electrons cause avalanches in  
557 the large electric fields before being collected by the anode wire.

558 Each endcap contains four CSC stations, each with six layers of CSCs whose cath-  
559 ode strips run radially outward to provide muon hit position measurements in the  $r$ - $\phi$

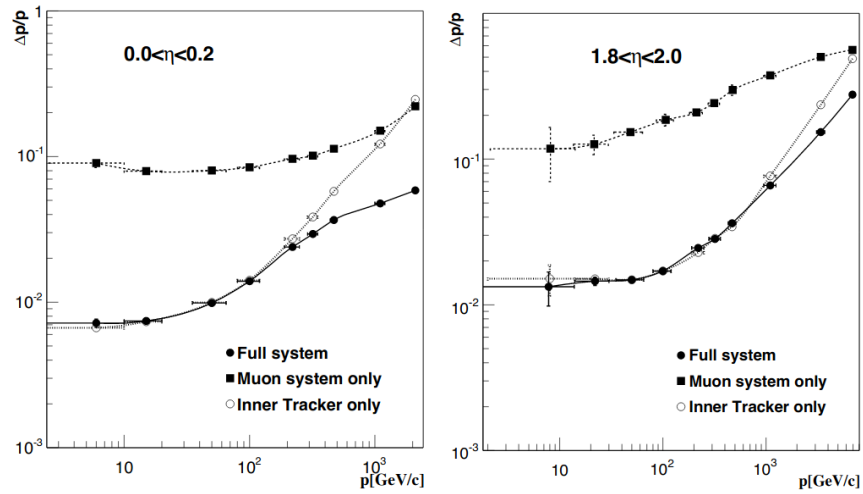


Figure 2.12: Muon momentum resolution as a function of momentum when using the CMS muon system, the CMS inner tracker, and the combination of the two subdetectors in two different  $\eta$  ranges [12].

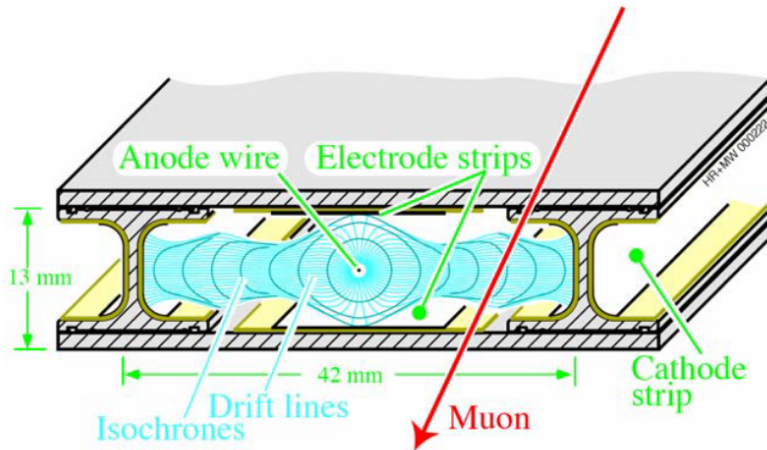


Figure 2.13: Sketch of a CMS muon system drift cell showing drift lines and isochrones. The plates at the top and bottom of the cell are at ground potential while the voltages applied to the electrodes are +3600 V for wires, +1800 V for strips, and -1200 V for cathodes [8].

560 plane while the anode wires run in the azimuthal direction to provide measurements  
561 in  $\eta$ . As in the DTs, charged particles ionize a gas mixture inside each chamber (this  
562 time an Ar/CO<sub>2</sub>/CF<sub>4</sub> mixture), which leads to an avalanche of electrons that are col-  
563 lected by an anode wire. In the CSCs, however, several anode wires share the same  
564 chamber and a two-coordinate position measurement is obtained by also reading out  
565 the induced charge on the perpendicular cathode strips.

### 566 2.2.6 Trigger

567 The trigger reduces the data writing rate from the 40 MHz collision rate to less  
568 than 1 kHz so that events can be written to tape. The rate reduction happens in  
569 two stages: Level-1 (L1) and High-Level Trigger (HLT). L1 analyzes input from  
570 ECAL, HCAL, and the muon system with custom electronics to reduce the rate to  
571 approximately 100 kHz in 3.8  $\mu$ s. With input from all subdetectors, the HLT then  
572 uses a dedicated processor farm to further reduce the rate to the desired < 1 kHz  
573 [8, 46].

### 574 2.2.7 Physics object reconstruction

575 CMS uses a particle-flow (PF) algorithm to reconstruct the properties of individ-  
576 ual particles from the combination of all subdetector measurements. Starting from  
577 charged particle tracks from the tracker and muon system and clusters of energy  
578 deposited in the ECAL and HCAL, CMS’s PF algorithm aims to reconstruct all  
579 final-state electrons, muons, photons, and charged and neutral hadrons in a given  
580 event. In this section, I first describe the reconstruction of tracks and energy clus-  
581 ters before moving on to the individual particle identification and reconstruction. A  
582 complete description of the CMS PF algorithm is available in Ref. [13].

583 **Charged particle tracks**

584     Charged particle tracks are reconstructed with an iterative procedure. Despite the  
585     middling reconstruction efficiency of each individual step, starting with the highest-  
586     purity algorithms and masking the hits associated with each reconstructed track be-  
587     fore moving on to the next step results in higher efficiency than could be achieved  
588     with any single tracking algorithm without increasing the rate of misreconstruction.  
589     This general principle applies to all charged particle tracks, but the tracks associated  
590     with candidate electrons and muons receive special consideration.

591     To better handle electron trajectories affected by radiative energy loss, CMS em-  
592     ploys a special iterative tracking procedure that includes a Gaussian-sum filter (GSF)  
593     [47]. This approach improves the overall reconstruction efficiency, allows reconstruc-  
594     tion of lower- $p_T$  electrons, and helps identify electrons from photon conversions and  
595     distinguish electrons from charged hadrons.

596     Muon track reconstruction benefits from measurements in the tracker and the  
597     muon system. Candidate muon tracks are placed in one of three categories depending  
598     on which subdetectors are used in their reconstruction: standalone muon tracks only  
599     use muon system hits; tracker muon tracks only use tracker hits and the requirement  
600     of at least one consistent muon system hit; and global muon tracks are reconstructed  
601     from a global fit of tracker and muon system hits.

602 **Calorimeter energy clusters**

603     Energy deposits in the calorimeters are clustered separately in ECAL and HCAL  
604     with a Gaussian-mixture model that assumes the energy deposits arise from an arbi-  
605     trary number of Gaussian energy deposits whose amplitude and location are allowed

606 to vary while the width is determined by the calorimeter properties. The clusters are  
607 first seeded by cells with energy above some threshold and greater than the energy  
608 of the surrounding cells. Nearby clusters are then merged before being fed to the  
609 Gaussian-mixture algorithm. Finally, several corrections are applied to the cluster  
610 energies to ensure accurate responses to photons and hadrons.

611 **Particle-flow reconstruction**

612 The tracks and clusters are then identified with and used to reconstruct all in-  
613 dividual particles in an event. The first step is to link tracks and clusters together  
614 into groups that correspond one or a few particles. Tracker tracks are extrapolated  
615 outwards and linked with the nearest ECAL and HCAL clusters that are within a  
616 set radius in the  $\eta$ - $\phi$  plane. In the case of candidate electron tracks, tracker tracks  
617 and ECAL deposits consistent with electron radiative losses are also linked with the  
618 candidate electron track. ECAL and HCAL clusters are similarly linked together by  
619 proximity in the  $\eta$ - $\phi$  plane. Due to the high granularity of CMS subdetectors, the  
620 number of tracks and clusters in a linked group is largely independent of the total  
621 number of particles in an event.

622 Each group of linked tracks and clusters is then processed by the PF particle  
623 identification and reconstruction algorithm. As in track reconstruction, particle re-  
624 construction is an iterative process in which the tracks and clusters are masked after  
625 being associated with a particle. Figure 2.14 diagrams the basic concept used to  
626 identify muons, electrons, photons, and charged and neutral hadrons. Each step of  
627 the PF algorithm is summarized below.

628 Muons are reconstructed first from isolated global muon candidates, then non-  
629 isolated global muon candidates, and finally tracker muon (standalone muon) can-  
630 didate tracks that are particularly well measured and consistent with hits in the  
631 muon system (tracker). Muon momentum is taken from the tracker track when  
632  $p_T < 200 \text{ GeV}$  and from the combination of tracker and muon system hits that yields  
633 the best fit otherwise.

634 Electron and isolated photon reconstruction, which occur together after muon  
635 reconstruction, are necessarily interrelated by the high probability that an electron  
636 radiates a photon or a photon pair-produces electrons when interacting with tracker  
637 material. Electrons are identified from GSF tracks with a corresponding ECAL cluster  
638 while isolated photons are identified from isolated ECAL clusters. The total electron  
639 energy accounts for radiative losses that show up as ECAL clusters, and both electrons  
640 and isolated photons require a high ratio of ECAL cluster energy to nearby HCAL  
641 cluster energy.

642 Next, nonisolated photons and charged and neutral hadrons are reconstructed  
643 from the remaining tracks and clusters. Within the tracker acceptance ( $|\eta| < 2.5$ ),  
644 ECAL (HCAL) clusters without associated tracks are identified as photons (neutral  
645 hadrons). At higher  $\eta$ , nearby ECAL and HCAL clusters are assumed to arise from the  
646 same hadron shower and ECAL clusters without nearby HCAL clusters are identified  
647 as photons. Discrepancies between track momenta and associated HCAL cluster  
648 energy are also used to identify neutral hadrons and muons. Finally, a post-processing  
649 step corrects for rare failure modes that can potentially produce inaccurately large  
650  $p_T^{\text{miss}}$  measurements.

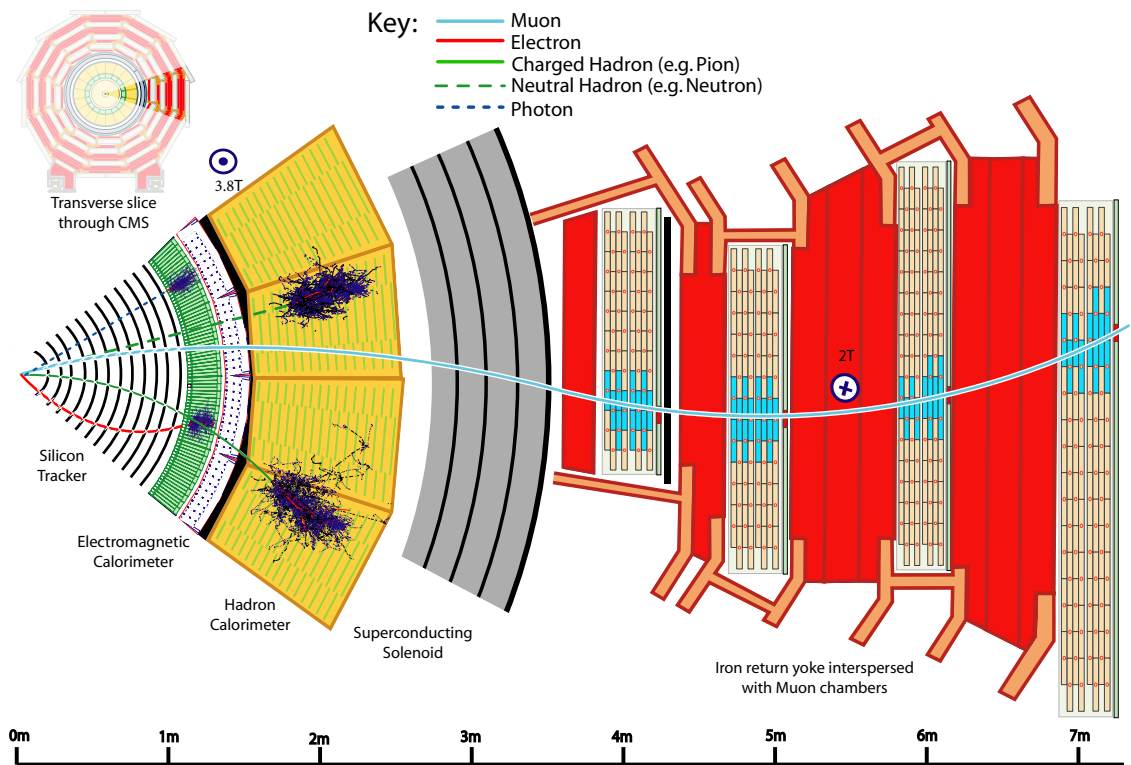


Figure 2.14: A sketch of a transverse slice of the CMS detector showing representative particle interactions used to identify and reconstruct particles with the CMS Particle Flow algorithm [13].

## Chapter 3: Search for displaced leptons

652 In this chapter, I present a search for new long-lived particles that could be pro-  
653 duced in proton-proton collisions at a center-of-mass energy of 13 TeV at the LHC  
654 and detected by the CMS experiment. The search targets the unique signature of  
655 “displaced leptons” that could be produced when long-lived particles decay to lep-  
656 tons after propagating a measurable distance from the nominal interaction point. The  
657 candidate signal events include at least two leptons (one electron and one muon, two  
658 electrons, or two muons) whose transverse impact parameters are between 0.01 and  
659 10 cm. Choosing transverse impact parameter as the main discriminating variable  
660 allows us to target pairs of displaced leptons without requiring that they form a com-  
661 mon vertex. We apply an otherwise minimal event selection to retain sensitivity to a  
662 wide range of new physics models.

663 The Ohio State CMS group has previously performed two related searches for  
664 displaced leptons in the electron-muon final state: one in  $19.7 \text{ fb}^{-1}$  of 8 TeV data and  
665 another in  $2.6 \text{ fb}^{-1}$  of 13 TeV data [48, 49]. The search presented here is the most  
666 sensitive to date. Some of the most significant improvements include:

- 667 • adding sensitivity to the electron-electron and muon-muon final states  
668 • simplifying the event selection to reduce model dependence

- 669       • introducing a custom lepton isolation definition to significantly reduce the back-  
670              ground from heavy-flavor meson decays
- 671       • implementing a new, fully data-driven background estimation procedure
- 672       • expanding the signal region to include leptons with smaller transverse impact  
673              parameters
- 674       • adding a second signal interpretation
- 675       • analyzing more than a factor of 40 times more data than the previous 13 TeV  
676              analysis [49]

677       The remainder of this chapter is organized as follows: Section 3.1 introduces the  
678       displaced leptons experimental signature in the context of LLPs at the LHC and  
679       gives an overview of the analysis strategy, Section 3.2 defines the data and simulated  
680       SM and signal samples used in the analysis, Section 3.3 describes the event selection  
681       criteria and defines the signal and control regions, Section 3.4 describes the various  
682       corrections applied to the SM and signal simulation, Section 3.5 investigates the  
683       sources of background and defines the procedure for estimating their contribution to  
684       the signal region, Section 3.6 describes the sources of systematic uncertainty in the  
685       efficiency for simulated signal events to pass the signal region selection, and Section 3.7  
686       presents the results.

## 687       **3.1 Overview**

### 688       **3.1.1 Long-lived particles at the LHC**

689       As discussed in Section 1.2.2, LLPs are common in the SM and naturally arise in  
690       many BSM scenarios. When produced in proton-proton collisions at the LHC, new

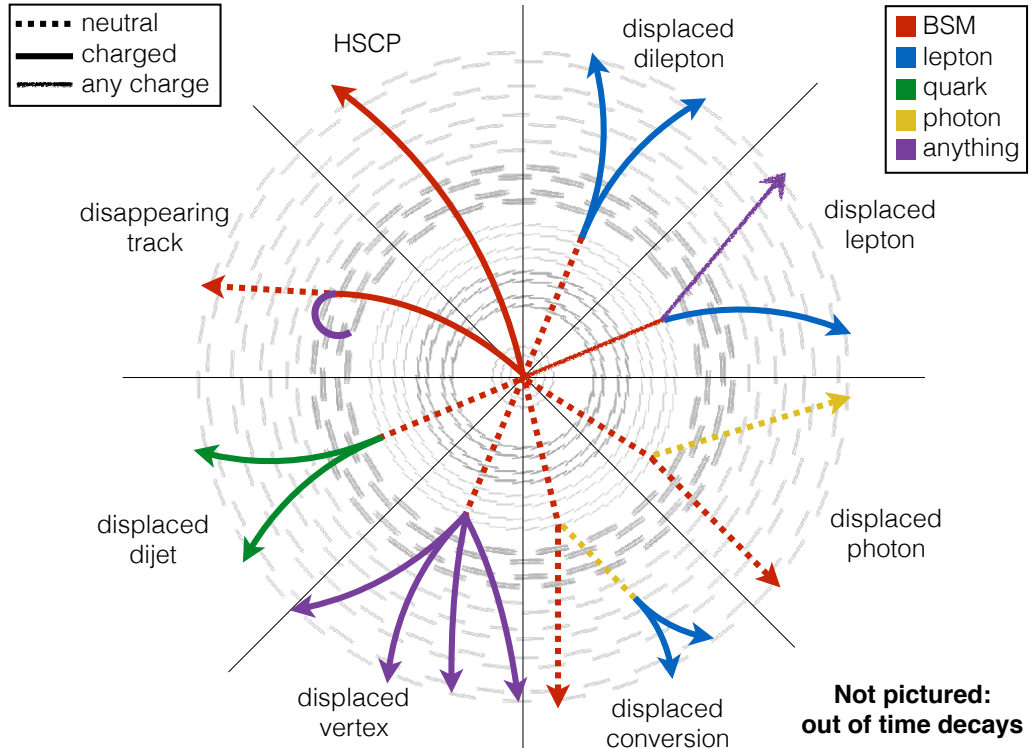


Figure 3.1: Illustration of several possible experimental signatures of long-lived particles [14].

LLPs have the potential to produce striking experimental signatures that differentiate them from SM backgrounds. As diagrammed in Fig. 3.1, new long-lived particles that decay within the detector volume can produce displaced vertices, physics objects whose trajectories do not point back to the nominal interaction point, or particle tracks that vanish before reaching the outer edge of the tracker. Neutral LLPs that decay farther out can pass undetected through the tracker before producing signals in the calorimeters or muon system, and heavy, charged LLPs that are stable on detector length scales can be identified by their unusually large charge depositions.

699        The identification of any of these LLP signatures above the expected background  
700        rates would be a clear sign of new physics, but their atypical nature adds an inherent  
701        layer of difficulty to studying such signatures. In fact, standard reconstruction al-  
702        gorithms and event selections frequently discard such unusual signatures and render  
703        the majority of LHC analyses insensitive to many BSM scenarios that include LLPs  
704        [50]. As a solution to the naturalness problem may require new physics at the LHC  
705        energy scale, it is critical that physicists face the challenges posed by LLP analyses  
706        and look everywhere BSM physics may be hiding.

707        Interest in LLPs is growing as evidence of BSM physics continues to evade LHC  
708        physicists. Recent CMS searches in 13 TeV proton-proton collisions target disappear-  
709        ing tracks [51] or use the ECAL timing capabilities to target photons or jets whose  
710        production at a displaced vertex delays the time of their detection [52, 53]. All ob-  
711        servations thus far agree with SM predictions, but these and other LLP analyses are  
712        probing regions of BSM parameter space that are untested by conventional analyses.

### 713        **3.1.2 Displaced leptons signature**

714        The Displaced Leptons analysis targets electrons and muons produced in the de-  
715        cays of new, long-lived particles. Inspired by models such as Displaced SUSY (see  
716        Section 1.2.3), we take care to maintain sensitivity to leptons that are produced in  
717        separate long-lived decays as well as those that share a common displaced vertex.  
718        This goal is achieved by selecting pairs leptons with large transverse impact param-  
719        eters and setting no constraints on the presence or absence of displaced vertices.  
720        Figure 3.2 shows the benefit of such an approach: the pair-produced new long-lived  
721        particles, labeled  $X$ , each decay to a single lepton and an unspecified second particle.

## CMS Simulation

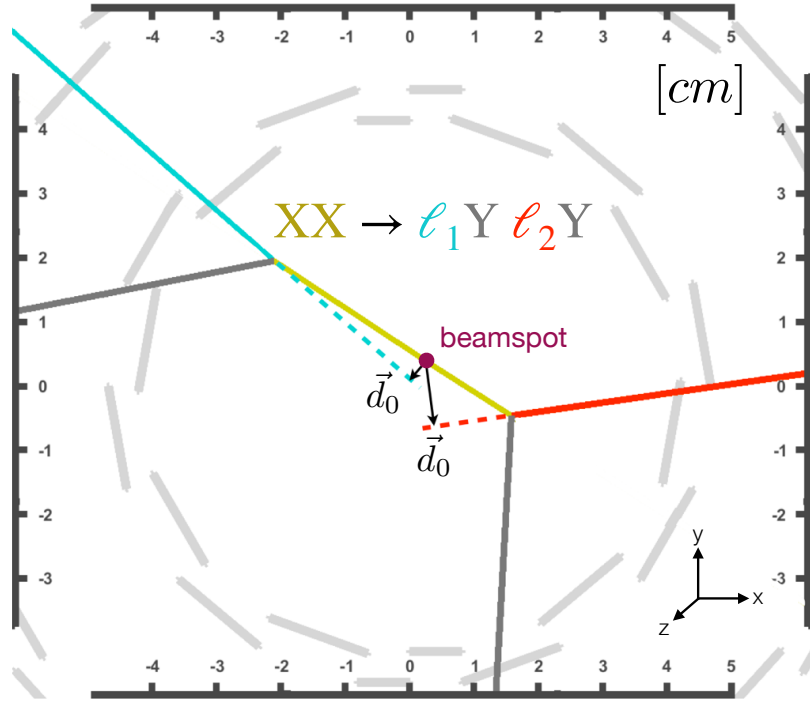


Figure 3.2: Illustration of the displaced leptons signature showing the definition of  $d_0$  in a transverse view of the CMS interaction point.  $X$  denotes a new long-lived particle,  $\ell$  denotes an electron or muon, and  $Y$  denotes any other decay products of the new long-lived particle. When interpreting the results of the Displaced Leptons analysis with the Displaced SUSY model,  $X$  refers to a top squark and  $Y$  refers to a b or d quark.

722 The lepton transverse impact parameter, which is labeled  $d_0$  in the figure and defined  
 723 explicitly below, is then used to identify the displaced nature of the lepton decays  
 724 without explicitly constraining the other decay products in any way. Note also that  
 725 the same strategy would successfully identify two leptons from a single long-lived  
 726 particle decay.

727 Lepton transverse impact parameter,  $d_0$ , is defined as the distance of closest ap-  
 728 proach in the transverse plane of the helical trajectory of the lepton track to the CMS

729 beamspot, which is the center of the region in which the proton bunches cross. The  
 730 transverse impact parameter is commonly measured with respect to the primary ver-  
 731 tex, but in the case of leptons produced in displaced decays, the association between  
 732 a given primary vertex and the resulting leptons is unreliable. We determine  $d_0$  from  
 733 measured properties of the lepton track using the following equation:

$$d_0 = \frac{(v_x - x_0)p_y - (v_y - y_0)p_x}{p_T} \quad (3.1)$$

734 where  $v_x$  and  $v_y$  refer to the  $x$  and  $y$  coordinates of the lepton track reference point,  
 735 which is usually chosen to be the point of closest approach to the center of CMS,  $x_0$   
 736 and  $y_0$  refer to the  $x$  and  $y$  coordinates of the beamspot, and  $p_x$ ,  $p_y$ , and  $p_T$  refer to the  
 737 magnitudes of the  $x$ ,  $y$ , and transverse components of the lepton's momentum.  $|d_0|$   
 738 is commonly used throughout the Displaced Leptons analysis because we generally  
 739 care about the magnitude of  $d_0$  but not its direction.

740 If we are to use lepton  $|d_0|$  as the discriminating variable in an LLP search, we  
 741 must ensure it scales appropriately with the parent LLP lifetime. Typically, a particle  
 742 with lifetime  $\tau$  will travel a distance  $d = \beta\gamma c\tau$ , where  $\beta$  and  $\gamma$  are relativistic factors  
 743 and  $c$  is the speed of light, so  $d$  and  $\tau$  are directly correlated. Figure 3.2 shows that  
 744 lepton  $|d_0|$  is determined by the distance travelled by the new LLP in the transverse  
 745 plane and the angle between the transverse momenta of the new LLP and the lepton.  
 746 Unless this angle is pathologically constrained to zero,  $|d_0|$  and  $\tau$  will be directly  
 747 correlated as well. In fact, the maximum value of lepton  $|d_0|$ , which occurs when  
 748 the angle between the transverse momenta of the new LLP and the lepton is  $\frac{\pi}{2}$ , is  
 749 exactly equal to the transverse distance between the beamspot and location of the  
 750 LLP decay.

751     Figure 3.3 shows the distribution of data and simulated Displaced SUSY events  
752     in the plane defined by electron and muon  $|d_0|$ . As expected, the data events, which  
753     are dominated by leptons from promptly decaying parent particles, are concentrated  
754     at low  $|d_0|$  values while the Displaced SUSY events are spread across the entire plane.  
755     This figure shows the power of  $|d_0|$  as a discriminating variable: requiring two leptons  
756     with  $|d_0| > 100 \mu\text{m}$  eliminates nearly all the SM background without requiring that  
757     the leptons form a common vertex.

758     Another possible discriminating variable could be  $|d_0|/\sigma_{|d_0|}$ , where  $\sigma_{|d_0|}$  is the  
759     uncertainty in  $|d_0|$ . Such a discriminating variable could potentially reduce the back-  
760     ground from leptons with poorly measured  $|d_0|$ , but we choose to use  $|d_0|$  because of  
761     its straightforward correspondence to the parent particle lifetime. We also find that  
762      $\sigma_{|d_0|}$  is often underestimated, which reduces the potential benefit of using  $|d_0|/\sigma_{|d_0|}$ .

### 763     3.1.3 Analysis strategy

764     Having seen that  $|d_0|$  can be used to identify leptons from long-lived particle decays  
765     without requiring that the leptons form a common vertex, we now define a strategy  
766     to target such a signature. The basic analysis strategy is outlined here and described  
767     in detail in the following sections.

768     In addition to maximizing our sensitivity to models such as Displaced SUSY,  
769     we also strive to develop an analysis that is model independent, signature based,  
770     and easy to reinterpret. With these goals in mind, we perform a relatively simple  
771     cut-and-count analysis in which our main event selection sets no constraints on any  
772     non-lepton physics object. Unlike previous displaced leptons analyses [48, 49], we  
773     allow final states with more than two leptons and set no constraints on the lepton

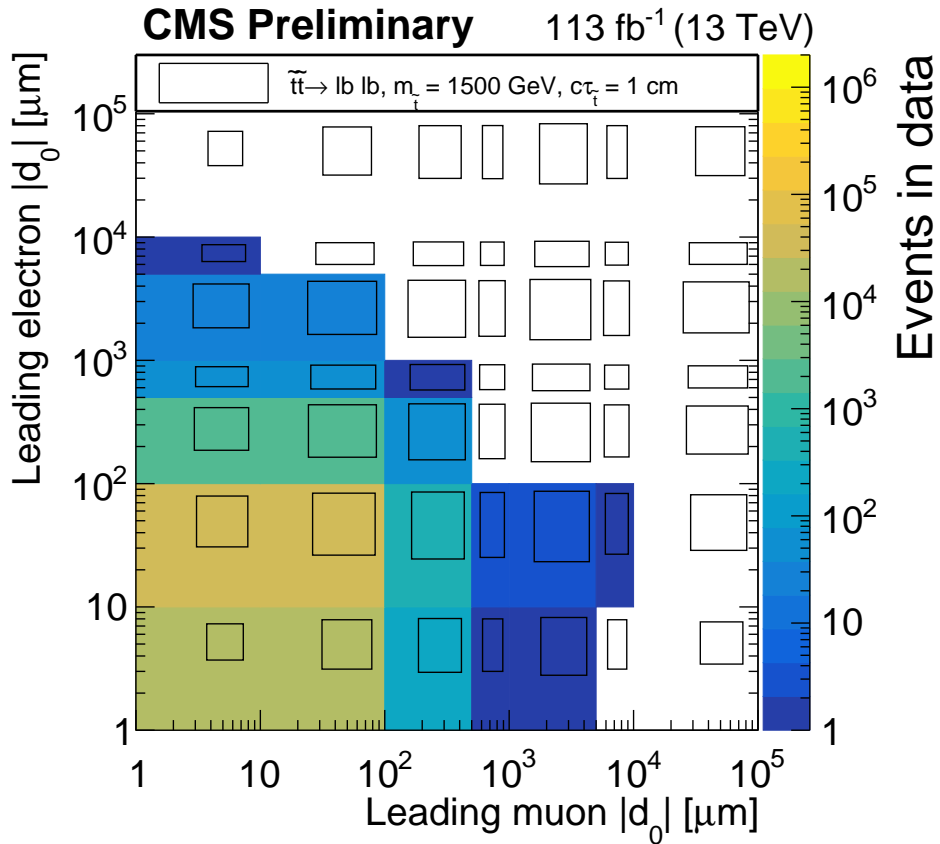


Figure 3.3: Distribution of data (colors) and simulated Displaced SUSY events (black boxes) in the plane defined by electron  $|d_0|$  and muon  $|d_0|$ . The size of the black boxes are proportional to the bin content, and the bins along the x and y axes include underflow. All events are required to pass the  $e\mu$  preselection defined in Section 3.3.

774 charge. As explained in Section 3.3, we select events in three analysis channels:  
775 electron-electron ( $ee$ ), electron-muon ( $e\mu$ ), and muon-muon ( $\mu\mu$ ). We then divide  
776 the events into different regions of the plane defined by the  $|d_0|$  of the two leptons  
777 that define the analysis channel. Figure 3.3, for example, shows this plane in the  
778  $e\mu$  channel. The signal region is defined as the region in which both leptons have  
779  $|d_0| > 100 \mu\text{m}$ .

780 Following the procedure defined in Section 3.5, we use the data in the non-signal  
781 regions to estimate the SM background in the signal region. Finally, we compare  
782 the background estimates and data yields in the signal region. In the absence of a  
783 significant excess, we use simulated signal events to constrain the available parameter  
784 space of the Displaced SUSY model. To avoid biasing the result, we blind ourselves  
785 to the data in the signal region and wait to observe the signal-region data until after  
786 we define and test the entire analysis procedure and receive pre-approval from the  
787 CMS Exotica Physics Analysis Group.

788    **3.2 Data and simulated samples**

789    **3.2.1 Experimental data**

790       This analysis uses proton-proton collision data taken in 2016, 2017, and 2018 at  
791       a center-of-mass energy of 13 TeV. In 2016, we use only the last two run periods due  
792       to lower displaced tracking efficiency caused by an analog pipeline voltage saturation  
793       problem in the silicon strip detector during the earlier run periods (see appendix A).  
794       In 2017, we use all run periods in the  $ee$  channel and all but the earliest run period  
795       in the  $e\mu$  and  $\mu\mu$  channels because the  $e\mu$  and  $\mu\mu$  triggers are not available in the  
796       earliest run period. In 2018, we use all available run periods in all three channels.  
797       Ultimately, this analysis uses an integrated luminosity of  $16.1 \pm 0.4 \text{ fb}^{-1}$  from 2016 in  
798       all three channels,  $41.5 \pm 1.0 \text{ fb}^{-1}$  ( $36.7 \pm 0.8 \text{ fb}^{-1}$ ) from 2017 in the  $ee$  channel ( $e\mu$   
799       and  $\mu\mu$  channels), and  $59.7 \pm 1.5 \text{ fb}^{-1}$  from 2018 in all three channels.

800       The search is performed in the MuonEG, DoubleEG (in 2016–2017), EGamma (in  
801       2018), and DoubleMu primary datasets. We also use the MET dataset to study the trig-  
802       ger efficiency and the Cosmics and NoBPTX datasets to study the displaced tracking ef-  
803       ficiency. All data are reconstructed in the 07Aug17, 31Mar2018, 17Sep2018 reprocess-  
804       ing campaigns with software versions CMSSW\_8\_0\_31, CMSSW\_9\_4\_8, and CMSSW\_10\_2\_0,  
805       respectively. The sole exception is the EGamma 2018D dataset, which was reconstructed  
806       in the 22Jan2019 campaign. In all cases, we use the CMS MiniAOD event format.

807    **3.2.2 Simulated background events**

808       This analysis employs a fully data-driven background estimation technique that  
809       does not rely on simulated SM events. We do, however, use simulated SM events  
810       to study possible sources of background and verify the validity of the background

estimation technique. The samples corresponding to 2016, 2017, and 2018 data conditions are from the `PdmVMCcampaignRunIISummer16`, `PdmVMCcampaignRunIIFall17`, and `PdmVMCcampaignRunIIAutumn18` production campaigns and were reconstructed in `CMSSW_8_0_31`, `CMSSW_9_4_8`, `CMSSW_10_2_0` with the MiniAODSIM event format. The samples simulating  $Z + \text{jets}$ ,  $W + \text{jets}$ , and  $t\bar{t}$  production are generated using `MADGRAPH5_aMC@NLO` [54, 55, 56], while the samples simulating diboson ( $WW$ ,  $WZ$ , and  $ZZ$  with leptonic and semi-leptonic decays) and single-top-quark production are simulated with `POWHEG v2` [57, 58, 59, 60, 61]. `PYTHIA 8.2` [62] is used to simulate the parton showering and hadronization for all processes. The modeling of the underlying event is generated using the `CUETP8M1` [63] and `CP5` tunes [64] for simulated samples corresponding to the 2016 and 2017–18 data sets, respectively.

### 3.2.3 Simulated signal events

We use simulated signal events to guide the analysis strategy and interpret our results. Samples of simulated  $\text{pp} \rightarrow \tilde{t}\bar{t}$  events in which the top squarks decay to a lepton and a  $b$  quark or  $d$  quark, are produced at leading order using `PYTHIA 8.2` [62]. For simplicity, all lepton flavors are generated with equal branching fractions. The top squarks can form strongly-produced hadronic states called R-hadrons, which are generated with `PYTHIA`. The interactions of the R-hadrons with matter are not simulated in `GEANT4`, but they are expected to have a negligible impact on the analysis because the lepton identification requirements effectively require the R-hadron to decay in the middle of the tracker volume. Each R-hadron therefore traverses  $\lesssim 1$  interaction length, making it unlikely to produce a high quality track, come to a stop in the detector, or flip its charge. To generate the samples, we start with a SUSY Les

834 Houches Accord file [65] corresponding to Snowmass Points and Slopes point 1a [66]  
835 and modify the mass and width of the top squark according to the sample being  
836 produced. We generate samples with  $\tilde{t}$  masses from 100 to 1800 GeV at 100 GeV  
837 intervals and with  $\tilde{t}$  lifetimes at each decade from 0.1 mm to 1 m. After producing  
838 these samples, we also employ a lifetime reweighting technique to effectively produce  
839 eight additional lifetime points between each pair of adjacent lifetimes. In the case of  
840 the 1 m samples, we also use an equivalent technique to effectively produce nine ad-  
841 ditional lifetime points between 1 and 10 m. The production cross sections for each  $\tilde{t}$   
842 mass hypothesis are taken from the website of the LHC SUSY Cross Section Working  
843 Group. The signal samples are reconstructed in the same campaigns and with the  
844 same conditions as the SM background samples described in 3.2.2.

845    **3.3 Event selection**

846    **3.3.1 Triggers**

847       The events are required to pass different triggers in each channel. Standard CMS  
848       electron and muon triggers are not designed for displaced objects, so we use non-  
849       standard triggers for both electrons and muons. For muons, we remove all trigger  
850       requirements relating to the muon  $|d_0|$  or longitudinal impact parameter or the ver-  
851       tex from which the muon originates. For electrons, we actually use photon triggers,  
852       which collect events with electrons as well as photons but do not rely on any tracking  
853       information. See Section 2.2.6 for a brief overview of the CMS trigger system.

854       In the  $e\mu$  channel, 2016 data and corresponding simulated events are required to  
855       pass the logical OR of two HLT paths (`HLT_Mu38NoFiltersNoVtx_Photon38_Cal`  
856       `oIdL_v*` OR `HLT_Mu28NoFiltersNoVtxDisplaced_Photon28_CaloIdL_v*`) that  
857       were both designed for this analysis. The first trigger requires at least one muon  
858       with  $p_T > 38 \text{ GeV}$  and places no constraints on the vertex,  $d_0$ , or longitudinal impact  
859       parameter. The second trigger requires at least one muon with  $p_T > 28 \text{ GeV}$  and  
860        $|d_0| > 0.01 \text{ cm}$ . Each of these two triggers also requires at least one photon that  
861       passes a loose calorimeter-based identification. The first (second) trigger requires  
862       that the photon  $E_T$  is greater than 38 GeV (28 GeV). The signal efficiency with these  
863       dedicated triggers is significantly higher than that of standard muon-photon HLT  
864       paths.

865       In 2017 and 2018, data and corresponding simulated events in the  $e\mu$  channel are  
866       required to pass `HLT_Mu43NoFiltersNoVtx_Photon43_CaloIdL_v*`. The muon  $p_T$   
867       and photon  $E_T$  thresholds are raised with respect to 2016 due to increased pileup. A

868 version of the 2016 trigger that requires displaced muons is not available in 2017 and  
869 2018.

870 In the  $ee$  channel, 2016 data and corresponding simulated events are required to  
871 pass the logical OR of two HLT paths (`HLT_Diphoton30_18_R9Id_OR_IsoCaloId_A`  
872 `ND_HE_R9Id_Mass90_v*` OR `HLT_DoublePhoton60_v*`). The first requires a leading  
873 photon with  $E_T > 30 \text{ GeV}$  and a subleading photon with  $E_T > 18 \text{ GeV}$ . Calorimeter  
874 identification, isolation,  $H/E$ , and  $R_9$  requirements are made on both photons, and  
875 the di-photon invariant mass must be  $> 90 \text{ GeV}$ . This path is highly efficient at low  
876  $\tilde{t}$  mass. The second trigger simply requires at least two photons with  $E_T > 60 \text{ GeV}$ .  
877 This path is highly efficient at large  $\tilde{t}$  mass and lifetime.

878 In 2017 and 2018, data and corresponding simulated events in the  $ee$  channel are  
879 required to pass `HLT_Diphoton30_22_R9Id_OR_IsoCaloId_AND_HE_R9Id_Mass90_v*`  
880 OR `HLT_DoublePhoton70_v*`. The photon  $E_T$  thresholds are raised with respect to  
881 2016 due to increased pileup.

882 In the  $\mu\mu$  channel, 2016 data and corresponding simulated events are required to  
883 pass the logical OR of two HLT paths (`HLT_DoubleMu33NoFiltersNoVtx_v*` OR  
884 `HLT_DoubleMu23NoFiltersNoVtxDisplaced_v*`) that were both designed for this  
885 analysis. The first trigger requires at least two muons with  $p_T > 33 \text{ GeV}$  and sets  
886 no constraints on the vertex,  $|d_0|$ , or the longitudinal impact parameter. The second  
887 trigger requires at least two muons with  $p_T > 23 \text{ GeV}$  and  $|d_0| > 0.01 \text{ cm}$ . The signal  
888 efficiency with these dedicated triggers is significantly higher than that of standard  
889 di-muon HLT paths.

890 In 2017 and 2018, data and corresponding simulated events in the  $\mu\mu$  channel are  
891 required to pass `HLT_DoubleMu43NoFiltersNoVtx_v*`. The muon  $p_T$  threshold is

892 raised with respect to 2016 due to increased pileup. A version of the 2016 trigger that  
893 requires displaced muons is not available in 2017 and 2018.

894 **3.3.2 Preselection**

895 Starting from the events collected with the triggers described above, we next apply  
896 a set of preselection criteria to select the events to be analyzed. The preselection  
897 criteria vary by channel and year, but the fundamental goal is always to select events  
898 with at least one good reconstructed lepton of each flavor required by the channel.

899 Specifically, the  $e\mu$  preselection selects events with at least one PF electron and  
900 at least one global PF muon, the  $ee$  preselection selects events with at least two PF  
901 electrons, and the  $\mu\mu$  preselection selects events with at least two global PF muons  
902 (see Section 2.2.7 for a discussion of the PF algorithm). We set requirements on these  
903 electrons and muons as shown in Tables 3.1, 3.2, and 3.3. The electron and muon  
904  $p_T$  requirements are chosen such that the trigger efficiency is independent of lepton  
905  $p_T$ , while electron and muon  $|\eta|$  requirements are chosen to reduce the fraction of  
906 leptons with poorly measured  $d_0$  (see Appendix B). Electrons that traverse the gap  
907 between the endcap and barrel detectors are also rejected due to the known decrease  
908 in reconstruction performance in this region.

909 We use a tight cut-based identification (ID) on the electrons and muons to se-  
910 lect well-reconstructed leptons, but unlike the standard ID definitions used in many  
911 CMS analyses, we do not place any requirements on  $|d_0|$  or the longitudinal impact  
912 parameter. In all other respects, we follow the cut-based ID recommendations of the  
913 CMS EGamma and Muon Physics Object Groups. The electron ID corresponds to  
914 `egmGsfElectronIDs:cutBasedElectronID-Summer16-80X-V1-tight` in 2016,

Table 3.1: The  $e\mu$  preselection criteria. The electron and muon  $p_T$  thresholds increase in 2017 in accordance with the increased HLT electron and muon  $p_T$  thresholds.

Selection variable	Object-level selections		
	Electron	Muon	Muon
Number	$\geq 1$	$\geq 1$	$\geq 1$
$p_T$	$> 42 \text{ GeV}$ (2016) $> 45 \text{ GeV}$ (2017 and 2018)	$> 40 \text{ GeV}$ (2016) $> 45 \text{ GeV}$ (2017 and 2018)	
$ \eta $	$< 1.5$	$< 1.5$	
	not in ECAL gap	-	
$\eta - \phi$	veto ( $1.0 < \eta < 1.5$ and $\phi > 2.7$ ) (2017) veto ( $0.3 < \eta < 1.2$ and $0.4 < \phi < 0.8$ ) (2018)	veto ( $1.0 < \eta < 1.5$ and $\phi > 2.7$ ) (2017) veto ( $0.3 < \eta < 1.2$ and $0.4 < \phi < 0.8$ ) (2018)	
ID	Tight (cut-based)	Tight (cut-based)	Tight (cut-based)
Custom isolation	Tight	Tight	Tight
	Event-level selections		
	Zero $\mu\mu$ pairs with $\cos \alpha < -0.99$ Reject $\Delta t < -20$ , if both timing ndof $> 7$ At least one $e\mu$ pair with $\Delta R(e, \mu) > 0.2$ Reject events with candidate leptons form a displaced vertex in the tracker material		

Table 3.2: The  $ee$  preselection criteria. The electron  $p_T$  threshold increase in 2017 and 2018 in accordance with the increased HLT electron  $p_T$  threshold.

Selection variable	Object-level selections	
Number	Electron	
$p_T$	$\geq 2$ $> 65 \text{ GeV}$ (2016) $> 75 \text{ GeV}$ (2017 and 2018)	
$ \eta $	$< 1.5$ not in ECAL gap	
$\eta - \phi$ (pixel power supply issue)	veto ( $1.0 < \eta < 1.5$ and $\phi > 2.7$ ) (2017) veto ( $0.3 < \eta < 1.2$ and $0.4 < \phi < 0.8$ ) (2018)	
ID	Tight (cut-based)	
Custom isolation	Tight	
	Event-level selections	
	At least one $ee$ pair with $\Delta R(e, e) > 0.2$	
	Reject events with candidate leptons form a displaced vertex in the tracker material	
	Reject events with displaced muons in the $e\mu$ channel inclusive signal region	

Table 3.3: The  $\mu\mu$  preselection criteria. The muon  $p_T$  threshold increase in 2017 and 2018 in accordance with the increased HLT muon  $p_T$  threshold.

Selection variable	Object-level selections	
	Muon	$\geq 2$
$p_T$		$> 35 \text{ GeV (2016)}$ $> 45 \text{ GeV (2017 and 2018)}$
$ \eta $		$< 1.5$
		veto ( $1.0 < \eta < 1.5$ and $\phi > 2.7$ ) (2017) veto ( $0.3 < \eta < 1.2$ and $0.4 < \phi < 0.8$ ) (2018)
ID	Tight (cut-based)	
Custom isolation		Tight
Event-level selections		
		Zero $\mu\mu$ pairs with $\cos \alpha < -0.99$
		Reject $\Delta t < -20$ , if both timing ndof $> 7$
		At least one $\mu\mu$ pair with $\Delta R(\mu, \mu) > 0.2$
		Reject events with candidate leptons from a displaced vertex in the tracker material
		Reject events with displaced electrons in the $e\mu$ channel inclusive signal region

Table 3.4: The electron tight ID requirements, which are identical to the tight cut-based ID from the CMS EGamma Physics Object Group with the  $d_0$  and longitudinal impact parameter requirements removed.

Electron ID requirements	
full5x5 $\sigma I\eta I\eta <$	0.0104 (2018, 2017) 0.00998 (2016)
$ \delta\eta_{\text{Seed}}  <$	0.00255 (2018) 0.00353 (2017) 0.00308 (2016)
$ \delta\phi_{\text{In}}  <$	0.022 (2018) 0.0499 (2017) 0.0816 (2016)
H/E <	0.026 + 1.15/E + 0.0324 $\rho$ /E (2018) 0.026 + 1.12/E + 0.0368 $\rho$ /E (2017) 0.0414 (2016)
Rel. comb. PF iso with EA corr <	0.0287 + 0.506/ $p_T$ (2018) 0.0361 (2017) 0.0588 (2016)
$ 1/E - 1/p  <$	0.159 (2018) 0.0278 (2017) 0.0129 (2016)
expected missing inner hits $\leq$	1
pass conversion veto	yes

915 `egmGsfElectronIDs:cutBasedElectronID-Fall17-94X-V1-tight` in 2017, and

916 `egmGsfElectronIDs:cutBasedElectronID-Fall17-94X-V2-tight` in 2018. The

917 electron and muon tight ID requirements are summarized in Tables 3.4 and 3.5.

918 We also require that electrons and muons are isolated. Specifically, we use a

919 modified isolation definition that accounts for the fact that displaced leptons may

920 be associated with the wrong primary vertex. The standard PF isolation assumes

921 all energy from primary vertices other than the leading primary vertex is due to

Table 3.5: The muon tight ID requirements, which are identical to the tight cut-based ID from the CMS Muon Physics Object Group with the requirements on  $d_0$  and the longitudinal impact parameter removed.

Muon ID requirements
Is a global muon
Is a PF muon
$\chi^2/n_{\text{dof}}$ of the global-muon track fit is $< 10$
At least one muon-chamber hit included in the global-muon track fit
Muon segments in at least two muon stations
At least 1 valid pixel hit
At least 6 tracker layers with hits

922 pileup, which is not true when the primary vertex ordering is altered by an incorrectly  
 923 associated lepton. We have therefore modified the pileup correction to be agnostic  
 924 to the primary vertex ordering by allowing PF candidates from any primary vertex  
 925 to contribute to the isolation sum and by using a simple  $\rho$ -based pileup correction,  
 926 where  $\rho$  is the total transverse energy of all the PF candidates divided by the total  
 927 detector area. Figure 3.4 shows how the size of the pileup correction term depends  
 928 on lepton displacement in the standard isolation but not in the modified isolation  
 929 described here. We use the modified isolation definition for both electrons and muons  
 930 while keeping the original tight working point for electrons and slightly tightening  
 931 the tight working point for muons. In the end, we require that the relative isolation  
 932 is  $< 0.10$  for muons and  $< 0.0588$  for electrons in 2016 and  $< 0.0287 + 0.506/p_T$   
 933 for electrons in 2017 and 2018. As shown in Figs. 3.5 and 3.6, this modified PF  
 934 isolation rejects substantially more background when the leptons are displaced but  
 935 does not significantly alter the signal yield. We note, however, that there may still be  
 936 some minor dependence on the primary vertex selection in the PF muon requirement

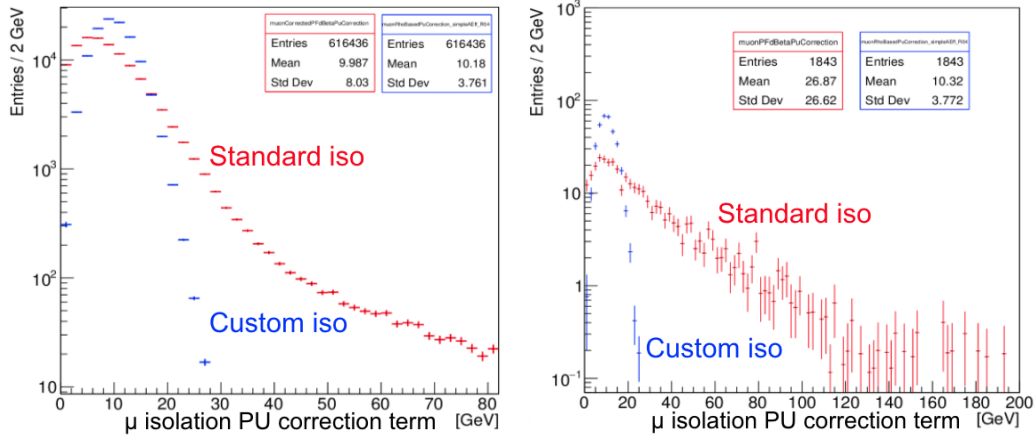


Figure 3.4: The muon isolation pileup correction term, for the standard muon isolation and the modified muon isolation in simulated  $t\bar{t}$  events that pass the  $e\mu$  preselection in 2018 conditions. The plot on the left is for muon  $|d_0| < 100 \mu\text{m}$ , and the plot on the right is for muon  $500 < |d_0| < 1000 \mu\text{m}$ .

937 because the PF muon selection includes some loose isolation requirements where the  
 938 charged hadron component is constrained to the selected primary vertex.

939 We also reject electrons and muons in certain regions of the  $\eta$ - $\phi$  plane where lepton  
 940  $|d_0|$  is more likely to be mismeasured. We identify these regions as highly populated  
 941 bins in the electron  $\eta$ - $\phi$  distribution in a prompt-muon, displaced-electron control  
 942 region in 2017 and 2018 data (see Fig.3.7). No such bins are present in 2016 data.  
 943 The identified regions coincide with regions found by a previous CMS analysis [51] to  
 944 be affected by power supply issues in the pixel detector. The  $\eta$ - $\phi$  variation is more  
 945 apparent for displaced electrons than displaced muons, so we use data in a prompt  
 946 muon ( $|d_0| < 40 \mu\text{m}$ ), displaced electron ( $100 < |d_0| < 500 \mu\text{m}$ ) control region to  
 947 define the regions used for both electrons and muons. In 2017, the rejected region is  
 948  $1.0 < \eta < 1.5$  AND  $\phi > 2.7$ , and in 2018 the rejected region is  $0.3 < \eta < 1.2$  AND  
 949  $0.4 < \phi < 0.8$ .

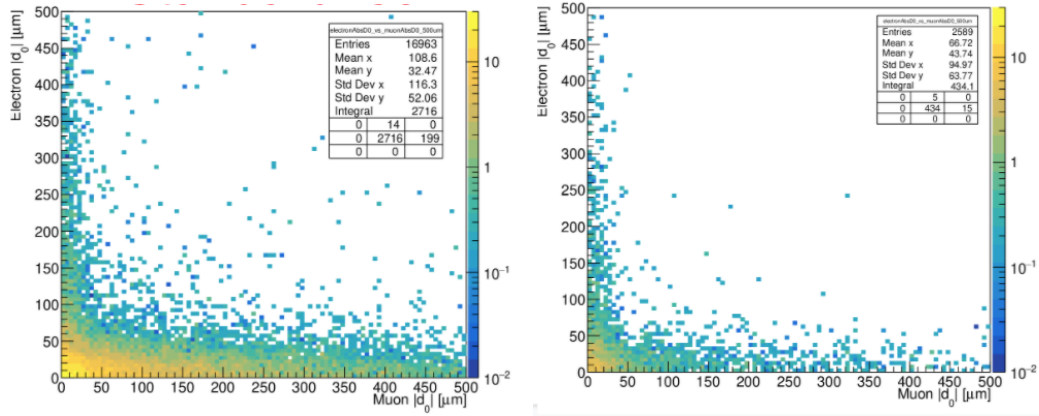


Figure 3.5: The electron  $|d_0|$  versus the muon  $|d_0|$ , for  $t\bar{t}$  simulated events that pass the  $e\mu$  preselection and where at least one lepton comes from a heavy-flavor meson. The plot on the left uses the standard isolation, and the plot on the right uses the modified isolation.

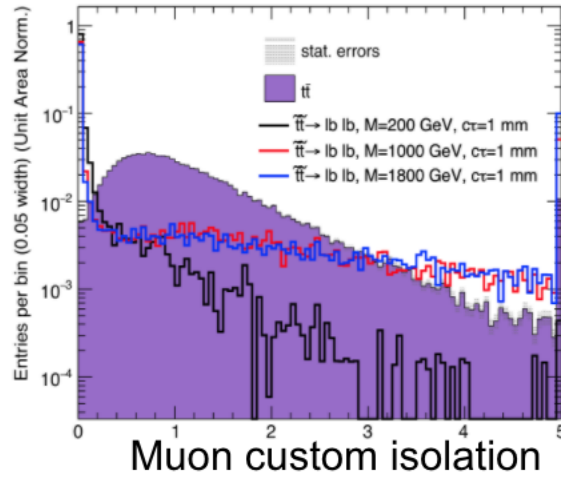


Figure 3.6: The muon custom isolation distribution for simulated  $t\bar{t}$  background and  $\tilde{t}\tilde{t} \rightarrow l\bar{b} l\bar{b}$  signal events in 2018 conditions.

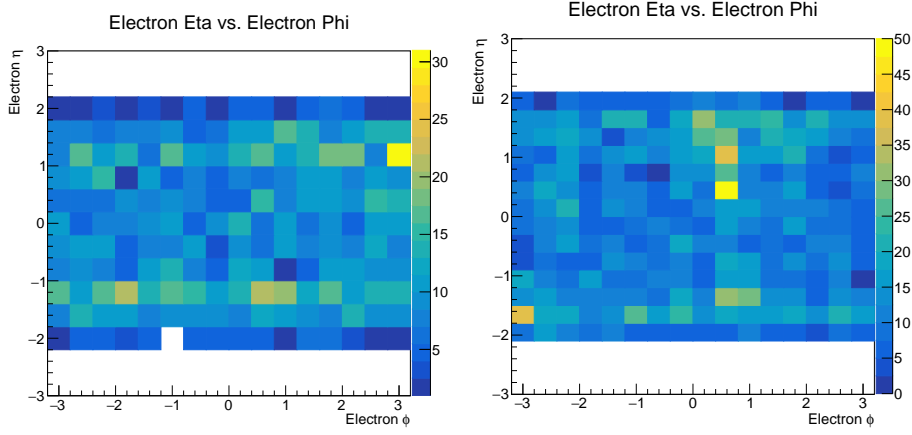


Figure 3.7: The electron  $\eta - \phi$  distribution in a prompt-muon, displaced-electron control region in 2017 (left) and 2018 (right) data before vetoing the regions affected by pixel power-supply issues.

950 In addition to these object-level selections, we also impose a few event-level selec-  
 951 tions designed to remove potential backgrounds from cosmic rays, material interac-  
 952 tions, and displaced decays of SM hadrons. To remove cosmic-ray muons in the  $\mu\mu$   
 953 and  $e\mu$  channels, we require there be zero pairs of muons with  $\cos \alpha < -0.99$ , where  
 954  $\alpha$  is the 3D angle between the muons, and that the relative time between the leading  
 955 two muons is inconsistent with the timing of cosmic-ray muons. To do this, we look  
 956 at the muon time measured by the DTs and CSCs, which assume that the muons are  
 957 traveling outwards from the center of the detector. We then use the muon  $\phi$  measure-  
 958 ments to determine which muon is above the other and find  $\Delta t$ , the time of the lower  
 959 muon subtracted from the time of the upper muon. We reject events with  $\Delta t < -20$   
 960 if the number of degrees of freedom of the timing measurements for both muons is  
 961 greater than seven. To remove leptons from decays of SM hadrons, we require that  
 962 the candidate leptons not be too close together in the  $\eta\phi$  plane. Specifically, we

963 find that requiring  $\Delta R > 0.2$  significantly reduces the contribution from SM hadrons  
964 without noticeably affecting the signal acceptance. To remove leptons from material  
965 interactions, we reject events in which the candidate leptons form a good displaced  
966 vertex that overlaps with the tracker material. The vertices are reconstructed with  
967 the Kalman Vertex Fitter, and a “good” vertex is one with  $\chi^2/n_{\text{dof}} < 20$ . The tracker  
968 material map is obtained from the tracker material budget measurements [67, 68].  
969 See Section 3.5.6 for tests in data that involve inverting the criteria described in this  
970 paragraph.

971 Finally, to ensure that the signal regions of all three channels are orthogonal to  
972 one another, we reject events in the  $ee$  ( $\mu\mu$ ) channel with at least one muon (electron)  
973 that passes the  $e\mu$  channel preselection and has  $|d_0| > 100 \mu\text{m}$ .

974 In contrast to previous displaced leptons analyses [48, 49], we allow for the possi-  
975 bility of more than one lepton of each type in a given channel and set no requirements  
976 on the charge product of the lepton pair. These changes were made at the request of  
977 several theorists, including the authors of Ref. [69].

978 Figure 3.8 shows the electron and muon  $|d_0|$  distributions in simulated signal and  
979 background events that pass the 2018  $e\mu$  preselection, and Fig. 3.9 shows the cumu-  
980 lative number of simulated signal events that pass each 2018 preselection criterion in  
981 all three channels for several top squark lifetime hypotheses.

### 982 3.3.3 Prompt control region

983 In order to verify the implementation of our selection and corrections to simula-  
984 tion (see Section 3.4), we define a prompt control region that is dominated by SM  
985 background events. Events in each channel’s prompt control region are selected by

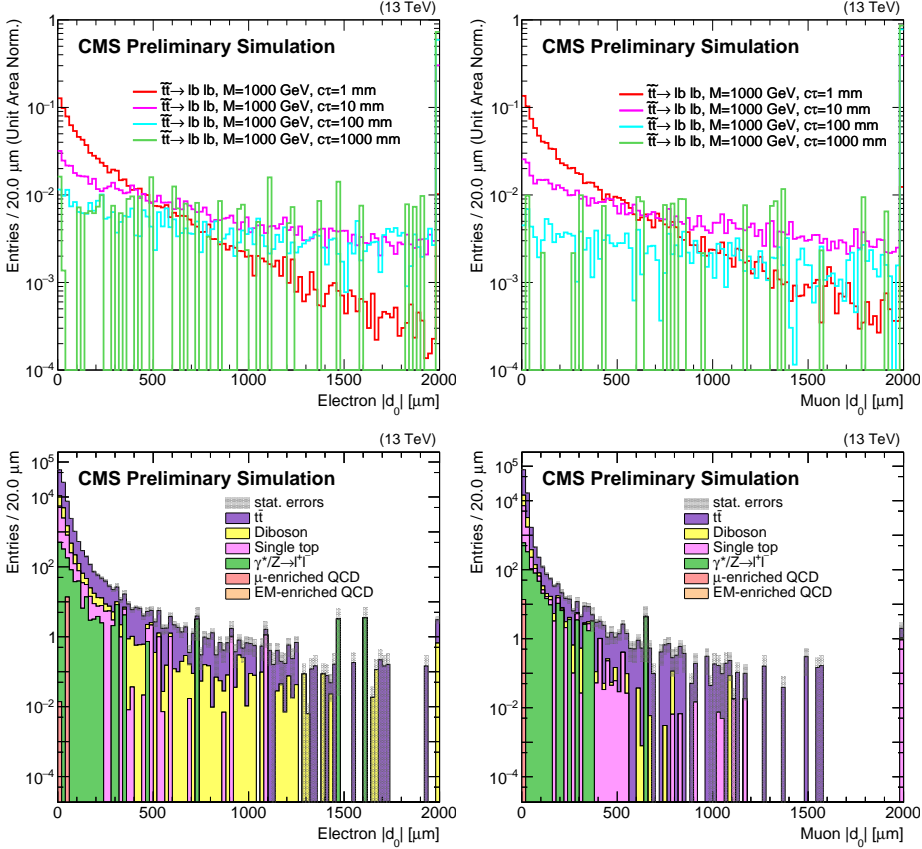


Figure 3.8: The electron (left) and muon (right)  $|d_0|$  distributions for 2018 simulation events that pass the  $e\mu$  preselection criteria. The upper two plots show  $\tilde{t}\tilde{t} \rightarrow \bar{l}b\bar{l}b$  simulation for a single  $\tilde{t}$  mass and four different proper decay lengths; each histogram is normalized to unity. The lower two plots show the background simulation normalized to the integrated luminosity. In all of the histograms, the last bin includes the overflow. All of the corrections from Section 3.4 are applied.

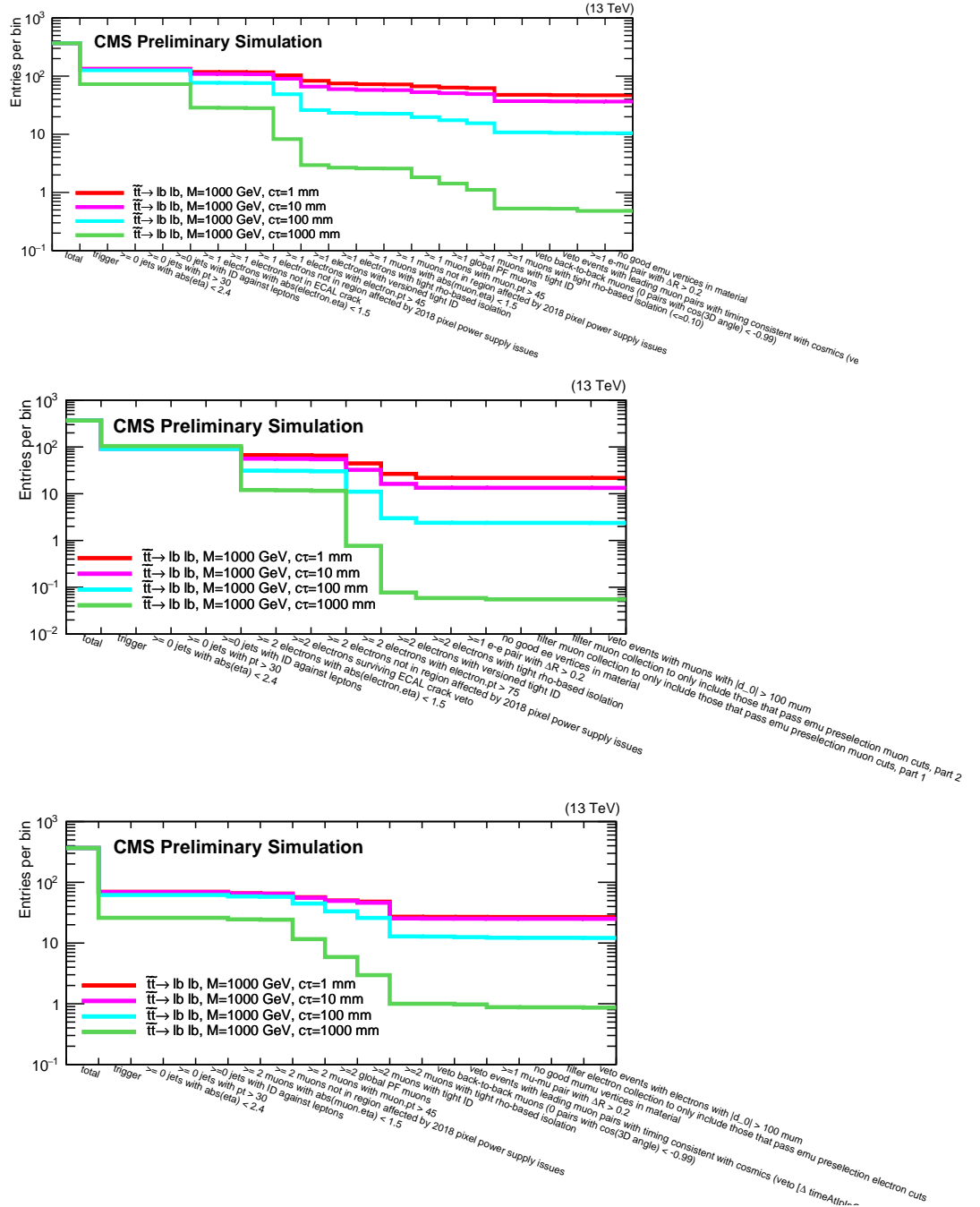


Figure 3.9: The cumulative number of events that pass each criterion in the  $e\mu$  (upper),  $ee$  (middle), and  $\mu\mu$  (lower) preselection, using 2018 signal simulation. Several  $\tilde{t}$  proper decay lengths are shown. The jet criteria do not exclude any events and are simply an artifact of the analysis framework.

requiring that they pass all of the criteria defined in Section 3.3.2 as well as the requirement that the candidate leptons have  $|d_0| < 50 \mu\text{m}$ . We define this region in each channel in order to check for reasonable agreement between simulated SM events and data after applying the corrections described in Section 3.4. Some examples are shown in Figs. 3.10, 3.11, and 3.12, which show the  $p_T$ ,  $\eta$ , and  $|d_0|$  distributions of the leptons in the  $e\mu$ ,  $ee$ , and  $\mu\mu$  prompt control regions, respectively, for 2016 data and background simulation. The data-driven background estimation technique employed in this analysis removes the need for exact agreement between data and simulation, but the absence of any significant discrepancies gives us confidence that we are accounting for the correct sources of prompt SM leptons and that our selection and corrections are functioning as intended.

### 3.3.4 Inclusive signal region

Finally, we define the region to which new physics may contribute significantly. The inclusive signal region is populated by events that pass all of the criteria defined in Section 3.3.2 as well as the requirement that the candidate leptons each have  $100 \mu\text{m} < |d_0| < 10 \text{ cm}$ . We do not select leptons with  $|d_0| > 10 \text{ cm}$  because the tracking efficiency drops sharply after this point, as shown in Section C. This requirement also ensures that the leptons originate within the pixel volume, which is effectively required by the pixel hit requirement of the tight lepton IDs. Table 3.6 lists the cumulative efficiency for  $\tilde{t}\tilde{t} \rightarrow \bar{l}b\bar{l}b$  events to pass the full 2018 inclusive signal region selection for several signal points. To ensure sensitivity to a wide range of new particle masses and lifetimes, we further subdivide the inclusive signal region into bins defined

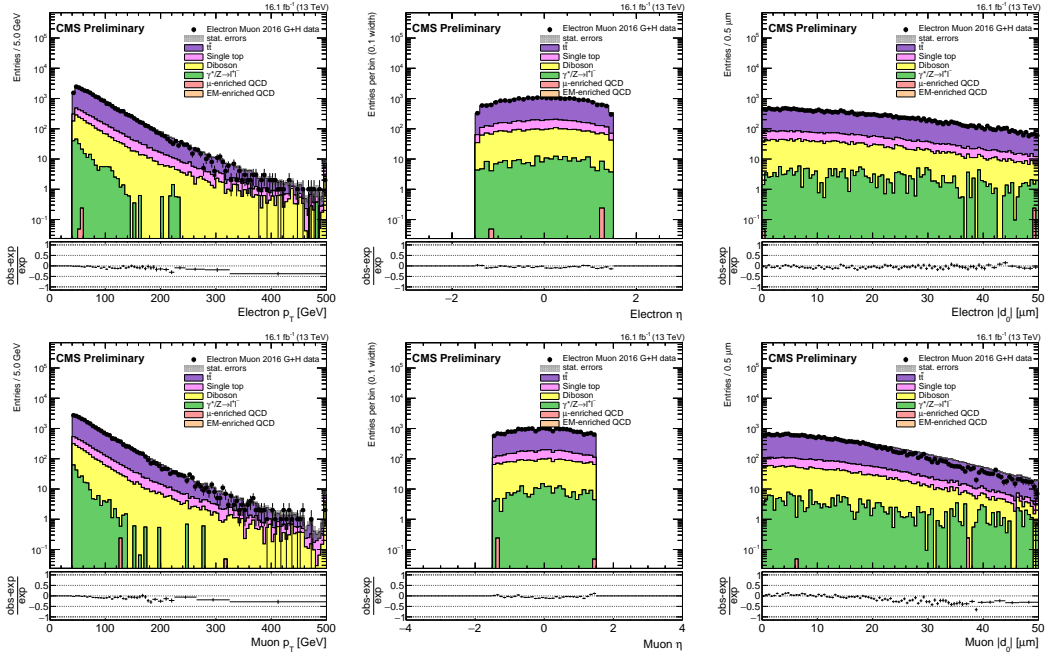


Figure 3.10: The electron (top) and muon (bottom)  $p_T$  (left),  $\eta$  (center), and  $|d_0|$  (right) distributions in the  $e\mu$  prompt control region for 2016 data and MC simulation. The rightmost bin in each plot contains the overflow entries.

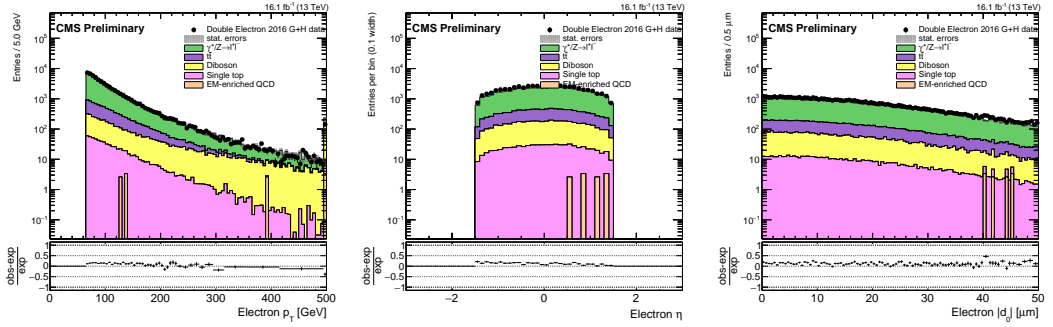


Figure 3.11: The electron  $p_T$  (left),  $\eta$  (center), and  $|d_0|$  (right) distributions in the  $ee$  prompt control region for 2016 data and MC simulation. The rightmost bin in each plot contains the overflow entries.

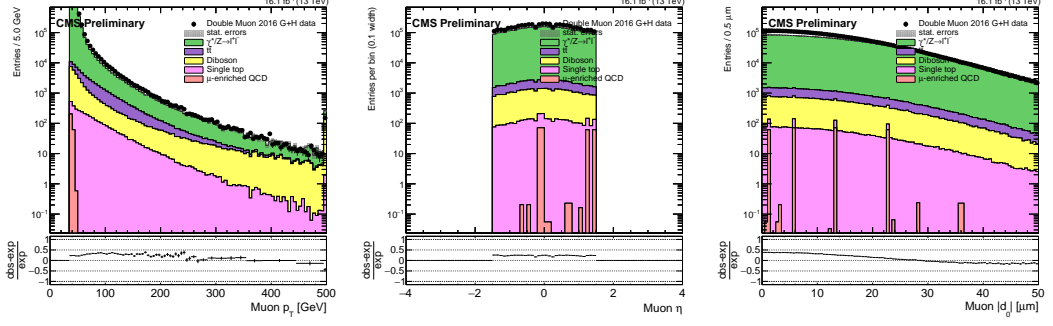


Figure 3.12: The muon  $p_T$  (left),  $\eta$  (center), and  $|d_0|$  (right) distributions in the  $\mu\mu$  prompt control region for 2016 data and MC simulation. The rightmost bin in each plot contains the overflow entries.

1008 by the  $|d_0|$  of each candidate lepton and the  $p_T$  of one candidate lepton. The exact  
 1009 binning is described in Section 3.5.2.

Table 3.6: The cumulative efficiency for simulated  $\tilde{t}\tilde{t} \rightarrow \bar{l}b\bar{l}\bar{b}$  signal events to pass the 2018 inclusive signal region selection, for several choices of  $\tilde{t}$  mass and  $c\tau$ . The corrections described in Section 3.4 are applied.

$e\mu$ inclusive signal region			
	200 GeV	1000 GeV	1800 GeV
0.1 cm	2.1%	4.6%	4.6%
1 cm	3.5%	7.9%	8.8%
10 cm	1.0%	2.7%	3.4%
100 cm	0.047%	0.13%	0.16%

$ee$ inclusive signal region			
	200 GeV	1000 GeV	1800 GeV
0.1 cm	0.47%	2.1%	2.1%
1 cm	0.60%	2.8%	3.3%
10 cm	0.11%	0.59%	0.76%
100 cm	0.003%	0.014%	0.022%

$\mu\mu$ inclusive signal region			
	200 GeV	1000 GeV	1800 GeV
0.1 cm	1.4%	2.6%	2.5%
1 cm	3.1%	5.6%	5.9%
10 cm	1.5%	3.2%	3.7%
100 cm	0.11%	0.23%	0.34%

1010 **3.4 Corrections to simulation**

1011 We apply several corrections to the simulated background and signal events in  
1012 order to account for known differences between simulation and data. Each correction  
1013 is described individually in the following sections.

1014 **3.4.1 Event pileup**

1015 The simulation is corrected so that its distribution of the number of pileup interac-  
1016 tions matches that of 2016, 2017, and 2018 data. Each simulated sample is reweighted,  
1017 event-by-event, by scale factors derived by dividing the pileup distribution in data by  
1018 the pileup distribution in the given simulated sample.

1019 **3.4.2 Lepton ID**

1020 We apply scale factors provided by the CMS Physics Object Groups to correct  
1021 for known differences in the lepton reconstruction and tight ID performance between  
1022 data and simulation. Although our lepton ID differs from the standard tight ID in  
1023 that we do not set requirements on  $|d_0|$  or the longitudinal impact parameter, the  
1024 standard scale factors are still sufficient because they are derived from leptons from  
1025  $Z$  boson decays that are representative of leptons in the bulk of the  $|d_0|$  distribution,  
1026 and we apply additional systematic uncertainties to account for possible differences  
1027 at larger  $|d_0|$  (see Section 3.6).

1028 **3.4.3 Lepton  $d_0$  resolution**

1029 As shown in Fig. 3.13, the agreement between data and simulation in the 2017 and  
1030 2018 electron and muon  $|d_0|$  distributions was initially poor. We found that the aver-  
1031 age muon and electron  $d_0$  fluctuated periodically with respect to  $\phi$  in 2017 and 2018

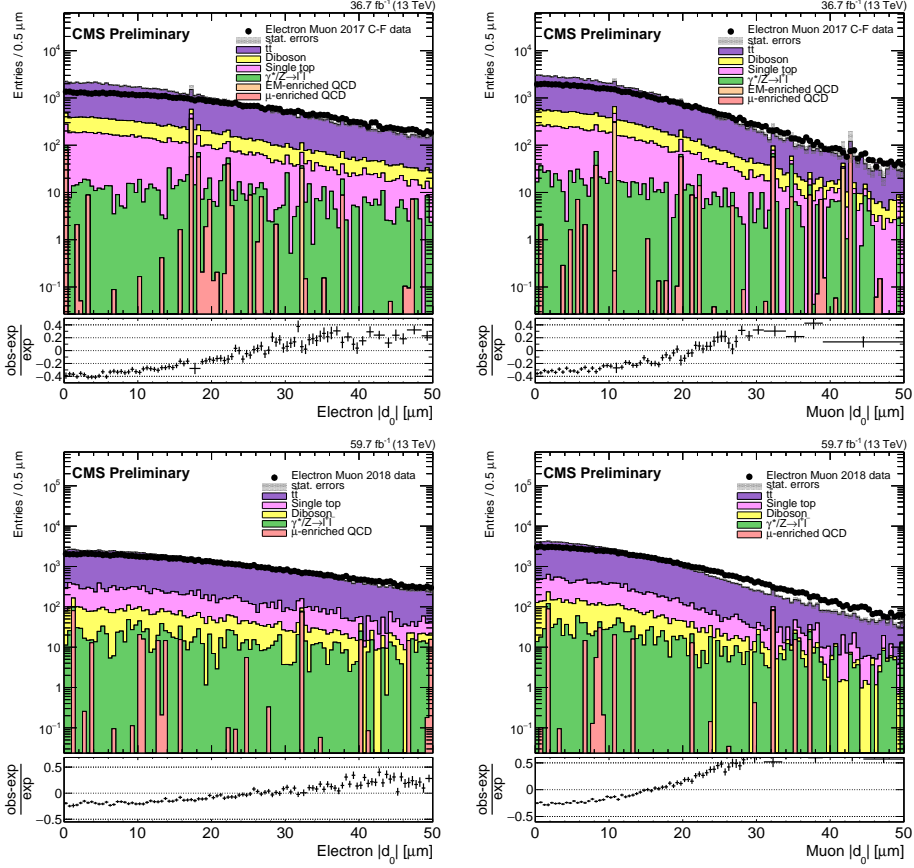


Figure 3.13: The uncorrected lepton  $|d_0|$  distributions in the  $e\mu$  prompt control region, for electrons (left) and muons (right), for 2017 data and simulation (upper), and 2018 data and simulation (lower). The rightmost bin in each plot contains the overflow entries.

1032 data but not in background simulation, as can be seen in Fig. 3.14. This periodic  
 1033 fluctuation in data but not in simulation indicates that an overly optimistic simu-  
 1034 lated tracker alignment is responsible for the unrealistically narrow  $d_0$  distribution in  
 1035 simulation.

1036 To account for the overly optimistic alignment in simulation, we smear the electron  
 1037 and muon  $d_0$  in 2017 and 2018 simulation in each channel's prompt control region to  
 1038 better model the  $d_0$  distribution in data. To do this, we first fit the central regions of

Table 3.7: The average  $\sigma_{align}$  for electrons and muons, for the 2017 and 2018 analyses.

	2017	2018
Electrons	$14.75 \pm 0.36 \mu\text{m}$	$9.18 \pm 0.41 \mu\text{m}$
Muons	$7.57 \pm 0.12 \mu\text{m}$	$8.11 \pm 0.08 \mu\text{m}$

1039 the background simulation and data  $d_0$  distributions with Gaussian functions in each  
 1040 channel's prompt control region and then compare the widths of the Gaussian fits.  
 1041 The fitted distributions are shown in Figs. 3.15 and 3.16 for the  $e\mu$  channel. Assuming  
 1042 that the width of each Gaussian fit is mostly determined by the  $d_0$  resolution, we define  
 1043  $\sigma_{data}^2 = \sigma_{bkg}^2 + \sigma_{align}^2$ , where  $\sigma_{data}$  is the data Gaussian width,  $\sigma_{bkg}$  is the uncorrected  
 1044 background simulation Gaussian width, and  $\sigma_{align}$  is the additional component that  
 1045 is needed to make up the difference in  $d_0$  resolution between background simulation  
 1046 and data. We find  $\sigma_{data}$  and  $\sigma_{bkg}$  from the fits and compute  $\sigma_{align}$ . The fit results are  
 1047 similar in the  $e\mu$  channel shown here and in the same-flavor channels. We average  
 1048 the  $\sigma_{align}$  derived in the  $ee$  channel and the  $e\mu$  channel for electrons, and in the  $\mu\mu$   
 1049 channel and the  $e\mu$  channel for muons. The average  $\sigma_{align}$  is shown in Table 3.7. We  
 1050 then smear the simulation  $d_0$  values with values drawn from a Gaussian distribution  
 1051 centered on zero and with a width of the average  $\sigma_{align}$ . The smearing is applied to  
 1052 both background and signal simulation. The corrected  $|d_0|$  distributions are shown  
 1053 in Fig. 3.17.

1054 This  $d_0$  smearing has a minimal effect on the final result because the width of the  
 1055 Gaussian distribution from which the smearing values are drawn is small relative to  
 1056 the size of the signal region bins, but understanding the source of the poor agreement

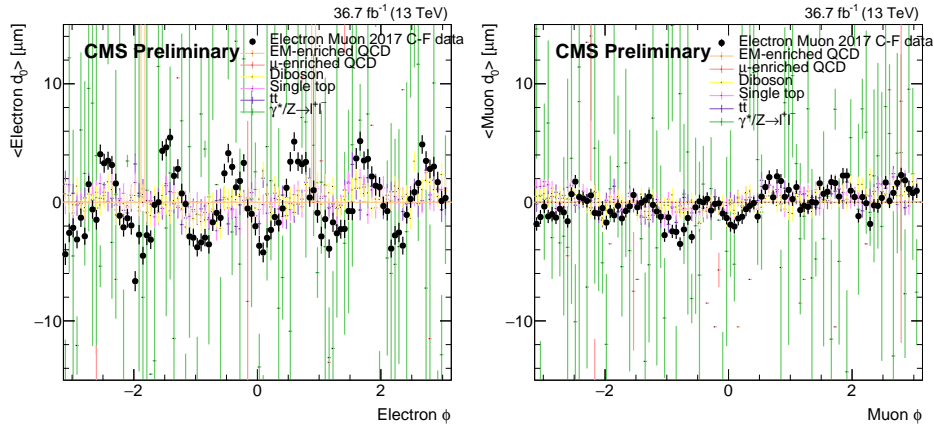


Figure 3.14: The average lepton  $|d_0|$  as a function of  $\phi$  in the  $e\mu$  prompt control region, for electrons (left) and muons (right), for 2017 data and simulation.

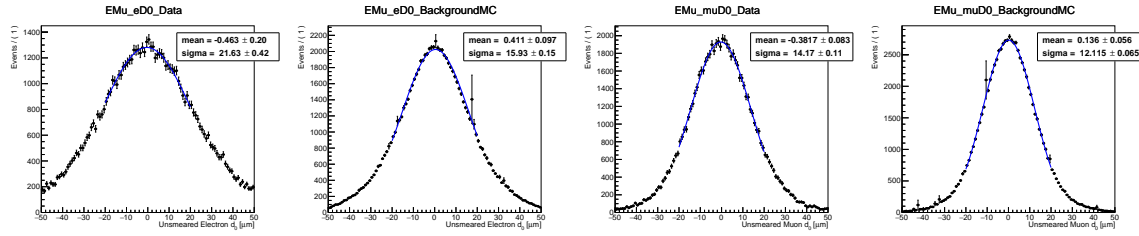


Figure 3.15: The lepton  $d_0$  distributions with Gaussian fits in the 2017  $e\mu$  prompt control region for (working from left to right) electrons in data, electrons in background simulation, muons in data, and muons in background simulation.

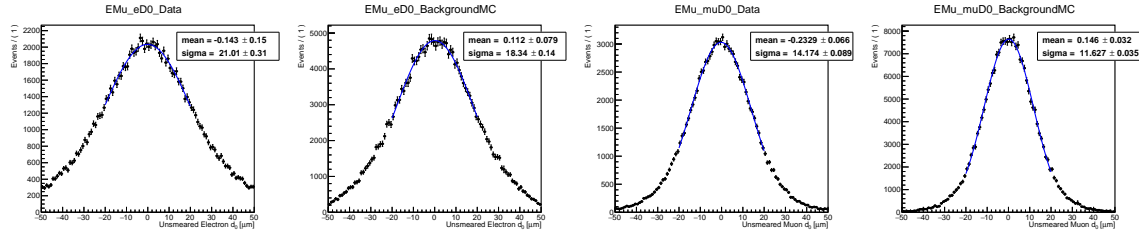


Figure 3.16: The lepton  $d_0$  distributions with Gaussian fits in the 2018  $e\mu$  prompt control region for (working from left to right) electrons in data, electrons in background simulation, muons in data, and muons in background simulation.

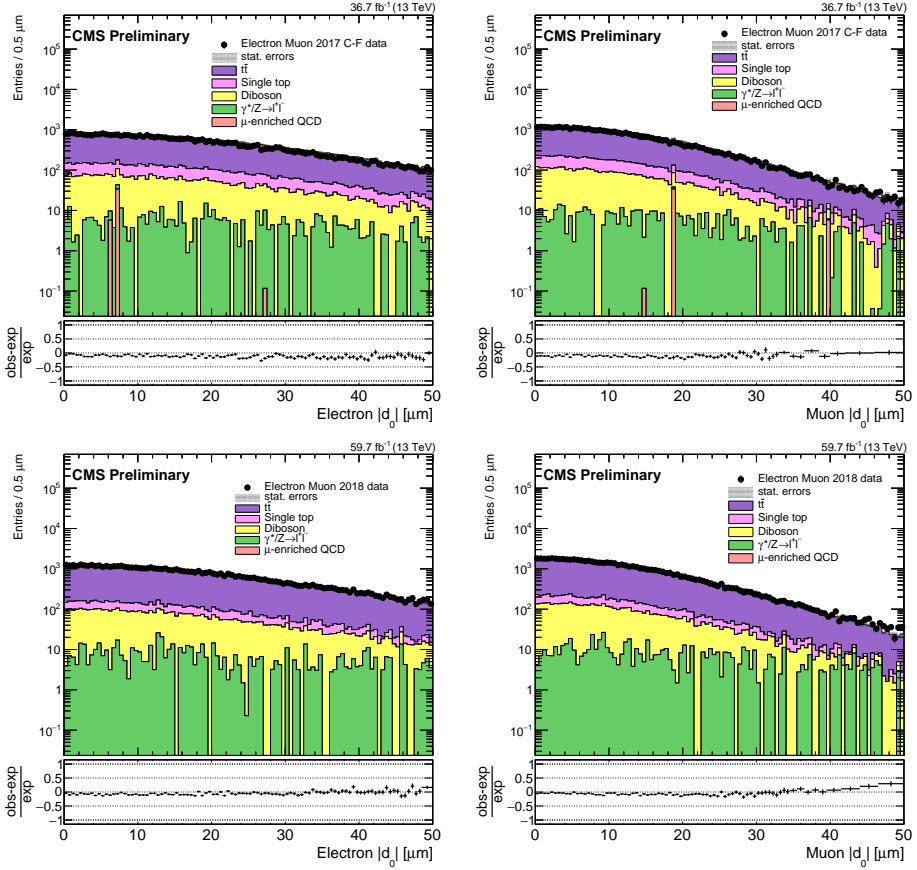


Figure 3.17: The corrected lepton  $|d_0|$  distributions in the  $e\mu$  prompt control region, for electrons (left) and muons (right), for 2017 data and simulation (upper), and 2018 data and simulation (lower). The rightmost bin in each plot contains the overflow entries.

1057 between data and simulation was important to validate our understanding of the SM  
1058 background.

1059 **3.4.4 Trigger efficiency**

1060 We also apply scale factors to the simulated background and signal events to cor-  
1061 rect for differences in trigger efficiency between data and simulation. To measure the  
1062 trigger efficiency, we first require that events pass an OR of several unprescaled  $p_T^{\text{miss}}$   
1063 triggers (see Table 3.8) and the preselection criteria with the lepton  $p_T$  requirement  
1064 excluded. The  $p_T^{\text{miss}}$  triggers provide a sample of dilepton events that is unbiased  
1065 with respect to the main triggers used in the analysis, and excluding the lepton  $p_T$   
1066 requirement allows us to study the trigger efficiency as a function of lepton  $p_T$ . In  
1067 the  $e\mu$  channel, the electron (muon)  $p_T$  is required to be greater than 50 GeV when  
1068 plotting against the muon (electron)  $p_T$  to disentangle the effect from the other leg of  
1069 the muon-photon trigger. Data events are taken from the MET primary dataset (which  
1070 contains events that pass  $p_T^{\text{miss}}$  trigger) and simulated background events are taken  
1071 from  $t\bar{t}$  simulation for the  $e\mu$  channel and Drell-Yan simulation for the same-flavor  
1072 channels. To calculate the efficiency, we divide the lepton  $p_T$  distribution in events  
1073 that pass the standard analysis triggers in addition to the OR of the  $p_T^{\text{miss}}$  triggers  
1074 and the preselection by the lepton  $p_T$  distribution in events that pass the OR of the  
1075  $p_T^{\text{miss}}$  triggers and the preselection. We then compute the scale factor as the ratio of  
1076 the efficiency in data to the efficiency in simulation in the plateau of the efficiency  
1077 distribution.

Table 3.8: The unprescaled  $p_T^{\text{miss}}$  triggers used to create an orthogonal data sample for the trigger efficiency calculation.

---

<b>2016</b>
HLT_MET200
HLT_MonoCentralPFJet80_PFMETNoMu110_PFMHTNoMu110_IDTight
HLT_PFMET120_PFMHT120_IDTight
HLT_PFMET170_HBHECleaned
HLT_PFMET300
HLT_PFMETNoMu120_PFMHTNoMu120_IDTight
<b>2017</b>
HLT_CaloMET350_HBHECleaned
HLT_MonoCentralPFJet80_PFMETNoMu120_PFMHTNoMu120_IDTight
HLT_PFMET120_PFMHT120_IDTight
HLT_PFMET250_HBHECleaned
HLT_PFMETNoMu120_PFMHTNoMu120_IDTight
<b>2018</b>
HLT_CaloMET350_HBHECleaned
HLT_MonoCentralPFJet80_PFMETNoMu120_PFMHTNoMu120_IDTight
HLT_PFMET120_PFMHT120_IDTight
HLT_PFMET200_HBHE_BeamHaloCleaned
HLT_PFMET250_HBHECleaned
HLT_PFMETNoMu120_PFMHTNoMu120_IDTight

---

1078 **3.5 Background estimation**

1079 **3.5.1 Background sources**

1080     The vast majority of leptons from SM processes are prompt. There are, however,  
1081     a few notable processes that produce leptons with large  $|d_0|$  values that may pass our  
1082     selection: (1) leptons from prompt decays whose  $|d_0|$  is poorly measured ("mismeas-  
1083     urements"), (2) leptons from decays of tau leptons ("taus"), and (3) leptons from  
1084     decays of B or D mesons ("heavy flavor"). Note that the leptons from these processes  
1085     generally do not share a common displaced vertex. We perform several cross checks  
1086     to ensure that processes in which leptons share a common displaced vertex do not  
1087     contribute significantly in the signal regions (SRs). Section 3.5.6 presents several  
1088     additional studies that confirm that the SR contribution of leptons from material  
1089     interactions, cosmic rays, and SM hadrons are either negligible or already accounted  
1090     for by the background estimation procedure.

1091     The  $|d_0|$  distributions of leptons from the three main background sources vary  
1092     according to lepton flavor and parent particle. Tau leptons have a lifetime of 87  $\mu\text{m}$ ,  
1093     B mesons have a lifetime around 500  $\mu\text{m}$ , and D mesons have a lifetime of around  
1094     100  $\mu\text{m}$ , so leptons from taus will generally have smaller  $|d_0|$  values than leptons from  
1095     heavy flavor. Furthermore, mismeasurements are more common for electrons than for  
1096     muons due to the superior muon  $d_0$  resolution. Figure 3.18, which shows the relative  
1097     contribution of each source of leptons as a function of  $|d_0|$  in simulated  $t\bar{t}$  events that  
1098     pass the  $e\mu$  channel preselection, shows how mismeasurements dominate at all  $|d_0|$   
1099     values for electrons while taus and heavy-flavor contribute meaningfully for muons  
1100     with  $|d_0| \gtrsim 100 \mu\text{m}$ .

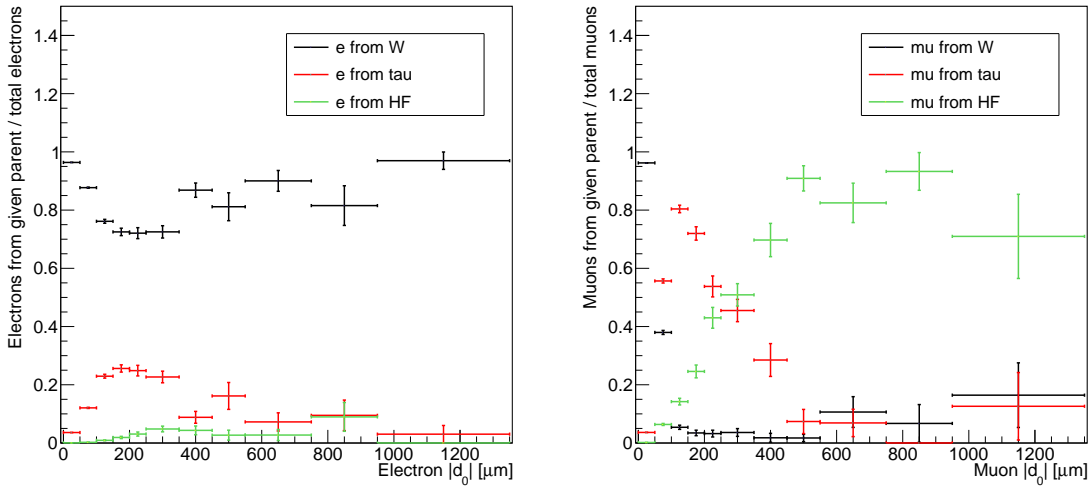


Figure 3.18: The fraction of electrons (left) and muons (right) from different parents as a function of lepton  $|d_0|$ , for simulated  $t\bar{t}$  events that pass the 2018  $e\mu$  channel preselection. In  $t\bar{t}$  events, the vast majority of leptons whose parent is a W boson are produced in a prompt decay.

1101 In the  $\mu\mu$  channel, it is worth examining which long-lived SM parents will con-  
 1102 tribute to  $|d_0|$ - $|d_0|$  correlation. The correlation specifically comes from DY-type pro-  
 1103 cesses in which the parentage is correlated between muons. Figure 3.19, which shows  
 1104 the fraction of muons from different background sources in DY simulation, indicates  
 1105 that tau lepton decays are the main source of muons that may be correlated in this  
 1106 way, and that the heavy-flavor contribution is negligible. This is reasonable because  
 1107 while tau leptons and heavy-flavor mesons both produce displaced muons, the iso-  
 1108 lation criteria rejects the vast majority of muons from heavy-flavor mesons. Muons  
 1109 from tau leptons contribute significantly from about 100 to 500  $\mu\text{m}$ , so we expect the  
 1110 most significant  $|d_0|$ - $|d_0|$  correlation to appear in this range and peak around 200  $\mu\text{m}$ .

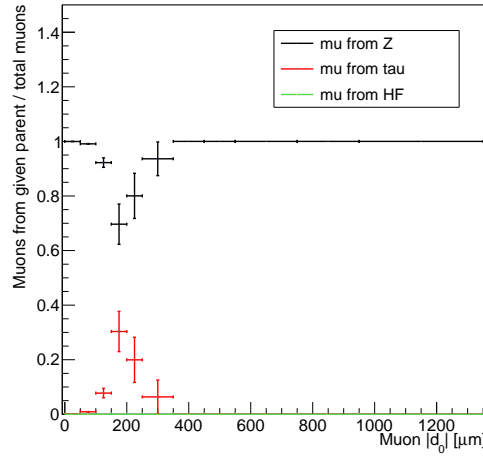


Figure 3.19: The fraction of muons from different parents as a function of muon  $|d_0|$ , for simulated DY events that pass the 2018  $\mu\mu$  channel preselection and the additional constraint that the leading and subleading muon both come from the same type of parent particle.

Furthermore, the correlation will be most pronounced in the regions where the  $|d_0|$  measurements are the best.

### 3.5.2 Data-driven ABCD method

We estimate the SR background yields with a data-driven method in which the leptons  $|d_0|$  distributions serve as composite models of all background processes. Specifically, we employ an ABCD method using the  $|d_0|$  of two leptons. We label the two  $|d_0|$  values in each channel as  $|d_0^a|$  and  $|d_0^b|$ , which correspond to the leading  $e$  and leading  $\mu$  in the  $e\mu$  channel, the leading and subleading  $e$  in the  $ee$  channel, and the leading and subleading  $\mu$  in the  $\mu\mu$  channel. As a first step, we categorize the events that pass the preselection criteria into four regions (A, B, C, and D) of the  $|d_0^a|$ - $|d_0^b|$  plane, as shown in Fig. 3.20.

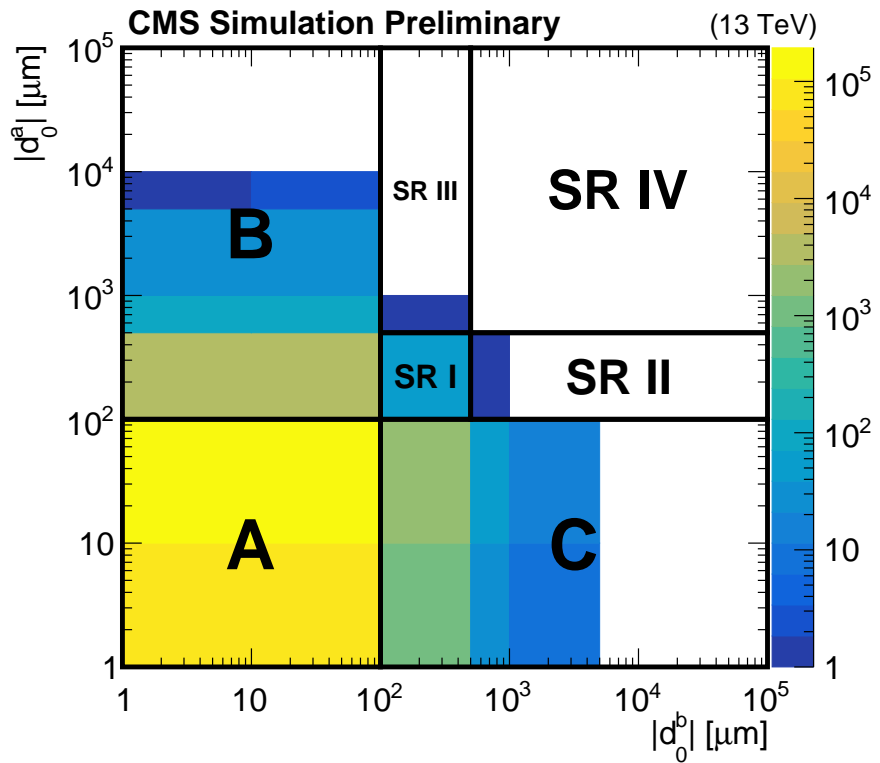


Figure 3.20: A diagram of the ABCD method overlaid on simulated background events passing the 2018  $e\mu$  preselection. A, B, and C are control regions, and D corresponds to the inclusive SR, which includes SRs I, II, III, and IV. Underflow events are included in the bins along the left and bottom edges. When performing the background estimate, regions B and C are further subdivided to coincide with the SR for which the estimate is being performed.

1122 We then use the number of events in regions A, B, and C to estimate the expected  
 1123 background in each SR. The basic estimation procedure depends on the assumption  
 1124 that  $|d_0^a|$  and  $|d_0^b|$  are uncorrelated. If this assumption holds, then  $N_B/N_A = N_D/N_C$   
 1125 and the number of background events in D is equal to  $N_B \times N_C/N_A$ , where  $N_X$  is  
 1126 the number of background events in the given region. We find that  $|d_0^a|$  and  $|d_0^b|$  are  
 1127 indeed uncorrelated over much of the  $|d_0|$ - $|d_0|$  plane, but the correlation discussed in  
 1128 Section 3.5.1 renders the basic ABCD method insufficient to estimate the background  
 1129 in SR I. After quantifying the degree of correlation in Section 3.5.3, we define a  
 1130 procedure to correct the basic ABCD estimate in Section 3.5.4.

1131 In order to maximize sensitivity to a wide range of new particle lifetimes, we  
 1132 further subdivide region D into the following four SRs:

- 1133 • SR I:  $100 \leq |d_0^a| < 500 \mu\text{m}$ ,  $100 < |d_0^b| < 500 \mu\text{m}$
- 1134 • SR II:  $100 \leq |d_0^a| < 500 \mu\text{m}$ ,  $500 \mu\text{m} < |d_0^b| < 10 \text{ cm}$
- 1135 • SR III:  $500 \mu\text{m} \leq |d_0^a| < 10 \text{ cm}$ ,  $100 < |d_0^b| < 500 \mu\text{m}$
- 1136 • SR IV:  $500 \mu\text{m} \leq |d_0^a| < 10 \text{ cm}$ ,  $500 \mu\text{m} < |d_0^b| < 10 \text{ cm}$

1137 The exact boundaries between the four SRs are motivated by the expected contribu-  
 1138 tions of the different background sources, as explained in 3.5.1. This approach also  
 1139 necessitates that the definitions of regions B and C vary in accordance with the SR for  
 1140 which a given estimate is performed (e.g. only the events in the  $100 \leq |d_0^a| < 500 \mu\text{m}$   
 1141 range of region B are considered when estimating the yields of SR I and II). Finally,  
 1142 we subdivide SR I into two bins using one lepton's  $p_T$  to further increase sensitivity to  
 1143 high-mass, low-lifetime new physics. Table 3.9 lists the  $p_T$  boundary in each channel  
 1144 and year.

Table 3.9: The  $p_T$  boundaries between the low- and high- $p_T$  bins of SR I in each channel.

	$p_T$ boundary [GeV]
2016 $e\mu$	leading $\mu$ $p_T = 90$
2017+2018 $e\mu$	leading $\mu$ $p_T = 140$
2016 $ee$	leading $e$ $p_T = 300$
2017+2018 $ee$	leading $e$ $p_T = 400$
2016 $\mu\mu$	leading $\mu$ $p_T = 100$
2017+2018 $\mu\mu$	leading $\mu$ $p_T = 100$

1145 When performing the background estimate and closure tests, we treat the 2016  
 1146 data and simulation separately from the 2017–2018 data and simulation to avoid  
 1147 any correlations between  $|d_0^a|$  and  $|d_0^b|$  that may arise from the differences between  
 1148 the original and Phase 1 pixel detectors employed by CMS in 2016 and 2017–2018,  
 1149 respectively (see Section 2.2.2).

### 1150 3.5.3 Closure tests in control regions

1151 We perform several closure tests of the background estimation procedure in data  
 1152 and simulation to test the method and quantify the degree of  $|d_0^a|-|d_0^b|$  correlation  
 1153 from the processes discussed in 3.5.1. Two series of tests are performed, the first in  
 1154 the 100–500 μm subregions of regions B and C and the second in the 500 μm–10 cm  
 1155 subregions of regions B and C.

#### 1156 100–500 μm tests

1157 We perform closure tests in subregions of regions B and C where one lepton is  
 1158 more prompt (20–100 μm) and the other is more displaced (100–500 μm). In these  
 1159 closure tests, we estimate the background yield using the simple ABCD method and

1160 then use the ratio of the actual number of events to the estimated number of events as  
1161 the measure of nonclosure (and therefore  $|d_0^a|$ - $|d_0^b|$  correlation). With this approach, a  
1162 ratio of 1 corresponds to closure and no  $|d_0^a|$ - $|d_0^b|$  correlation while ratios greater than  
1163 1 correspond to nonclosure and positive  $|d_0^a|$ - $|d_0^b|$  correlation. Using the procedure  
1164 outlined in Section 3.5.4, we estimate the corresponding degree of nonclosure in SR I  
1165 by fitting the resulting ratios and extrapolating from the closure test regions to SR I.  
1166 We perform identical procedures in regions B and C and then average the resulting  
1167 extrapolated ratios.

1168 Table 3.10 shows the average extrapolated ratios for three rounds of closure tests:  
1169 one in background simulation with the  $Z \rightarrow \tau\tau \rightarrow ll$  events removed, one in the full  
1170 background simulation, and one in data. The average extrapolated ratios are always  
1171 compatible with one in background simulation without  $Z \rightarrow \tau\tau \rightarrow ll$  events, but they  
1172 generally increase when the  $Z \rightarrow \tau\tau \rightarrow ll$  events are included. Furthermore, the average  
1173 extrapolated ratios from the full background simulation generally describe the average  
1174 extrapolated ratios in data. From these results, we conclude that within our statistical  
1175 uncertainties,  $Z \rightarrow \tau\tau \rightarrow ll$  events are the only meaningful source of correlation and that  
1176 the degree of correlation observed in data is modeled reasonably well in simulation.  
1177 We also observe that the variation in the degree of correlation across channels matches  
1178 our expectations: correlation increases with the number of muons in the final state  
1179 and is greater in 2017–2018 than 2016 because of the improved  $d_0$  resolution made  
1180 possible by the Phase-1 tracker upgrade (described in Section 2.2.2).

1181 **500  $\mu\text{m}$ –10 cm tests**

1182 We next perform closure tests in subregions of regions B and C where one lepton  
1183 is more prompt (20–100  $\mu\text{m}$ ) and the other is more displaced (500  $\mu\text{m}$ –10 cm). We

Table 3.10: Closure test results in background simulation (with and without  $Z \rightarrow \tau\tau \rightarrow ll$  events) and in data, in the 100–500  $\mu\text{m}$  region. The average extrapolated ratios and their statistical uncertainties are given. The A, B, C, and D regions are defined as follows: A is 20–30  $\mu\text{m}$  in prompt lepton  $|d_0|$  and 20–100  $\mu\text{m}$  in displaced lepton  $|d_0|$ , B is 20–30  $\mu\text{m}$  in prompt lepton  $|d_0|$  and 100–500  $\mu\text{m}$  in displaced lepton  $|d_0|$ , C is always 20–100  $\mu\text{m}$  in displaced lepton  $|d_0|$ , D (the test region) is always 100–500  $\mu\text{m}$  in displaced lepton  $|d_0|$ , and we perform repeated tests while simultaneously varying the C and D prompt lepton  $|d_0|$ s within the 30–100  $\mu\text{m}$  range.

	Bkg. simulation without $Z \rightarrow \tau\tau \rightarrow ll$	Full bkg. simulation	Data
2016 $e\mu$	$0.9 \pm 0.3$	$1.6 \pm 0.6$	$0.9 \pm 1.3$
2017+2018 $e\mu$	$1.1 \pm 0.4$	$1.6 \pm 0.7$	$3.1 \pm 1.0$
2016 $ee$	$0.8 \pm 0.5$	$0.8 \pm 0.5$	$0.6 \pm 0.6$
2017+2018 $ee$	$0.8 \pm 1.0$	$1.6 \pm 0.9$	$1.5 \pm 0.4$
2016 $\mu\mu$	$1.1 \pm 0.8$	$2.0 \pm 0.8$	$2.5 \pm 1.0$
2017+2018 $\mu\mu$	$2.6 \pm 2.8$	$7.8 \pm 3.7$	$4.2 \pm 1.8$
Average	$1.2 \pm 0.5$	$2.6 \pm 0.7$	$2.1 \pm 0.5$

again use the ratio of the actual number of events to the estimated number of events  
 as the measure of nonclosure, but in these tests we expect the ratio to be consistent  
 with one because  $Z \rightarrow \tau\tau \rightarrow ll$  events do not contribute meaningfully beyond 500  $\mu\text{m}$ .  
 Table 3.11 shows that this is indeed the case for background simulation (with and  
 without  $Z \rightarrow \tau\tau \rightarrow ll$  events) and for data. These results imply that  $|d_0^a|$  and  $|d_0^b|$  are  
 uncorrelated beyond 500  $\mu\text{m}$ , which means that a simple ABCD procedure will be  
 adequate for estimating the background yields in SRs II, III, and IV.

### 3.5.4 ABCD correction and systematic uncertainty

The closure tests of Section 3.5.3 show that  $|d_0^a|$  and  $|d_0^b|$  are frequently positively  
 correlated in the 100–500  $\mu\text{m}$  region but are uncorrelated otherwise. To account for  
 this correlation as well as other possible unforeseen sources of nonclosure, we define

Table 3.11: Closure test results in data and background simulation (with and without  $Z \rightarrow \tau\tau \rightarrow ll$  events), in the 500  $\mu\text{m}$ –10 cm region. The ratios of the actual yield to the estimated yield and their statistical uncertainties are given. The A, B, C, and D regions are defined as follows: A is 20–30  $\mu\text{m}$  in prompt lepton  $|d_0|$  and 20–100  $\mu\text{m}$  in displaced lepton  $|d_0|$ , B is 20–30  $\mu\text{m}$  in prompt lepton  $|d_0|$  and 500  $\mu\text{m}$ –10 cm in displaced lepton  $|d_0|$ , C is 30–100  $\mu\text{m}$  in prompt lepton  $|d_0|$  and 20–100  $\mu\text{m}$  in displaced lepton  $|d_0|$ , and D (the test region) is 30–100  $\mu\text{m}$  in prompt lepton  $|d_0|$  and 500  $\mu\text{m}$ –10 cm in displaced lepton  $|d_0|$ .

Region B			
	Bkg. simulation without $Z \rightarrow \tau\tau \rightarrow ll$	Bkg. simulation	Data
2016 $e\mu$	$1.1^{+0.3}_{-0.3}$	$1.1^{+0.3}_{-0.3}$	$0.4^{+1.0}_{-0.4}$
2017+2018 $e\mu$	$0.9^{+0.3}_{-0.2}$	$0.9^{+0.3}_{-0.2}$	$0.7^{+0.3}_{-0.3}$
2016 $ee$	$0.4^{+0.6}_{-0.3}$	$0.4^{+0.6}_{-0.3}$	$1.4^{+1.6}_{-0.9}$
2017+2018 $ee$	$0.5^{+0.8}_{-0.4}$	$0.3^{+0.4}_{-0.2}$	$1.0^{+0.3}_{-0.3}$
2016 $\mu\mu$	$0.7^{+0.3}_{-0.3}$	$0.7^{+0.3}_{-0.3}$	$0.8^{+0.3}_{-0.3}$
2017+2018 $\mu\mu$	$0.8^{+1.8}_{-0.7}$	$0.4^{+1.0}_{-0.4}$	$1.8^{+0.6}_{-0.7}$

Region C			
	Bkg. simulation without $Z \rightarrow \tau\tau \rightarrow ll$	Bkg. simulation	Data
2016 $e\mu$	$0.8^{+0.4}_{-0.3}$	$0.8^{+0.4}_{-0.3}$	1.0 (0 vs 0)
2017+2018 $e\mu$	$0.8^{+0.3}_{-0.2}$	$0.8^{+0.3}_{-0.2}$	$0.7^{+1.3}_{-0.7}$
2016 $ee$	$4.0^{+5.8}_{-3.1}$	$4.0^{+5.8}_{-3.1}$	$0.7^{+1.0}_{-0.6}$
2017+2018 $ee$	$3.5^{+2.6}_{-1.8}$	$2.1^{+2.6}_{-1.5}$	$1.0^{+0.3}_{-0.3}$
2016 $\mu\mu$	$1.2^{+0.5}_{-0.4}$	$1.3^{+0.6}_{-0.4}$	$0.6^{+0.4}_{-0.3}$
2017+2018 $\mu\mu$	$0.4^{+0.4}_{-0.3}$	$0.5^{+0.5}_{-0.3}$	$0.5^{+0.3}_{-0.2}$

1195 a procedure to correct the simple ABCD estimate in SR I and assign a systematic  
1196 uncertainty to the simple ABCD estimate in all SRs.

1197 **100–500  $\mu\text{m}$  correction and systematic uncertainty**

1198 Figures 3.21, 3.22, and 3.23 show the results of the data closure tests in the  $e\mu$ ,  
1199  $ee$ , and  $\mu\mu$  channels, respectively, in the one-prompt (20–100  $\mu\text{m}$ )/one-displaced (100–  
1200 500  $\mu\text{m}$ ) sidebands. These plots show the ratio of the actual to the estimated number  
1201 of events as a function of the prompt lepton  $|d_0|$ . In all of these plots, the binning of  
1202 the prompt lepton axis is initially 10  $\mu\text{m}$  wide. Starting from most-displaced bin, we  
1203 test to see if any bin has fewer than 5 events, and if so, we combine it with whichever  
1204 neighboring bin has fewer events, repeating until all bins have at least 5 events.

1205 In each of the two sidebands, we then fit the resulting ratios with a straight  
1206 line, where the slope and y-intercept are allowed to vary, and extrapolate the fit to  
1207 200  $\mu\text{m}$ , which is where we expect the largest contribution from tau lepton decays (see  
1208 Section 3.5.1). 200  $\mu\text{m}$  also happens to be approximately the center-of-mass of the  
1209 100–500  $\mu\text{m}$  bin in background simulation. We average the two extrapolated ratios  
1210 and derive a correction and systematic uncertainty from this average extrapolated  
1211 ratio.

1212 If the average extrapolated ratio is  $> 1.0$ , we take the central value as a multi-  
1213 plicative correction to the background estimate and the uncertainty in the average as  
1214 a systematic uncertainty in the background estimate. In this case, we also vary the  
1215 200  $\mu\text{m}$  extrapolation point by  $\pm 50 \mu\text{m}$  (the approximate width of the peak in the tau  
1216 lepton contribution as a function of  $|d_0|$ ). We apply the difference from this varia-  
1217 tion in extrapolation point as an additional systematic uncertainty in the background

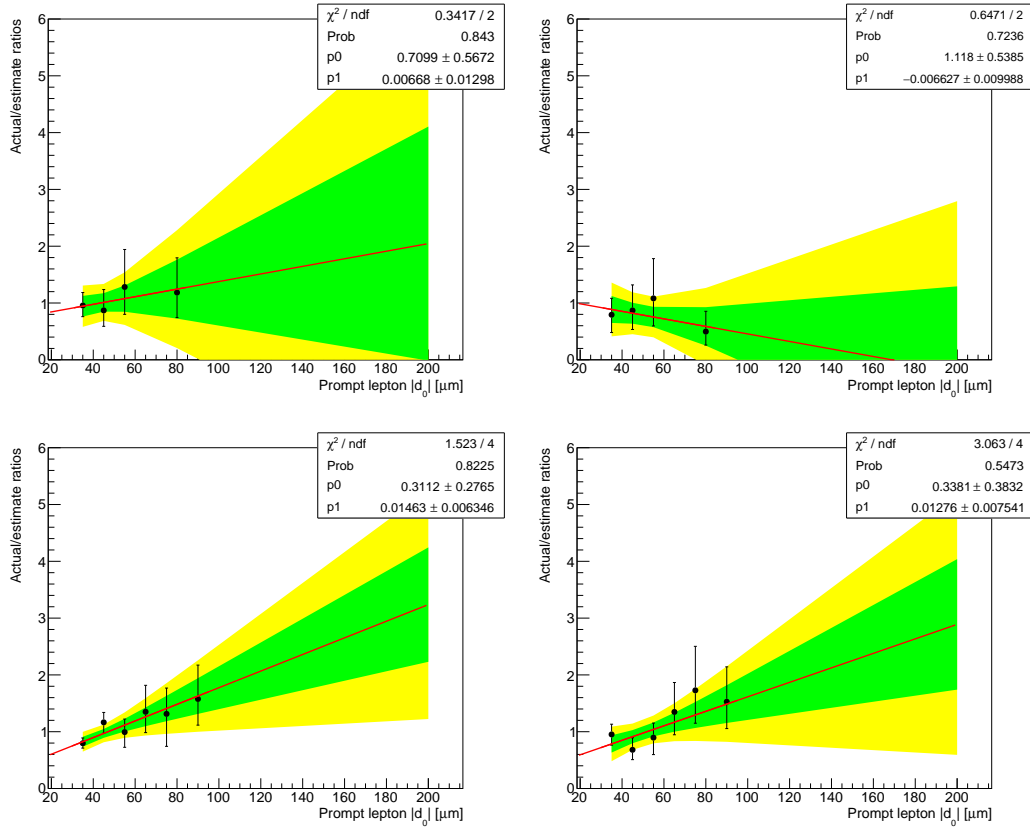


Figure 3.21: Background estimation closure tests in data, in 100–500  $\mu\text{m}$  subregions of regions B (left) and C (right) in the  $e\mu$  channel. Each plot shows the ratio of the actual to the estimated number of events as a function of the prompt lepton  $|d_0|$  in 2016 (top) and 2017–18 (bottom). A linear fit is shown in black along with the 68 % and 95 % confidence intervals of the extrapolated fit value.

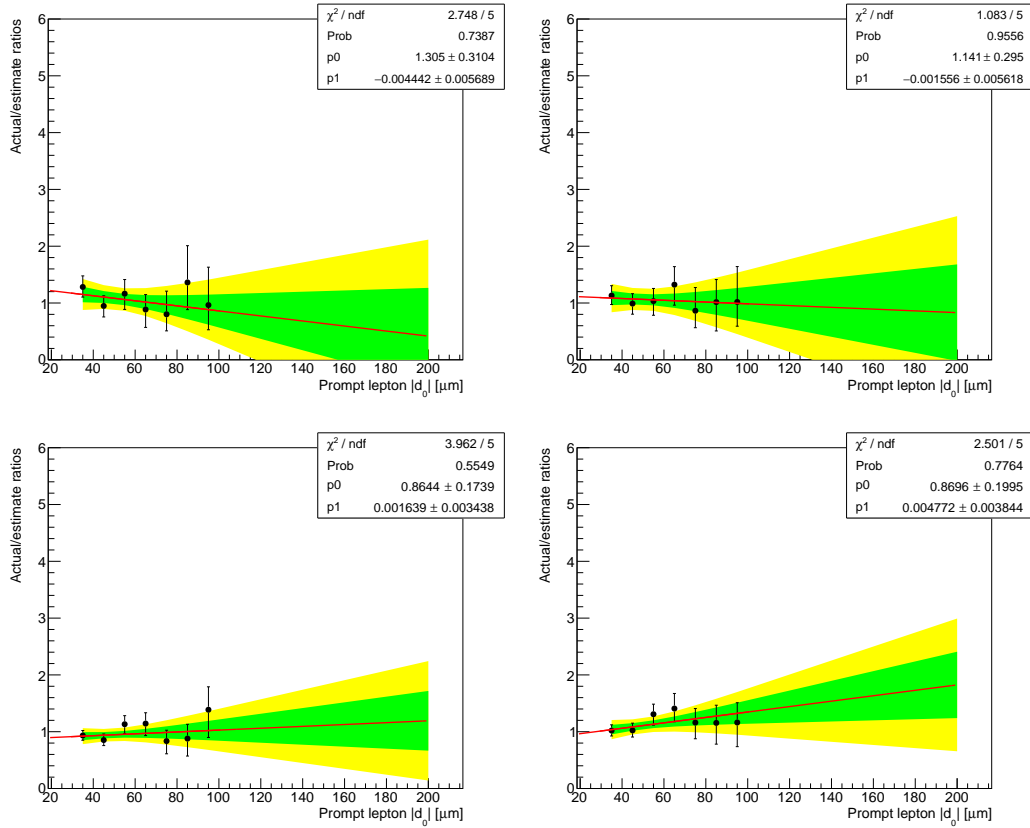


Figure 3.22: Background estimation closure tests in data, in  $100\text{--}500\,\mu\text{m}$  subregions of regions B (left) and C (right) in the  $ee$  channel. Each plot shows the ratio of the actual to the estimated number of events as a function of the prompt lepton  $|d_0|$  in 2016 (top) and 2017–18 (bottom). A linear fit is shown in black along with the 68 % and 95 % confidence intervals of the extrapolated fit value.

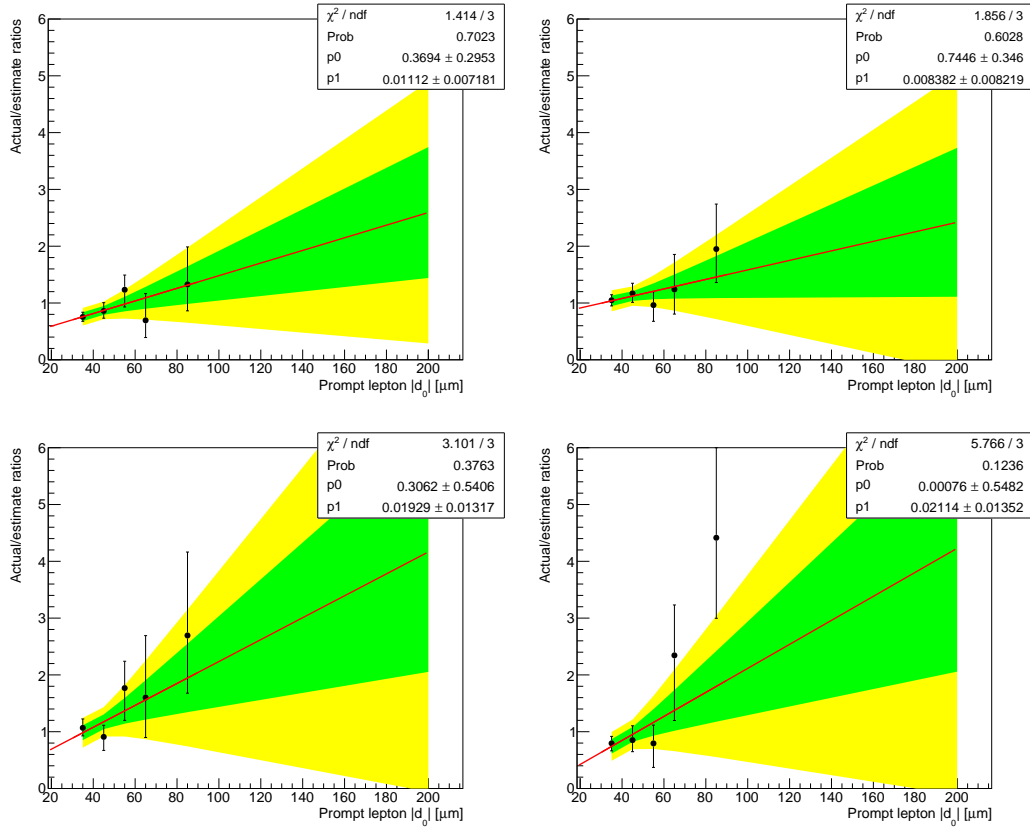


Figure 3.23: Background estimation closure tests in data, in 100–500  $\mu\text{m}$  subregions of regions B (left) and C (right) in the  $\mu\mu$  channel. Each plot shows the ratio of the actual to the estimated number of events as a function of the prompt lepton  $|d_0|$  in 2016 (top) and 2017–18 (bottom). A linear fit is shown in black along with the 68 % and 95 % confidence intervals of the extrapolated fit value.

Table 3.12: The correction factors and the uncorrected and corrected background estimates in SR I . The correction factor uncertainties include both the uncertainty in the average and the additional uncertainty obtained from varying the fit extrapolation point. The total uncertainty (statistical plus systematic) is given for the corrected background estimates.

	Correction factor	Uncorrected estimate	Corrected estimate
2016 $e\mu$	$1.0^{+1.3}_{-1.0}$	$4.21^{+0.38}_{-0.40}$	$4.2^{+5.4}_{-4.2}$
2017+2018 $e\mu$	$3.0 \pm 1.0$	$12.53^{+0.64}_{-0.61}$	$38 \pm 13$
2016 $ee$	$1.00 \pm 0.60$	$18.30^{+0.94}_{-0.91}$	$18 \pm 11$
2017+2018 $ee$	$1.51^{+0.43}_{-0.42}$	$41.6 \pm 1.3$	$63^{+18}_{-17}$
2016 $\mu\mu$	$2.5 \pm 1.0$	$3.07 \pm 0.08$	$7.7 \pm 3.1$
2017+2018 $\mu\mu$	$4.2 \pm 1.8$	$1.00 \pm 0.04$	$4.2 \pm 1.8$

1218 estimate. If the average is  $\leq 1.0$ , we set the correction equal to 1.0 and use the un-  
 1219 certainty in the average as a symmetric systematic uncertainty about 1.0. Table 3.12  
 1220 shows the resulting correction factors along with the uncorrected and corrected SR I  
 1221 background estimate.

1222 **500  $\mu\text{m}$ –10 cm systematic uncertainty**

1223 In the 500  $\mu\text{m}$ –10 cm region, we derive a systematic uncertainty in the background  
 1224 estimate from the data closure tests shown in Section 3.5.3. We take the largest  
 1225 deviation from 1.0 that occurs in the ratio of the actual to the estimated number  
 1226 of events plus its uncertainty, in either of the two closure tests that correspond to a  
 1227 given SR, as a systematic uncertainty. This is a conservative approach that produces  
 1228 a large systematic uncertainty in the small background yields that we predict in these  
 1229 regions. Table 3.13 shows the systematic uncertainty and the predicted number of  
 1230 events in SRs II, III, and IV.

Table 3.13: The systematic uncertainty and the background estimates in SRs II, III, and IV. The total uncertainty (statistical plus systematic) is given for each estimate.

	Systematic uncertainty	SR II	SR III	SR IV
2016 $e\mu$	98%	$0.15 \pm 0.15$	$0.09^{+0.12}_{-0.09}$	$0.003^{+0.004}_{-0.003}$
2017+2018 $e\mu$	106%	$0.71^{+0.76}_{-0.71}$	$0.23^{+0.27}_{-0.23}$	$0.01^{+0.02}_{-0.01}$
2016 $ee$	199%	$0.51^{+1.02}_{-0.51}$	$0.43^{+0.85}_{-0.43}$	$0.01^{+0.02}_{-0.01}$
2017+2018 $ee$	37%	$3.6 \pm 1.4$	$2.8 \pm 1.1$	$0.24^{+0.10}_{-0.09}$
2016 $\mu\mu$	64%	$0.17 \pm 0.11$	$0.19 \pm 0.12$	$0.01 \pm 0.01$
2017+2018 $\mu\mu$	140%	$0.14^{+0.19}_{-0.14}$	$0.08^{+0.12}_{-0.08}$	$0.01^{+0.02}_{-0.01}$

### 1231 3.5.5 Testing full background estimation procedure

1232 Having defined the full background estimation procedure and seen that the  $|d_0^a|$ -  
 1233  $|d_0^b|$  correlation observed in data is also present in simulated background events, we  
 1234 now perform a final closure test of the full background estimation method using  
 1235 simulated background events in SRs I–IV.

1236 Table 3.14 shows the estimated and actual number of simulated background events  
 1237 in SRs I–IV. The listed estimates include all corrections and statistical and system-  
 1238 atic uncertainties as discussed in 3.5.4. The uncertainties in the actual values are  
 1239 purely statistical. The general agreement between estimated and actual yields leads  
 1240 us to conclude that the background estimation procedure is valid and the assigned  
 1241 systematic uncertainties are sufficient to cover any potential sources of nonclosure  
 1242 that we have not explicitly considered.

Table 3.14: Closure test results in background simulation in the SRs, with the correction applied. The estimated number of events, the actual number of events, and their total uncertainties (statistical plus systematic) are given. In cases where the actual number of events is zero, the uncertainty is given by the product of the average background simulation event weight and the upper bound of the 68% Poisson interval given by a single observation of zero events.

	SR I	SR II	SR III	SR IV
2016 $e\mu$ estimated	$7.4^{+4.8}_{-4.2}$	$0.07 \pm 0.07$	$0.096^{+0.105}_{-0.096}$	$0.001 \pm 0.001$
2016 $e\mu$ actual	$5.0^{+1.5}_{-1.2}$	$0.07^{+0.09}_{-0.05}$	$0.005^{+0.011}_{-0.004}$	$0.000^{+0.037}_{-0.000}$
2017+2018 $e\mu$ estimated	$13.5 \pm 6.4$	$0.37^{+0.40}_{-0.37}$	$0.34^{+0.36}_{-0.34}$	$0.02 \pm 0.02$
2017+2018 $e\mu$ actual	$19.1^{+11.4}_{-7.6}$	$0.52^{+0.41}_{-0.25}$	$0.00^{+0.24}_{-0.00}$	$0.00^{+0.24}_{-0.00}$
2016 $ee$ estimated	$9.3 \pm 5.0$	$0.12^{+0.23}_{-0.12}$	$0.14^{+0.28}_{-0.14}$	$0.002^{+0.004}_{-0.002}$
2016 $ee$ actual	$13.4^{+3.4}_{-2.8}$	$0.15^{+0.19}_{-0.09}$	$1.03^{+1.36}_{-0.67}$	$0.000^{+0.550}_{-0.000}$
2017+2018 $ee$ estimated	$18 \pm 11$	$0.59^{+0.27}_{-0.26}$	$0.45^{+0.21}_{-0.20}$	$0.02 \pm 0.01$
2017+2018 $ee$ actual	$8.2^{+6.5}_{-3.9}$	$0.17^{+0.23}_{-0.11}$	$0.00^{+0.17}_{-0.00}$	$0.00^{+0.17}_{-0.00}$
2016 $\mu\mu$ estimated	$1.3 \pm 0.6$	$0.04 \pm 0.04$	$0.03 \pm 0.03$	$0.002 \pm 0.002$
2016 $\mu\mu$ actual	$3.3^{+1.8}_{-1.2}$	$0.11^{+0.14}_{-0.07}$	$0.06^{+0.14}_{-0.05}$	$0.000^{+0.110}_{-0.000}$
2017+2018 $\mu\mu$ estimated	$2.7 \pm 1.4$	$0.04 \pm 0.04$	$0.02 \pm 0.02$	$0.002 \pm 0.002$
2017+2018 $\mu\mu$ actual	$7.1^{+6.9}_{-3.8}$	$0.00^{+0.15}_{-0.00}$	$0.00^{+0.15}_{-0.00}$	$0.078^{+0.179}_{-0.064}$

1243 **3.5.6 Additional background checks**

1244 We perform a few additional studies to check for other potential sources of back-  
1245 ground. We find that their SR contributions are either negligible or already covered  
1246 by the background estimation method described above.

1247 **Material interactions**

1248 In order to further study the material interactions, we invert the preselection  
1249 criterion that rejects good vertices in the material. In data, we find seven events,  
1250 across all channels and years, that pass the preselection with this inverted criterion.  
1251 As shown in Table 3.15, three of these events are in the prompt control region and  
1252 four are in region B or region C. The lepton vertices in these events coincide with the  
1253 material as we expect: two are in the beampipe, one is in the pixel detector inner  
1254 shield, and four are in the first layer of the pixel detector. Even with the material  
1255 interaction veto inverted, we find no SR events resulting from material interactions  
1256 and therefore conclude that material interactions are not a significant background  
1257 after the full selection is applied.

Table 3.15: Some properties of the seven events found in data with the material interactions selection inverted.

Channel, Era	$( d_0^a ,  d_0^b )$ [μm]	Region	Vertex (x, y, z) [cm]	Material
$e\mu$ , 2017C	(-14, -10)	A	(-2.5, 1.4, 6.8)	pixel L1
$e\mu$ , 2018D	(46, -14)	A	(0.9, 2.1, 0.1)	beampipe
$ee$ , 2018D	(198, -34)	B	(-1.9, 0.5, 2.7)	beampipe
$\mu\mu$ , 2016G	(407, -8)	B	(-1.4, 4.0, 6.3)	pixel L1
$\mu\mu$ , 2016G	(-17, -2215)	C	(-2.6, 3.1, 6.6)	pixel L1
$\mu\mu$ , 2016H	(2, 0)	A	(-1.6, -3.5, 12)	inner shield
$\mu\mu$ , 2017F	(522, -13)	B	(-1.1, -3.0, -7.5)	pixel L1

1258 **Cosmic-ray muons**

1259 To estimate the SR contribution of cosmic-ray muons, we perform a study in which  
1260 we invert the  $\Delta t$  and  $\cos \alpha$  criteria in the  $\mu\mu$  preselection and check how many events  
1261 are in the SRs. We find three data events with the criteria inverted (one event per year,  
1262 all in SR IV). Next, we use NoBPTX data, which is dominated by cosmic-ray muon  
1263 events, to estimate the efficiency for cosmic-ray muons to pass the  $\Delta t$  and  $\cos(\alpha)$   
1264 criteria after passing the rest of the  $\mu\mu$  preselection criteria. While 3736 NoBPTX  
1265 data events pass the preselection criteria with the  $\Delta t$  and  $\cos(\alpha)$  criteria removed,  
1266 zero NoBPTX data events pass the full preselection. To conservatively estimate the  
1267 efficiency, we fluctuate the number of passing events up to 1 and find an efficiency  
1268 of  $1/3736$ . We therefore find the approximate upper bound on the SR contribution  
1269 of cosmic ray muons to be  $3 \times \frac{1}{3736} = 0.0008$ , which is negligible compared to the  
1270 background estimation in each SR.

1271 **Heavy-flavor mesons**

1272 We perform two studies to estimate an upper limit on the SR contribution of  
1273 leptons from heavy-flavor mesons. First, we estimate SR yields with a simple ABCD  
1274 method in 2018  $\mu\mu$  preselection data while additionally requiring at least one medium  
1275 CSVv2  $b$ -tagged jet. The test is performed in the  $\mu\mu$  channel because it contains  
1276 the smallest relative SR contribution from mismeasurements and should therefore be  
1277 most sensitive to heavy flavor. As shown in Table 3.16, the background estimates  
1278 are about an order of magnitude smaller than when no  $b$  jet is required in our usual  
1279 preselection.

Table 3.16: Background estimates in data while applying the 2018  $\mu\mu$  preselection and the additional requirement of at least one medium  $b$ -tagged jet. The estimates with at least one  $b$  jet are about an order of magnitude below the nominal prediction.

	SR I	SR II	SR III	SR IV
Preselection (corrected)	$2.6 \pm 1.0$	$0.09^{+0.12}_{-0.09}$	$0.05^{+0.07}_{-0.05}$	$0.007^{+0.010}_{-0.007}$
Preselection + 1 $b$ jet	$0.19 \pm 0.03$	$0.008^{+0.007}_{-0.004}$	$0.005^{+0.004}_{-0.002}$	$0.0002^{+0.0002}_{-0.0001}$

1280        Next, we look at 2018 data and simulated QCD multijet events that pass the  $\mu\mu$   
 1281        preselection with the isolation criterion inverted. These samples are dominated by  
 1282        muons from B meson decays, and the QCD simulation describes the data well in the  
 1283        region outside of the  $Z$  boson peak, as shown in Fig. 3.24. We use this QCD multijet  
 1284        sample to test the heavy-flavor background in two ways. First, we perform a simple  
 1285        ABCD estimate in the simulated QCD multijet events to check for  $|d_0^a| - |d_0^b|$  correlation.  
 1286        As shown in Table 3.17, we find no evidence of correlation, which indicates that the  
 1287        background estimation already accounts for the heavy-flavor background. Second,  
 1288        we estimate the approximate heavy-flavor background in the SRs by taking the ratio  
 1289        of SR to prompt control region events in QCD multijet simulation from the anti-  
 1290        isolated region and the normalization from the number of simulated QCD multijet  
 1291        events that pass the  $\mu\mu$  preselection. Using this approach, we estimate that the  
 1292        heavy-flavor background to be  $0.06^{+0.13}_{-0.05}$  events in SR I and  $0.0015^{+0.0034}_{-0.0012}$  events in  
 1293        SR IV, which is small relative to the nominal prediction shown in the first row of  
 1294        Table 3.16.

1295        We therefore conclude that the heavy-flavor SR contribution is small and already  
 1296        accounted for in our background estimates.

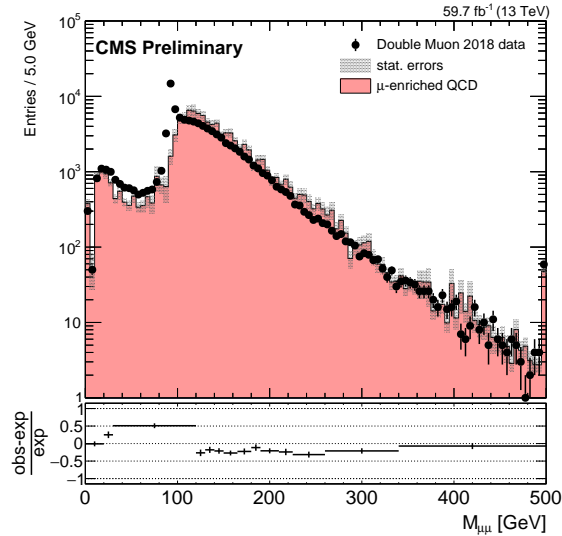


Figure 3.24: The dimuon invariant mass distribution in the  $\mu\mu$  channel with the muon isolation criterion inverted, for 2018 data and QCD multijet simulation.

Table 3.17: A closure test of the ABCD method in 2018 QCD simulation in the  $\mu\mu$  channel with the muon isolation criterion inverted. The estimates from the ABCD method, the actual yields in simulation, and the ratios of the actual to the estimated yields are shown.

Region	Estimated yield	Actual yield	Ratio of actual to estimate
SR I	$9500 \pm 1100$	$11000 \pm 1000$	$1.2 \pm 0.2$
SR II	$1740^{+310}_{-280}$	$2200^{+330}_{-290}$	$1.3 \pm 0.3$
SR III	$1450^{+280}_{-240}$	$1500^{+180}_{-160}$	$1.0 \pm 0.2$
SR IV	$265^{+62}_{-54}$	$268^{+61}_{-50}$	$1.0 \pm 0.3$

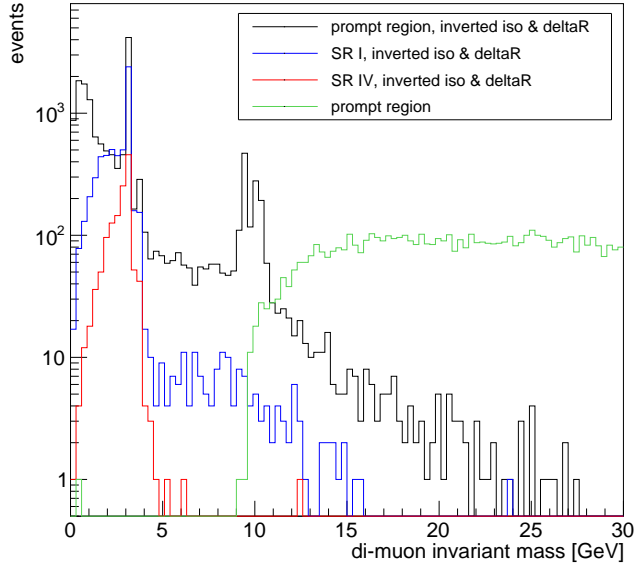


Figure 3.25: The dimuon invariant mass distribution in 2018 data in the  $\mu\mu$  channel, in the prompt control region (black), SR I (blue), SR IV (red), with the muon isolation and di-muon  $\Delta R$  criteria inverted. The equivalent distribution from the prompt control region is also shown in green.

1297 **Low-mass SM hadrons**

1298 To estimate an upper limit on the SR contribution of leptons from decays of low-  
1299 mass SM hadrons, we examine 2018 data and QCD multijet simulation in the  $\mu\mu$   
1300 channel with both the muon isolation and the  $\Delta R$  requirements inverted. As shown  
1301 in Fig. 3.25, this region is dominated low-mass  $\mu\mu$  pairs, with clear  $J/\psi$ ,  $\psi'$ , and  $\Upsilon$   
1302 mass peaks. Many of these leptons are displaced, especially those in the  $J/\psi$  mass  
1303 range. To estimate the fraction of such leptons that will be displaced, we take the  
1304 ratio of SR to prompt control region events of SM hadrons that decay to leptons from  
1305 data in this region.

1306 Even though the inverted-isolation region is dominated by low-mass muon pairs,  
1307 the only QCD multijet simulation event that survives the 2018  $\mu\mu$  preselection has  
1308 a di-muon invariant mass of approximately 300 GeV. Furthermore, the muons are  
1309 not near each other in the  $\eta$ - $\phi$  plane ( $\Delta R \approx 3$ ), which is inconsistent with the low-  
1310 mass SM hadron events that dominate the region with the inverted isolation and  $\Delta R$   
1311 criteria. To find a normalization from which to estimate the low-mass SM hadron  
1312 SR contribution, we therefore turn to the inverted-isolation sample used above in the  
1313 heavy-flavor meson cross check. In this sample, the ratio of events with  $\Delta R < 0.5$   
1314 to events with  $2.8 < \Delta R < 3.2$  is about 0.1. We find 0.2 QCD multijet simulated  
1315 events that pass the nominal preselection, and so we estimate that of the events  
1316 passing the 2018  $\mu\mu$  preselection, about 0.02 contain pairs of muons produced in low-  
1317 mass SM hadron decays. We estimate the SR contributions using this preselection  
1318 normalization and the ratio of SR to prompt control region events from the sample  
1319 of SM hadrons that decay to leptons in data. We find this contribution is less than  
1320  $0.006^{+0.013}_{-0.005}$  events in SR I and less than  $0.001^{+0.002}_{-0.001}$  events in SR IV, which, if compared  
1321 with the nominal prediction shown in the first row of Table 3.24, are respectively  
1322 negligible and easily covered by the 140 % systematic uncertainty already applied to  
1323 the background prediction in this region.

1324 **3.6 Systematic uncertainties**

1325 Several systematic uncertainties are applied to the simulated signal efficiency to  
1326 account for uncertainty in the signal yields arising from possible mismodeling of the  
1327 detector conditions and response. The following subsections describe each systematic  
1328 uncertainties in turn, and Table 3.18 summarizes all systematic uncertainties applied  
1329 to the simulated signal.

1330 **3.6.1 Integrated luminosity**

1331 The integrated luminosities of the 2016, 2017, and 2018 data-taking periods are  
1332 individually known with uncertainties in the 2.3–2.5 % range [70, 71, 72], while the  
1333 total Run 2 (2016–2018) integrated luminosity has an uncertainty of 1.8 %, the im-  
1334 provement in precision reflecting the uncorrelated time evolution of some systematic  
1335 effects. The full table of 2016–2018 integrated luminosity uncertainties are taken from  
1336 Ref. [73], with the correlations specified therein.

1337 **3.6.2 Pileup**

1338 The simulation of pileup events assumes a total inelastic proton-proton cross sec-  
1339 tion of 69.2 mb with an associated uncertainty of 5 % [74]. The systematic uncertainty  
1340 arising as a result of the modeling of pileup events is estimated by varying the cross  
1341 section of the minimum bias events by 5 % when generating the target pileup distri-  
1342 butions. The pileup weights are recomputed with these new distributions and applied  
1343 to the simulated events to obtain the variation in the yields in the inclusive signal  
1344 region. The average uncertainty is between 1 and 2 %. We treat these uncertainties  
1345 as 100 % correlated across the three years of data taking.

Table 3.18: Systematic uncertainties in the signal efficiency for all three years and the three channels. The mean is provided in cases where the uncertainty varies by signal sample. Uncertainties in the same row are treated as correlated among the years of data taking, except for the displaced tracking and muon pixel hit efficiencies, where the 2016 uncertainty is treated as uncorrelated with the 2017 and 2018 uncertainties.

Systematic uncertainty	2016	2017	2018
<i>Integrated luminosity</i>	1.8%	1.8%	1.8%
<i>Pileup</i>			
- $e\mu$ channel	0.5%	0.6%	0.5%
- $ee$ channel	0.5%	0.9%	0.8%
- $\mu\mu$ channel	0.2%	0.1%	0.2%
<i>Displaced tracking efficiency</i>	14%	5.8%	2.4%
<i>Trigger efficiency</i>			
- $e\mu$ channel, electrons	1.6%	1.3%	1.2%
- $e\mu$ channel, muons	1.6%	1.4%	1.2%
- $ee$ channel	10%	13%	19%
- $\mu\mu$ channel	1.2%	1.0%	1.1%
<i>Muon trigger efficiency at large <math> d_0 </math></i>			
- $e\mu$ channel, muons	20%	20%	20%
- $\mu\mu$ channel	20%	20%	20%
<i>Lepton identification and isolation</i>			
- $e\mu$ channel, electrons	1.2%	3.6%	3.5%
- $e\mu$ channel, muons	0.05%	0.07%	0.06%
- $ee$ channel	2.4%	7.2%	7.0%
- $\mu\mu$ channel	0.10%	0.14%	0.12%
<i>Muon pixel hit efficiency</i>			
- $e\mu$ channel, muons	32%	12%	16%
- $\mu\mu$ channel	73%	23%	30%
<i>Lepton <math> d_0 </math> correction</i>			
- $e\mu$ channel, electrons	—	0.001%	0.001%
- $e\mu$ channel, muons	—	0.003%	0.001%
- $ee$ channel	—	0.11%	0.11%
- $\mu\mu$ channel	—	0.11%	0.11%

1346 **3.6.3 Displaced tracking efficiency**

1347 The systematic uncertainty associated with the modeling of the displaced tracking  
1348 efficiency is derived from a dedicated study using cosmic ray muons. Following the  
1349 results of the study presented in Appendix C, we assign 14.1%, 5.8%, and 2.4%  
1350 systematic uncertainties in 2016, 2017, and 2018, respectively. Because the CMS pixel  
1351 detector was upgraded between 2016 and 2017 data taking, we treat the 2017 and  
1352 2018 systematic uncertainties as fully correlated and the 2016 systematic uncertainty  
1353 as uncorrelated with 2017 and 2018.

1354 **3.6.4 Trigger efficiency**

1355 The trigger efficiency systematic uncertainty is given by the uncertainty in the  
1356 measured trigger efficiency scale factors (see Section 3.4.4). These uncertainties are  
1357 1% or less for the  $e\mu$  and  $\mu\mu$  channels and about 10% for the  $ee$  channel. In addition,  
1358 we have studied the trigger efficiency in signal as a function of  $|d_0|$  for events in the  
1359 trigger  $p_T$  plateau. To cover the change observed in the muon trigger efficiency over  
1360 the full  $|d_0|$  range, we assign an additional 20% uncertainty.

1361 We treat the trigger efficiency uncertainties as 100% correlated across the three  
1362 years of data taking.

1363 **3.6.5 Lepton ID and isolation**

1364 To find the systematic uncertainty associated with the corrections to the lepton  
1365 ID and isolation, we fluctuate the lepton scale factors up and down by their uncer-  
1366 tainty and observe the change in the event yields in the inclusive signal region. The  
1367 average uncertainty for electrons is about 3% in the  $e\mu$  channel and about 7% in

1368 the  $ee$  channel, while the average uncertainty for muons is  $< 1\%$ . We treat these  
1369 uncertainties as 100 % correlated across the three years of data taking.

1370 **3.6.6 Muon pixel hit efficiency**

1371 The requirement in the muon ID that muons have at least one pixel hit could in  
1372 principle have some appreciable  $|d_0|$  dependence, so we perform a dedicated study  
1373 to ensure that we account for any differences in  $|d_0|$  dependence between data and  
1374 simulation. Figure 3.26 shows the efficiency of this requirement in cosmic simulation  
1375 and NoBPTX data (described in appendix C) as a function of muon  $|d_0|$ . For events  
1376 in the denominator of these plots, we require that at least 2 global, PF muons have  
1377  $|\eta| < 1.0$ ,  $p_T > 25 \text{ GeV}$ , no displaced vertices in the tracker material, longitudinal im-  
1378 pact parameter less than 15 cm, and pass all the tight ID criteria except the pixel hit  
1379 requirement. We also require the muons to be separated by  $\Delta R > 0.2$ . The events  
1380 in the numerator must pass the same requirements in addition to the requirement  
1381 that the muons have at least one pixel hit. From this plot, we calculate the mean  
1382 efficiency to identify the muons in the simulated signal events using the same proce-  
1383 dure as is used for the displaced tracking efficiency systematic uncertainty described  
1384 in Appendix C. We repeat the procedure in both cosmic simulation and in NoBPTX  
1385 data, and using the ratio of these two efficiencies, we derive the relative systematic  
1386 uncertainty in the signal. The average uncertainty is about 16 % (32 %) in the  $e\mu$   
1387 ( $\mu\mu$ ) channel. As the pixel detector was upgraded after 2016, the 2017 and 2018  
1388 systematic uncertainties are treated as fully correlated while the 2016 uncertainty is  
1389 treated as uncorrelated with the 2017 and 2018 uncertainties.

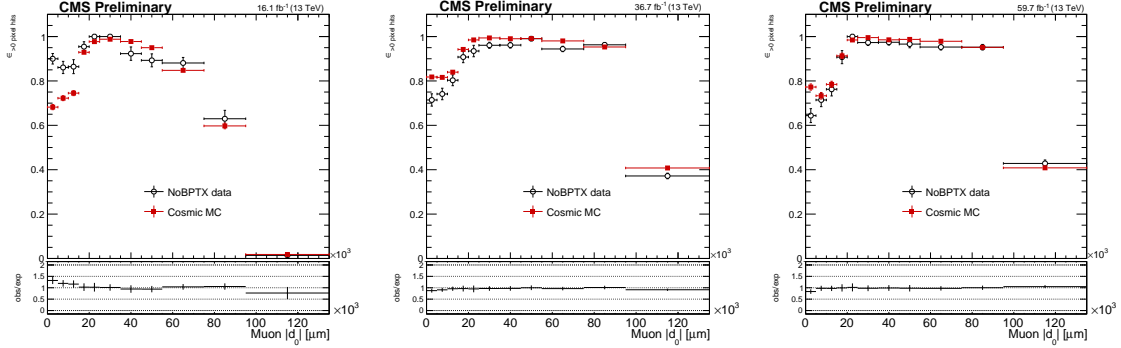


Figure 3.26: The pixel hit efficiency as a function of muon  $|d_0|$ , for cosmic simulation and NoBPTX data in 2016 (left), 2017 (middle), and 2018 (right) conditions.

### 1390 3.6.7 Lepton $d_0$ resolution

1391 To find the systematic uncertainty associated with the corrections to the lepton  
 1392  $d_0$  (see Section 3.4.3), we fluctuate the lepton  $d_0$  corrections up and down by their  
 1393 uncertainty and observe the change in the event yields in the inclusive signal region.  
 1394 The average uncertainty is  $< 1\%$ . We treat these uncertainties as 100 % correlated  
 1395 in 2017 and 2018. No  $d_0$  correction or systematic uncertainty is needed for 2016  
 1396 simulation.

1397 **3.7 Results**

1398 After unblinding and comparing the observed SR yields with the predicted back-  
1399 ground yields, we find no significant excess. Table 3.19 shows the predicted number  
1400 of background events and the observed yields in each SR, and Figs. 3.27 and 3.28  
1401 visually summarize this same information.

1402 **3.7.1 Observed events**

1403 In general, the observed SR events appear to be SM events from proton-proton  
1404 collisions. Specifically, we see no evidence of leptons from cosmic rays, material inter-  
1405 actions, or signal. Figure 3.29 shows two-dimensional  $|d_0|$  distributions of data events  
1406 that pass the preselection, and Fig. 3.30 shows the same but for data events in the  
1407 inclusive SR. As expected for SM background, the observed events are concentrated  
1408 in the low  $|d_0|$  region.

1409 We also use event display visualizations to examine each observed SR event indi-  
1410 vidually and record our observations below.

1411 In the  $e\mu$  channel, the SR events tend to have several jets and often have  $p_T^{\text{miss}} >$   
1412 100 GeV. Many events have muon  $\phi$  values such that the muon system hits are all  
1413 near the edges of detector sections or muon  $\eta$  values such that the muon is near the  
1414 barrel/endcap transition in the muon system. There are also a few events in which  
1415 the electron and/or muon are associated with a different primary vertex than their  
1416 associated track.

1417 In the  $ee$  channel, the majority of SR events contain at least one electron with  
1418  $|\eta| > 1.1$ , which increases the probability that their  $d_0$  is poorly measured. Across all  
1419 three years, most events fall into one of three categories:

Table 3.19: The number of estimated background and observed events in each channel and SR. For each estimate, the total uncertainty is given. The  $p_T$  boundaries that separate the low- and high- $p_T$  bins of SR I are listed in Table 3.9.

	SR I, low $p_T$ bin	SR I, high $p_T$ bin	SR II	SR III	SR IV
<i>2016 e<math>\mu</math></i>					
- estimated	$3.8^{+4.8}_{-3.8}$	$0.41^{+0.53}_{-0.41}$	$0.09^{+0.12}_{-0.09}$	$0.15 \pm 0.15$	$0.003^{+0.004}_{-0.003}$
- observed	8	1	0	0	0
<i>2017+2018 e<math>\mu</math></i>					
- estimated	$38 \pm 13$	$0.75^{+0.41}_{-0.34}$	$0.23^{+0.27}_{-0.23}$	$0.71^{+0.76}_{-0.71}$	$0.01^{+0.02}_{-0.01}$
- observed	28	3	0	1	0
<i>2016 ee</i>					
- estimated	$18 \pm 11$	$0.22^{+0.17}_{-0.16}$	$0.51^{+1.02}_{-0.51}$	$0.43^{+0.85}_{-0.43}$	$0.01^{+0.02}_{-0.01}$
- observed	40	0	0	1	0
<i>2017+2018 ee</i>					
- estimated	$62^{+18}_{-17}$	$0.85^{+0.33}_{-0.35}$	$2.8 \pm 1.1$	$3.6 \pm 1.4$	$0.24^{+0.10}_{-0.09}$
- observed	48	0	1	4	0
<i>2016 <math>\mu\mu</math></i>					
- estimated	$7.4 \pm 3.0$	$0.25 \pm 0.11$	$0.17 \pm 0.11$	$0.19 \pm 0.12$	$0.01 \pm 0.01$
- observed	15	0	0	1	0
<i>2017+2018 <math>\mu\mu</math></i>					
- estimated	$3.5 \pm 1.5$	$0.69 \pm 0.31$	$0.08^{+0.12}_{-0.08}$	$0.14^{+0.19}_{-0.14}$	$0.01^{+0.02}_{-0.01}$
- observed	1	1	1	1	0

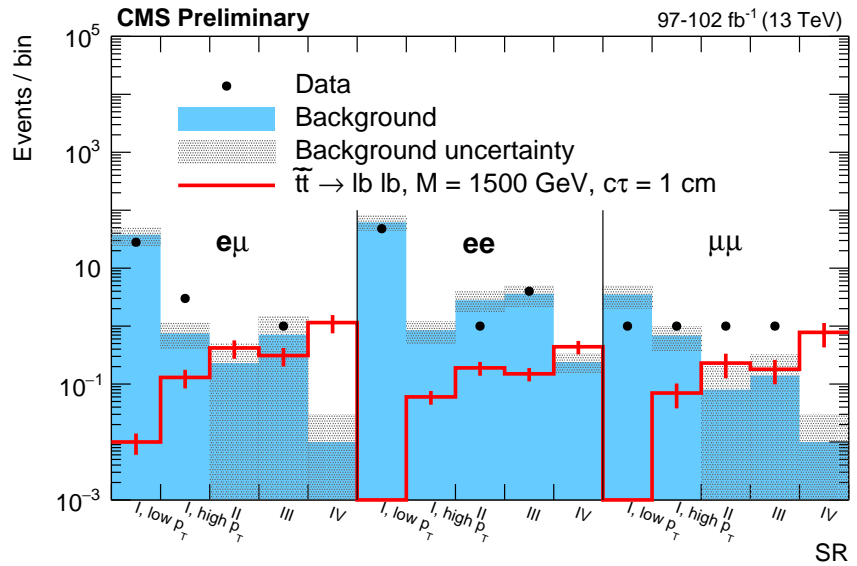
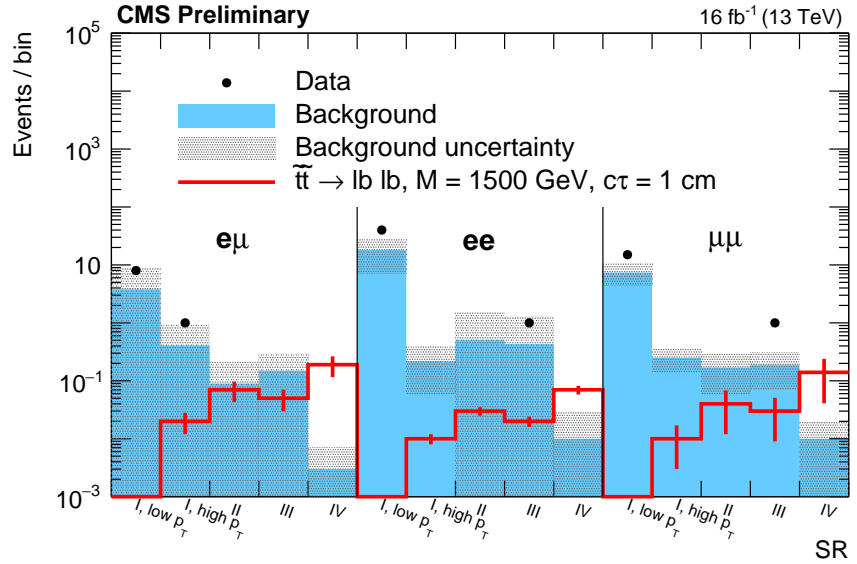


Figure 3.27: The number of estimated background and observed events in each channel and SR, with a representative signal overlaid, for 2016 (top) and 2017–2018 (bottom). For each background estimate and signal yield, the total uncertainty is given.

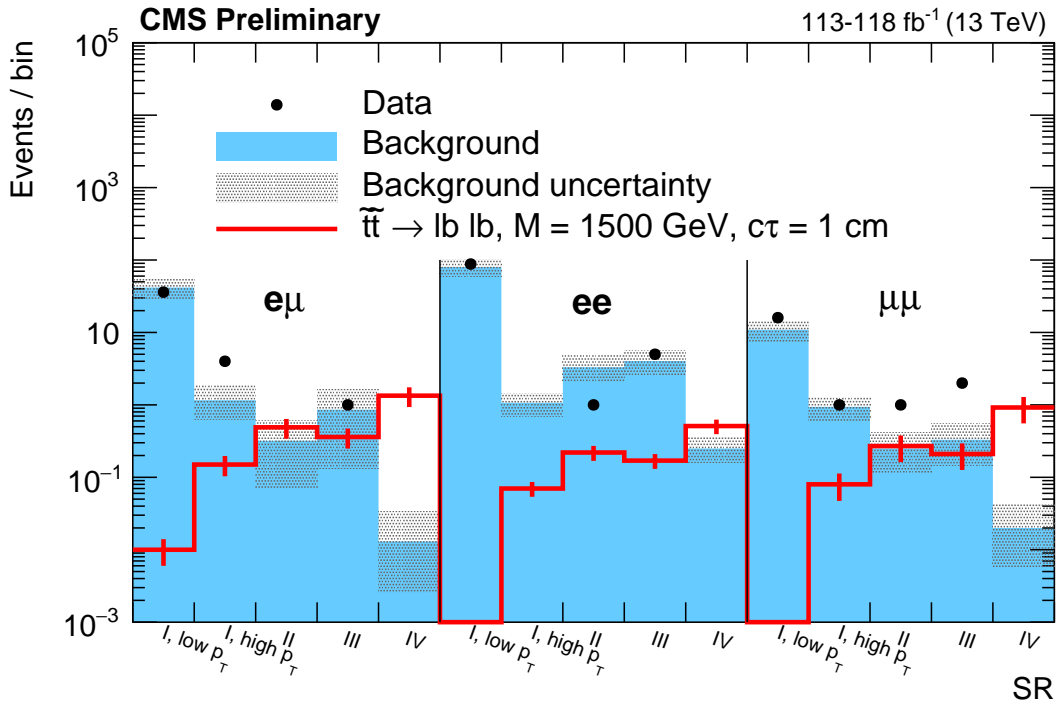


Figure 3.28: The number of estimated background and observed events in each channel and SR, with a representative signal overlaid, for 2016–2018. For each background estimate and signal yield, the total uncertainty is given.

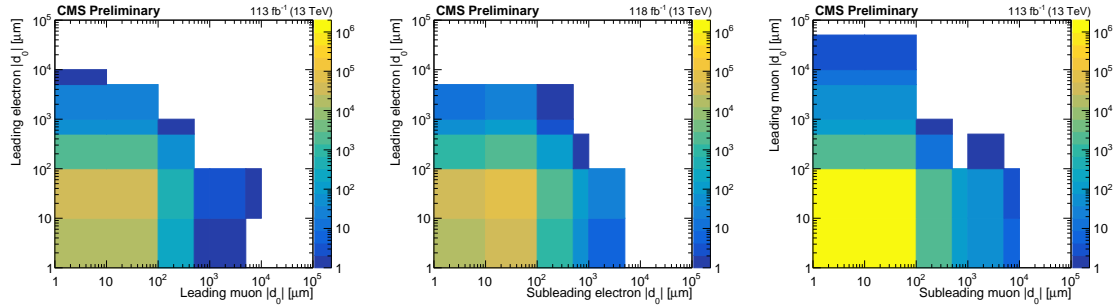


Figure 3.29: Two-dimensional distributions of  $|d_0^a|$  and  $|d_0^b|$ , for the events in data that pass the  $e\mu$  (left),  $ee$  (middle), and  $\mu\mu$  (right) preselection. The bins along the x and y axes contain underflow. The inclusive signal region covers the region between  $100 \mu\text{m}$  and  $10 \text{ cm}$  in each  $|d_0|$  variable shown.

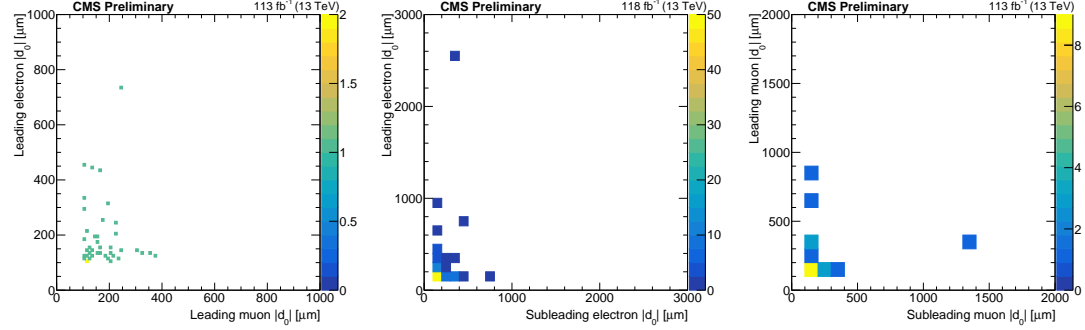


Figure 3.30: Two-dimensional distributions of  $|d_0^a|$  and  $|d_0^b|$ , for data events in the inclusive SR in the  $e\mu$  (left),  $ee$  (middle), and  $\mu\mu$  (right) channels.

- 1420     1. Events with two electrons that appear to be from a boosted  $Z$  boson, with an
- 1421       invariant mass between 80 and 100 GeV, opposite one or two jets
- 1422     2. Events with two electrons approximately back-to-back in  $\phi$  with an invariant
- 1423       mass greater than 100 GeV and  $p_T^{\text{miss}}$  usually between 10 and 40 GeV
- 1424     3. Events that are similar to type 2 but with at least one jet and frequently  $p_T^{\text{miss}}$
- 1425       between 70 and 110 GeV

1426       In the  $\mu\mu$  channel, many events have an invariant mass consistent with the mass  
 1427       of the  $Z$  boson and  $p_T^{\text{miss}}$  less than about 60 GeV. Most of the events found in 2017  
 1428       and 2018 have an invariant mass higher than than the  $Z$  boson mass and could be  $t\bar{t}$   
 1429       events. Eight of the sixteen SR events in 2016 have two muons with  $\phi$  values of about  
 1430        $\pm\pi/2$  (i.e. in the  $y$ - $z$  plane). Every muon pair in these eight events have an invariant  
 1431       mass consistent with a  $Z$  boson, and the  $\cos(\alpha)$  and  $\Delta t$  distributions of these muons  
 1432       confirm that they are not from cosmic rays. As shown in Fig. 3.31, these features are  
 1433       clearly visible in the  $\phi$  and di-muon invariant mass distributions of the SR data when  
 1434       compared with background simulation. Thirteen of the sixteen muons in these eight

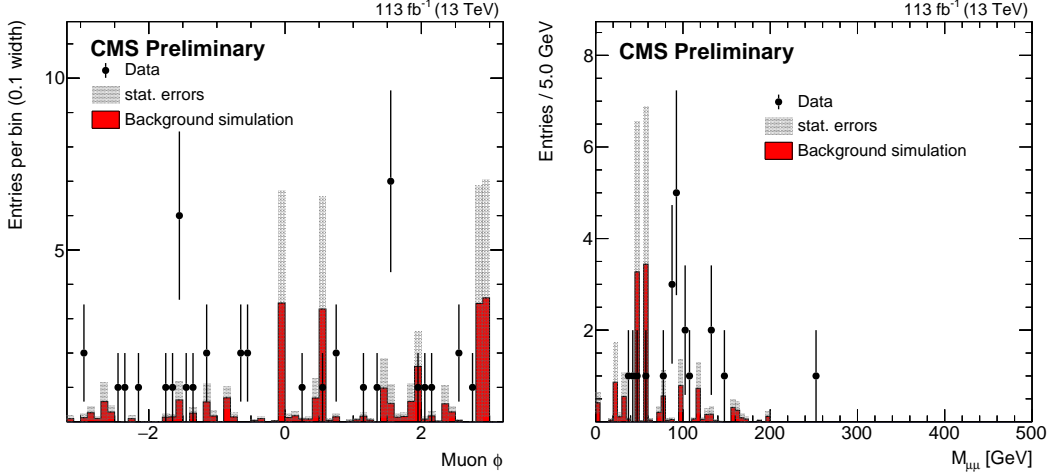


Figure 3.31: Muon  $\phi$  and di-muon invariant mass distributions for data and composite background simulation in the  $\mu\mu$  channel in the inclusive SR. The background simulation is normalized to the ABCD method background prediction.

1435 events have only one valid pixel hit, and event displays of these events show that the  
 1436 muon track often passes between or at the edge of pixel modules near the place where  
 1437 the two halves of the original pixel detector barrel are joined. We believe that this  
 1438 feature causes the muon  $d_0$  values to be poorly measured.

### 1439 3.7.2 Limits

1440 The data show no significant excess over background, so we set upper limits on the  
 1441 product of the signal production cross section ( $\sigma$ ) and branching fraction ( $\mathcal{B}$ ) using  
 1442 the HybridNew statistical method of the “Combine” tool developed by the CMS  
 1443 Higgs working group [75, 76, 77, 78]. The ABCD estimate is performed in Combine,  
 1444 which means that any signal contamination in the control regions is accounted for  
 1445 automatically. We perform a simultaneous counting experiment in each signal region

1446 bin. Figure 3.32 shows the 95% confidence level (CL) upper limits on the top squark  
1447 mass as a function of its lifetime.

1448 The variation in the size and shape of the exclusion regions between the three  
1449 channels is mostly explained by variation in signal yields between the three channels.  
1450 Looking at the high- $p_T$  bin of SR I, which is the most sensitive bin for top squarks with  
1451 large masses and small lifetimes, we find that the simulated signal yield is highest  
1452 in the  $e\mu$ . This difference between the  $e\mu$  and same-flavor channels is a result of  
1453 simple combinatorics: the two independent top squark decays will result in an  $e\mu$  final  
1454 state twice as often as an  $ee$  or  $\mu\mu$  final state. In this bin, the  $ee$ - and  $\mu\mu$ -channel  
1455 signal yields are similar. SR IV drives the sensitivity for top squarks with large  
1456 lifetimes. Because CMS identifies muons with higher efficiency than it does electrons,  
1457 the  $\mu\mu$  channel has the largest simulated signal yield in SR IV when considering top  
1458 squarks with lifetimes  $\gtrsim 10$  cm. For this same reason, the  $ee$  channel has the smallest  
1459 signal yield out of the three channels in SR IV when considering top squark lifetimes  
1460  $\gtrsim 10$  cm. Taking all of these effects together, we find that the  $e\mu$  channel is the most  
1461 sensitive for lifetimes  $\lesssim 10$  cm while the  $\mu\mu$  channel is the most sensitive for lifetimes  
1462  $\gtrsim 10$  cm.

1463 Figure 3.33 shows the 95% CL upper limits for the combination of the three  
1464 channels. The top squark limits assume  $\mathcal{B}(\tilde{t} \rightarrow bl) = \mathcal{B}(\tilde{t} \rightarrow dl) = 100\%$ , and each  $l$   
1465 has an equal probability of being an electron, a muon, or a tau lepton.

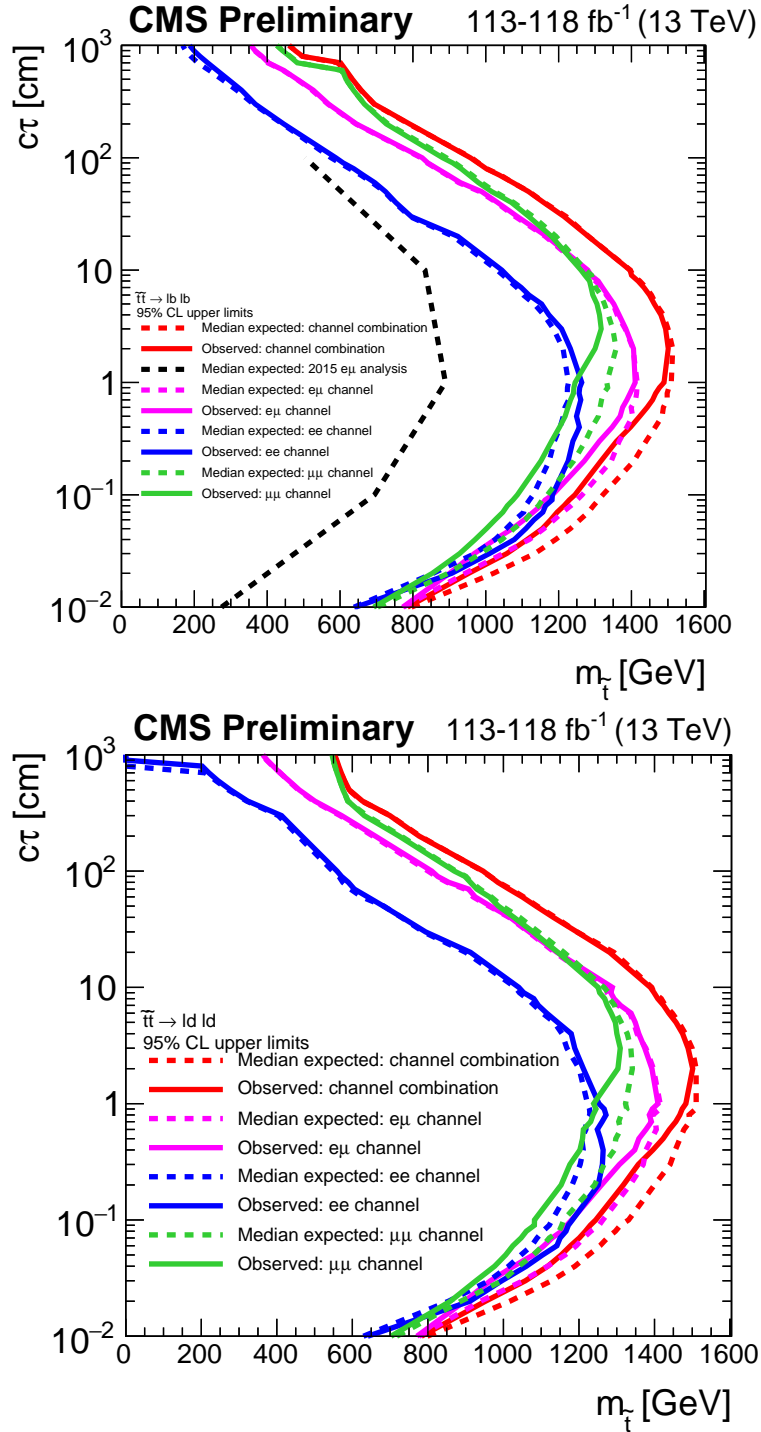


Figure 3.32: The 95% CL upper limits on the long-lived particle mass ( $m_{\tilde{t}}$ ) as a function of its lifetime ( $c\tau$ ), for the  $e\mu$ ,  $ee$ , and  $\mu\mu$  channels. The  $\tilde{t}\tilde{t} \rightarrow \bar{l}b\bar{l}b$  (top) and  $\tilde{t}\tilde{t} \rightarrow \bar{l}d\bar{l}d$  (bottom) processes are shown.

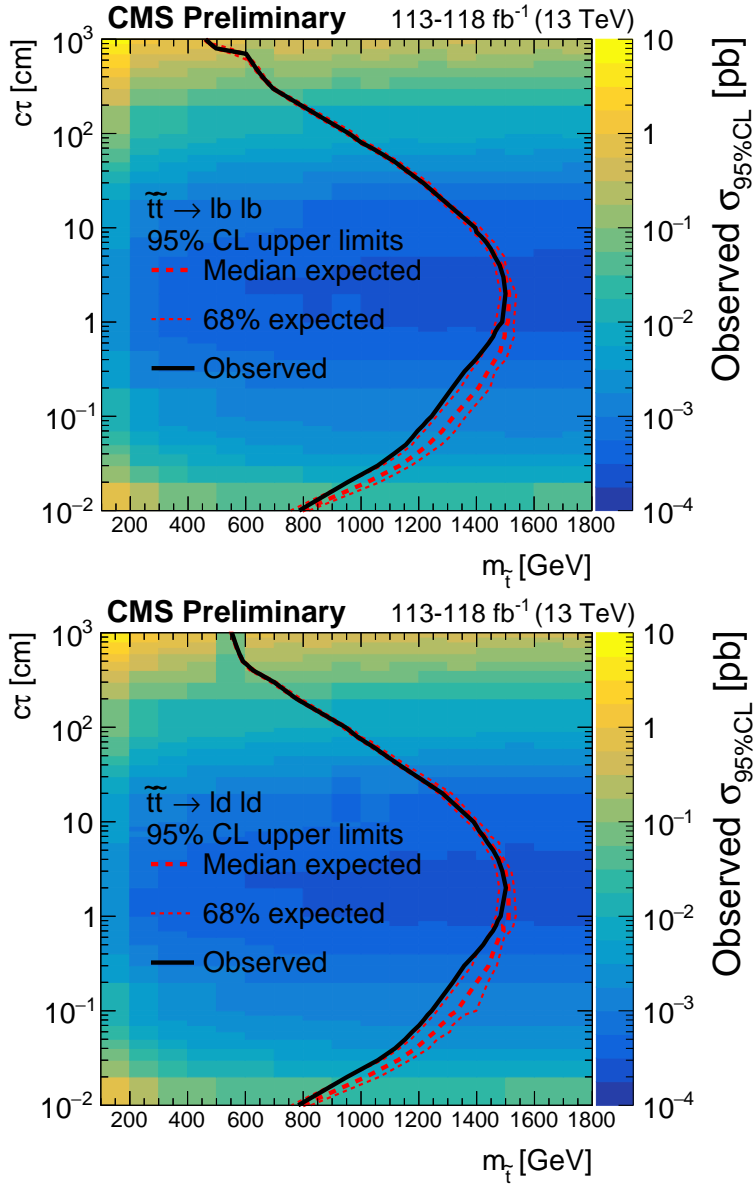


Figure 3.33: The 95% CL upper limits on the long-lived particle mass ( $m_{\tilde{t}}$ ) as a function of its lifetime ( $c\tau$ ). The colors indicate the observed 95% CL upper limit on the cross section. The  $\tilde{t} \bar{t} \rightarrow l b \bar{l} b$  (left) and  $\tilde{t} \bar{t} \rightarrow l d \bar{l} \bar{d}$  (right) processes are shown.

1466 **3.7.3 Additional likelihood tests**

1467 We also perform several statistical tests to help assess the significance of the  
1468 differences between the observed and predicted SR yields and to ensure that the  
1469 likelihood is handling the observed yields in a reasonable way.

1470 We first compare the best-fit background yields under the background-only hy-  
1471 pothesis while masking the signal regions with the best-fit background yields under  
1472 the signal+background hypothesis using the full information from all signal and con-  
1473 trol regions. For simplicity, we refer to the first quantity as the pre-fit prediction and  
1474 the second as the post-fit prediction. Table 3.20 lists the pre- and post-fit predictions  
1475 for each channel and SR, and Fig. 3.34 (left) shows associated pull distribution. We  
1476 find that the differences between the pre- and post-fit predictions are consistent with  
1477 the variation one would expect from purely statistical effects.

1478 Next, we examine the equivalent pull distribution for background yield nuisance  
1479 parameters. Figure 3.34 (right) shows that the differences in nuisance parameter  
1480 values before and after the fit are also consistent with the variation one would expect  
1481 from purely statistical effects.

1482 Finally, we check the observed asymptotic significance of the  $t\bar{t} \rightarrow \tilde{l}b \bar{l}\bar{b}$  signal  
1483 model. As shown in Fig. 3.35, the observed significance is less than two for all signal  
1484 points we consider when looking at the combination of all channels as well as each  
1485 channel individually. We therefore conclude that the observed yields do not constitute  
1486 a significant excess.

Table 3.20: The pre- and post-fit predictions for each signal region bin.

	SR I, low $p_T$ bin	SR I, high $p_T$ bin	SR II	SR III	SR IV
<i>2016 e<math>\mu</math></i>					
- pre-fit	$3.8 \pm 3.9$	$0.40 \pm 0.45$	$0.09 \pm 0.11$	$0.15 \pm 0.13$	$0.003 \pm 0.003$
- post-fit	$7.1 \pm 2.0$	$0.76 \pm 0.31$	$0.08 \pm 0.08$	$0.14 \pm 0.14$	$0.003 \pm 0.003$
<i>2017+2018 e<math>\mu</math></i>					
- pre-fit	$38 \pm 14$	$0.75 \pm 0.40$	$0.23 \pm 0.37$	$0.71 \pm 0.90$	$0.01 \pm 0.02$
- post-fit	$31 \pm 5$	$0.68 \pm 0.25$	$0.20 \pm 0.17$	$0.65 \pm 0.48$	$0.01 \pm 0.01$
<i>2016 ee</i>					
- pre-fit	$18 \pm 11$	$0.22 \pm 0.17$	$0.51 \pm 2.41$	$0.43 \pm 2.06$	$0.01 \pm 0.06$
- post-fit	$35 \pm 5$	$0.40 \pm 0.14$	$0.50 \pm 0.75$	$0.44 \pm 0.53$	$0.01 \pm 0.02$
<i>2017+2018 ee</i>					
- pre-fit	$62 \pm 17$	$0.85 \pm 0.31$	$2.8 \pm 0.9$	$3.6 \pm 1.2$	$0.25 \pm 0.09$
- post-fit	$50 \pm 6$	$0.65 \pm 0.19$	$2.5 \pm 0.7$	$3.2 \pm 0.9$	$0.22 \pm 0.06$
<i>2016 <math>\mu\mu</math></i>					
- pre-fit	$7.4 \pm 3.3$	$0.25 \pm 0.11$	$0.17 \pm 0.11$	$0.19 \pm 0.12$	$0.01 \pm 0.01$
- post-fit	$11 \pm 2$	$0.37 \pm 0.10$	$0.19 \pm 0.10$	$0.21 \pm 0.12$	$0.01 \pm 0.01$
<i>2017+2018 <math>\mu\mu</math></i>					
- pre-fit	$3.4 \pm 1.6$	$0.69 \pm 0.32$	$0.08 \pm 0.12$	$0.14 \pm 0.18$	$0.01 \pm 0.02$
- post-fit	$2.5 \pm 1.1$	$0.51 \pm 0.22$	$0.14 \pm 0.36$	$0.23 \pm 0.63$	$0.02 \pm 0.05$

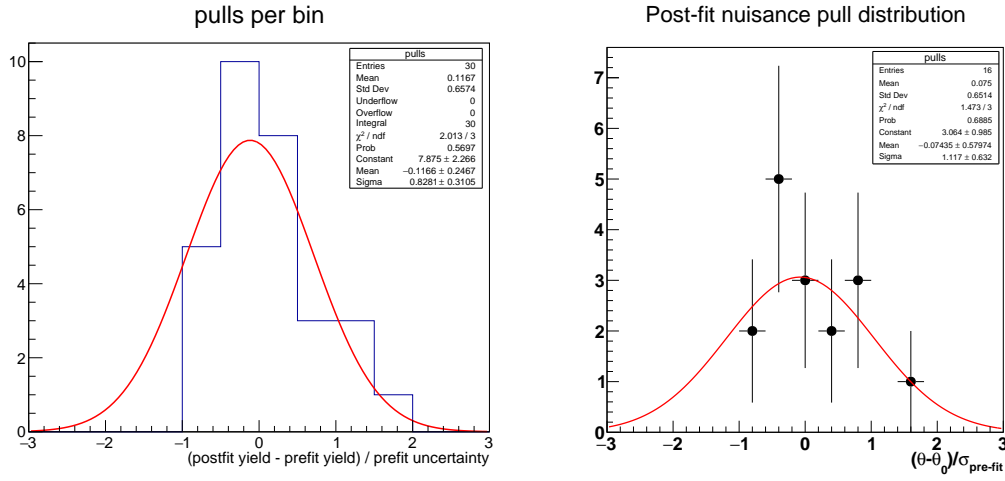


Figure 3.34: The distribution of pulls for each signal region bin, where pulls are calculated as the difference between the post-fit background yield and the pre-fit background yield divided by the pre-fit background uncertainty (left). The distribution of pulls for each background nuisance parameter, where pulls are calculated as the difference between the post-fit value and the pre-fit value divided by the pre-fit uncertainty (right).

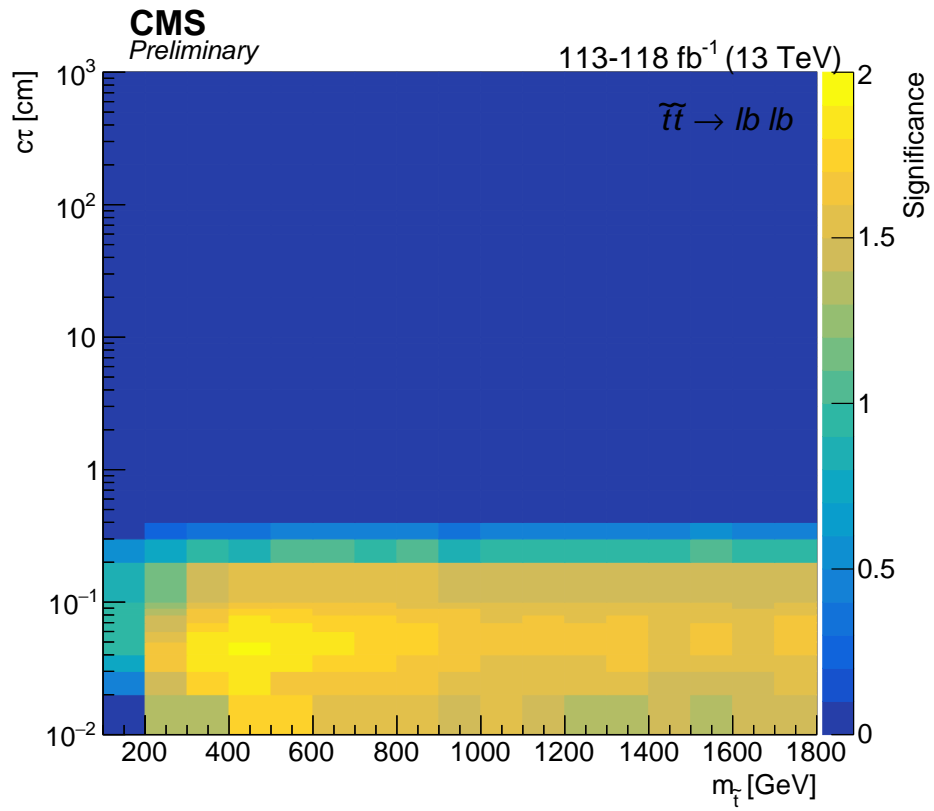


Figure 3.35: The observed asymptotic significances for the  $\tilde{t}\tilde{t} \rightarrow \bar{l}b\bar{l}b$  process as a function of  $\tilde{t}$  mass and lifetime using the combined results.

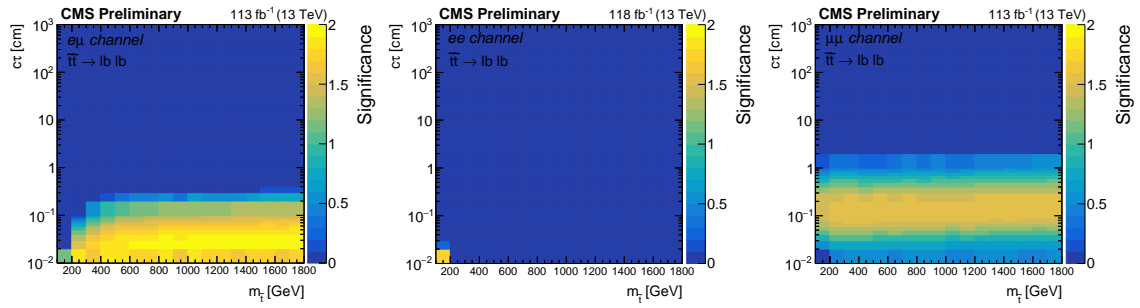


Figure 3.36: The observed asymptotic significances for the  $\tilde{t}\tilde{t} \rightarrow \bar{l}b\bar{l}b$  process as a function of  $\tilde{t}$  mass and lifetime in the  $ee$  (left),  $e\mu$  (center),  $\mu\mu$  channels (right).

## Chapter 4: Conclusion

1488 A search has been presented for new long-lived particles that propagate a mea-  
1489 surable distance before decaying to leptons inside the CMS detector. The resulting  
1490 displaced lepton signature is targeted by selecting events with two leptons (an electron  
1491 and a muon, two electrons, or two muons) whose transverse impact parameters are  
1492 between 0.01 and 10 cm. The search is performed in  $113\text{--}118 \text{ fb}^{-1}$  of proton-proton  
1493 collision data produced by the CERN LHC at a center-of-mass energy of 13 TeV and  
1494 collected by the CMS detector in 2016, 2017, and 2018. This analysis is the first  
1495 at CMS to target pairs of displaced electrons or muons without requiring that they  
1496 form a common vertex. The observation is consistent with the background-only hy-  
1497 pothesis, and limits are set on the product of the cross-section of top squark pair  
1498 production and the branching fraction to a lepton and a b or d quark through an  
1499 R-parity-violating vertex. For a proper decay length hypothesis of 2 cm, top squarks  
1500 with masses up 1500 GeV are excluded at the 95 % confidence level.

1501 Looking to the future, there are several opportunities to increase the sensitivity to  
1502 new long-lived particles that decay to leptons. Aside from the incremental improve-  
1503 ments offered by the expected increases in integrated luminosity and center-of-mass  
1504 energy provided by the LHC (14 TeV proton-proton collisions may be available as

1505 soon as 2022 [79, 80]), there are a few changes to the analysis strategy that may be  
1506 worth pursuing.

1507 The most straightforward improvement would be to study the electron and muon  
1508 identification requirements with an eye to improving the signal efficiency, especially  
1509 at large  $|d_0|$ . In particular, the missing inner hit and pixel hit requirements applied  
1510 to electrons and muons, respectively, in the current analysis effectively limit the max-  
1511 imum LLP decay length to the radius of the CMS pixel detector, which is 16 cm.  
1512 Any gains in signal efficiency would of course have to be balanced against the likely  
1513 increase in the mismeasurement background. Thinking along similar lines, it may be  
1514 interesting to investigate the effects of relaxing the lepton isolation requirement.

1515 A more challenging angle would be to explicitly consider tau leptons in the final  
1516 state. The analysis presented here is sensitive to displaced taus that decay leptonically  
1517 to electrons and muons, but a future analysis could likely expand this sensitivity by  
1518 explicitly studying the  $|d_0|$  behavior of displaced taus. Given the tau decay branching  
1519 fractions [31], the largest gain would likely come from considering hadronic tau decays,  
1520 though this route would also likely represent a considerable challenge.

1521 Finally, one could perform an analysis similar to the one presented here but specif-  
1522 ically target new low-mass long-lived particles. The lepton  $p_T$  requirements imposed  
1523 by the trigger limit the low-mass sensitivity of the current analysis. One possible  
1524 approach would be to adopt a different triggering strategy in the next data-taking  
1525 period, but it may be that CMS has already collected the ideal dataset in which to  
1526 perform such a search. In 2018, CMS debuted a novel trigger strategy in which spe-  
1527 cialized triggers collected approximately ten billion unbiased b-hadron-decay events  
1528 [81]. The triggers use a tag-and-probe strategy that actually require the presence of

1529 at least one displaced muon whose  $p_T$  can be as low as 7 GeV. The trade-off is that  
1530 most of the muons will be embedded in b-jets, which will likely necessitate changes to  
1531 the analysis strategy. Such a search could be an interesting way to cover new ground  
1532 with existing data.

1533 Searches for BSM LLPs are critical to exploring the available new-physics param-  
1534 eter space and ultimately to understanding whether new physics exists at currently  
1535 accessible energy scales. The analysis presented here explicitly constrains the natural  
1536 parameter space of RPV SUSY models, but more importantly, it also constrains any  
1537 not-yet-imagined new physics scenarios that could produce displaced leptons. There  
1538 are still many stones unturned, and the analysis presented in this thesis shines a light  
1539 on one more region of this unexplored space.

## Appendix A: Impact of APV25 saturation on displaced tracking

1542 A portion of the data collected by the CMS detector in 2016 is affected by the  
1543 APV saturation effect described in [82]. The APV25 saturation effect is a byproduct  
1544 of the production of heavily ionising particles (HIPs) in inelastic interactions between  
1545 hadrons and the nuclei of silicon sensors. The energy deposits of HIPs can be up to  
1546 1000 times greater than those of typical particles produced in LHC collisions. These  
1547 large energy deposits can saturate the analog readout of the APV25 chips [83] that are  
1548 used to read out the CMS silicon strip tracker, which is described in Section 2.2.2. Due  
1549 to a feature of the APV25 powering scheme that normally helps stabilize the pulse-  
1550 height baseline, a single saturated channel can inadvertently suppress the outputs of  
1551 the 127 other APV25 channels for hundreds of nanoseconds.

Only around one in every 1000 incident hadrons will result in saturating HIP events, so the effect is only significant at high instantaneous luminosities. In 2016, the instantaneous luminosity increased to greater than the original LHC design goal, and the effect began influencing detector performance. Starting in run 278802, the tracker front-end electronics were reconfigured to substantially reduce their sensitivity to the APV25 saturation effect.

1558        The deadtime associated with the a saturating HIP event can cause some tracker  
1559        hits to be lost. This effect can lead to reduced tracking efficiency, and it is reasonable  
1560        to suspect that the lose of efficiency may be more significant for displaced particles  
1561        that may have fewer tracker hits to begin with. To investigate the impact on displaced  
1562        tracking, one of our collaborators, Ian Tomalin, performed a study with  $K_S^0 \rightarrow \pi^+\pi^-$   
1563        decays. From this study, we conclude that only data taken after the APV25 saturation  
1564        effect was mitigated should be used in the Displaced Leptons analysis. We therefore  
1565        use only eras G and H in 2016 and all available data from 2017 and 2018.

1566        Using data collected in 2016, 2017, and 2018 with the `HLT_ZeroBias` trigger, the  
1567        reconstructed  $K_S^0$  candidate decay lengths are compared among several different runs  
1568        that correspond to a wide range of instantaneous luminosities and data-taking periods.  
1569        The  $K_S^0$  candidates used come from the `generalV0Candidates:Kshort` collection.  
1570        Each candidate must have a pair of oppositely charged tracks consistent with the  $K_S^0$   
1571        mass and coming from a common vertex that is at least 2 cm from the beam line.  
1572        The tracks are required to have at least one pixel hit and  $|\eta| < 2$ . In 2016 (2017-18),  
1573        the tracks are required to have  $p_T > 0.7$  GeV (1.5 GeV).

1574        Figure A.1 shows the reconstructed transverse decay length of the  $K_S^0$  candidates  
1575        for data from all three years. Each distribution is normalized to the integrated lumi-  
1576        nosity of the run from which it is taken. In the 2016 plot, the solid (dashed) lines  
1577        correspond to runs taken before (after) the APV25 saturation effect was mitigated.  
1578        In the pre-mitigation runs, the  $K_S^0$  transverse decay length distribution falls rapidly  
1579        with increasing instantaneous luminosity, but the dependence on instantaneous lumi-  
1580        nosity is significantly reduced in the post-mitigation runs and in all 2017 and 2018

1581 runs. The narrower transverse decay length at higher luminosity in the 2016 pre-  
1582 mitigation runs is interpreted as an instantaneous-luminosity-dependent decrease in  
1583 tracking efficiency.

1584 Given the size of this effect, we decide not to use 2016 data taken before run  
1585 278802 in the Displaced Leptons search. The instantaneous-luminosity-dependent  
1586 displaced tracking efficiency would be difficult to quantify, which would lead to large  
1587 systematic uncertainties. Furthermore, the signal yield would be suppressed by the  
1588 lower displaced tracking efficiency. Finally, studies of displaced tracking efficiency  
1589 with cosmic ray data are insensitive to the APV25 saturation effect because the  
1590 instantaneous luminosity during dedicated cosmic runs is zero.

1591 A small dependence on instantaneous luminosity is also apparent in the 2017  
1592 and 2018 distributions shown in Fig. A.1. The runs with the lowest (highest) in-  
1593 stantaneous luminosity examined in each data taking period are shown with dashed  
1594 (solid) lines. This may be due to a residual APV saturation effect or possibly another  
1595 luminosity-related tracker inefficiency. We do not find it necessary to take any special  
1596 measures to account for this small effect in 2017 and 2018.

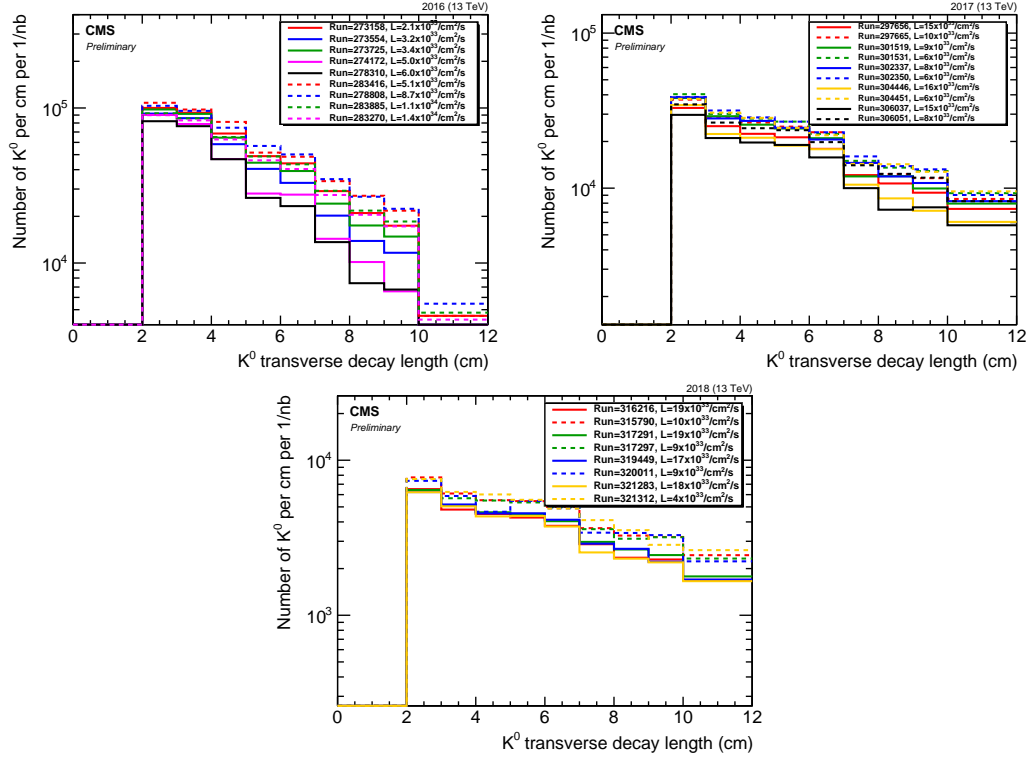


Figure A.1: Transverse decay length distribution of reconstructed  $K_0^0 \rightarrow \pi^+\pi^-$  candidates for various runs in 2016 (top left), 2017 (top right) and 2018 (bottom). The peak instantaneous luminosity of each run is indicated in the legend, and each distribution is normalized to the integrated luminosity of the run. In the 2016 plot, runs taken before (after) the APV25 saturation effect was mitigated are shown by solid (dashed) lines. In the 2017 plot, the run with lowest (highest) instantaneous luminosity examined in each data taking era is plotted with a dashed (solid) line. Towards the end of 2017 (orange and black lines) the LHC ran with approximately 20% fewer proton bunches, meaning that the instantaneous luminosity per bunch crossing was higher than one might naively expect from the instantaneous luminosities shown in the legend.

1597

## Appendix B: Poorly measured lepton $|d_0|$ at large $|\eta|$

1598

We require muons to have  $|\eta| < 1.5$  due to the observed increase in width of the muon  $d_0$  distribution at large  $|\eta|$  in DY simulation with  $Z \rightarrow \tau\tau \rightarrow ll$  events removed (see Fig. B.1 (left)). The width visibly increases at large  $|\eta|$  in all three years but is less pronounced in 2017 and 2018 due to the improved performance of the Phase 1 pixel detector. The upgraded pixel detector is also responsible for the overall difference in  $d_0$  width between years. Requiring muon  $|\eta| < 1.5$  has two effects: (1) it dramatically reduces the mismeasurement background in 2016 data in the  $\mu\mu$  channel, and (2) it removes a possible source of  $|d_0^a| - |d_0^b|$  correlation in which the correlation between muons in  $\eta$  leads to correlation between muons in  $|d_0|$ . As shown in Fig. B.1 (right), muons from  $\tilde{t}\tilde{t} \rightarrow \bar{l}b l\bar{b}$  events tend to have small  $|\eta|$ , so requiring muon  $|\eta| < 1.5$  has a minimal effect on the signal acceptance.

1609

Electron  $d_0$  resolution also worsens at large  $|\eta|$ . Furthermore, Fig. B.2 (left) shows that electrons from SM mesons are particularly concentrated  $|\eta| > 1.5$ . As in the muon case, electrons from  $\tilde{t}\tilde{t} \rightarrow \bar{l}b l\bar{b}$  events tend to have  $|\eta| < 1.5$  (see Fig. B.2), which implies that requiring electron  $|\eta| < 1.5$  will reduce the mismeasurement and SM meson backgrounds without significantly reducing signal acceptance.

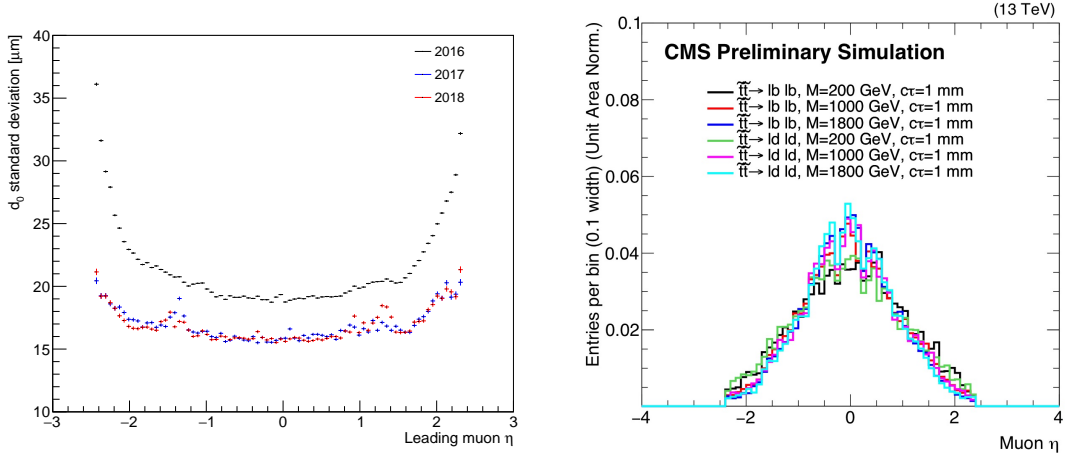


Figure B.1: The standard deviation of the leading muon  $d_0$  as a function of the leading muon  $\eta$  for simulated background events (left). To ensure that the variation in width is purely due to  $d_0$  resolution effects, we use a sample of simulated Drell-Yan events from which the  $Z \rightarrow \tau\tau \rightarrow ll$  events have been removed. Muon  $\eta$  distribution for simulated  $\tilde{t}\tilde{t} \rightarrow l\bar{b} l\bar{b}$  events (right). The  $\mu\mu$  preselection with a loosened  $|\eta|$  requirement is applied in both plots.

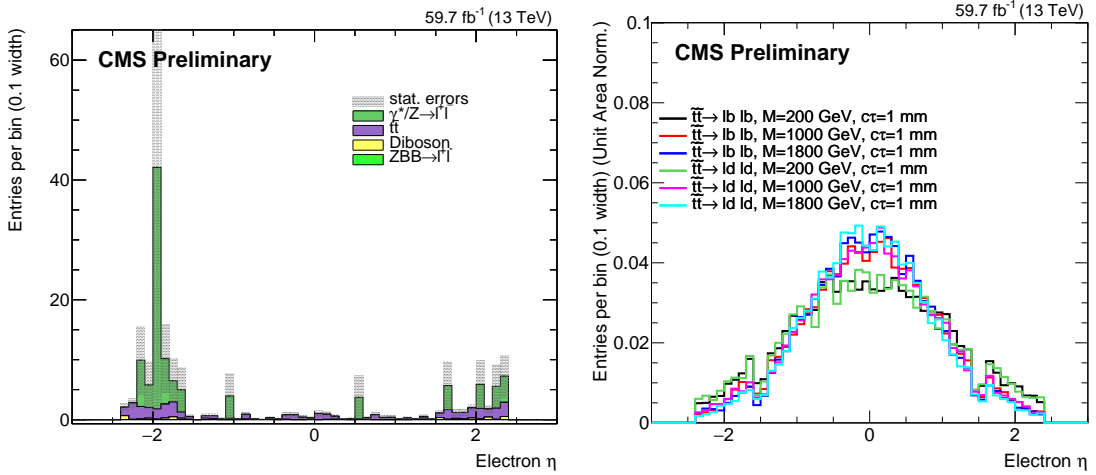


Figure B.2: Electron  $\eta$  distribution for simulated background events in which the electron parent particles are required to be SM mesons (left). Electron  $\eta$  distribution for simulated  $\tilde{t}\tilde{t} \rightarrow l\bar{b} l\bar{b}$  events (right). The  $e\mu$  preselection with a loosened  $\eta$  requirement is applied in both plots.

## Appendix C: Displaced tracking efficiency

1615 To measure the efficiency to reconstruct displaced, isolated, high- $p_T$  muons, our  
1616 collaborator Ian Tomalin performed a study with cosmic rays. The basic idea is to ap-  
1617 proximate the displaced tracking efficiency in data and simulation from the fraction of  
1618 cosmic ray muons reconstructed in the muon system that have a corresponding track  
1619 in the tracker. The results of this study are used to assign a systematic uncertainty  
1620 in the signal efficiency (see Section 3.6) and define the upper bound of 10 cm on the  
1621 inclusive signal region (see Section 3.3).

1622 First, the cosmic ray dataset is chosen. CMS collects cosmic ray data in two types  
1623 of runs: (1) dedicated cosmic runs in which cosmic ray muons are reconstructed  
1624 with dedicated reconstruction algorithms and (2) parasitic cosmic runs in which the  
1625 triggers veto bunch-crossing events to collect cosmic ray data in otherwise normal  
1626 proton-proton running conditions. In the parasitic cosmic runs, the cosmic ray muons  
1627 are reconstructed with the standard reconstruction algorithms as well as some dedi-  
1628 cated reconstruction algorithms. These two types of runs are then collected into two  
1629 datasets: (1) `Cosmics`, which contains only the dedicated cosmic runs and (2) `NoBPTX`,  
1630 which contains both the dedicated and parasitic cosmic runs. In each case, the strip  
1631 tracker electronics operate in the same mode used for proton-proton collisions. The

1632 NoBPTX datasets are used in this study because they include the same reconstruction  
1633 algorithms as used in the Displaced Leptons analysis.

1634 Events are collected with the `HLTL2Mu10NoVertexNoBPTX3BXv*` trigger, which ve-  
1635 toes events with proton-proton collisions and requires that a muon with  $p_T > 10 \text{ GeV}$   
1636 is reconstructed in the muon system. As in the Displaced Leptons analysis, the trigger  
1637 does not explicitly constrain the muon transverse or longitudinal impact parameter.  
1638 Following the study presented in appendix A, only eras G and H are used in 2016.  
1639 Following the procedure outlined in [84], the set of data-taking periods with reli-  
1640 able detector performance is identified with particular attention paid to the following  
1641 properties: (1) suitable cosmic trigger timing configuration, (2) data quality assessed  
1642 from reconstructed (as opposed to trigger-level) quantities, (3) trigger, tracker, muon  
1643 system, and track reconstruction known to be functioning well, and (4) magnetic field  
1644 value in normal range.

1645 To compare the displaced tracking efficiency between data and simulation, simu-  
1646 lated cosmic ray events are produced using the CMSGEN generator. The simulated  
1647 cosmic ray muons have  $p_T > 20 \text{ GeV}$ , transverse (longitudinal) impact parameter less  
1648 than 40 cm (80 cm), and arrive within a 30 ns window centered on the time at which  
1649 tracker readout efficiency is greatest. The detector response is modeled with GEANT  
1650 [85].

1651 In both data and simulated events, cosmic rays are reconstructed in the tracker  
1652 using the same track reconstruction algorithm that is used during proton-proton  
1653 collisions. This algorithm assumes particles propagate outwards from the center of  
1654 the detector, so cosmic ray muons are typically reconstructed as two tracks: one  
1655 moving upward and one moving downwards. In the muon system, cosmic ray muons

1656 are reconstructed with two dedicated algorithms. The first is a two-leg algorithm  
1657 that reconstructs each cosmic ray muon as two separate muons, one in the top half of  
1658 CMS and the other in the bottom. The second is a one-leg algorithm that reconstructs  
1659 cosmic rays as a single muon that traverses the entire detector. The longer lever arm  
1660 provided by the one-leg algorithm generally results in more accurate measurements  
1661 of the muon curvature in the magnetic field.

1662 A preliminary event selection is then applied to the data and simulation. The  
1663 events are required to have one one-leg muon with  $p_T > 20 \text{ GeV}$  and at least 50 hits  
1664 in the muon system. While the  $p_T$  requirement of the muons selected in this study  
1665 is lower than the Displaced Leptons muon  $p_T$  requirement, the tracking efficiency  
1666 does not depend significantly on  $p_T$  in the relevant range. The one-leg muon is also  
1667 required to be within 0.3 rad of two two-leg muons in  $\phi$  in order to reject cosmic ray  
1668 muon candidates that do not traverse the entire detector.

1669 The tracking efficiency is inferred from the fraction of selected one-leg muons that  
1670 are associated with a tracker track that has  $p_T > 15 \text{ GeV}$  and is within 0.2 rad in  $\phi$  of  
1671 the selected one-leg muon. To mimic the Displaced Leptons event selection, tracker  
1672 tracks are also required to have at least one pixel hit. Because each cosmic ray muon  
1673 generally results in two tracker tracks, two separate efficiencies are measured. These  
1674 efficiencies are referred to as "upward" and "downward" according to the direction of  
1675 the relevant tracker track. The downward efficiency is expected to be more reliable  
1676 because the tracker readout electronics assume that particles propagate outward from  
1677 the center of the detector. The upward and downward efficiencies measured in this  
1678 study agree within a few percent, but the downward efficiencies are used for the  
1679 definitive measurement.

Table C.1: Cosmic ray muon arrival time requirements used when measuring displaced tracking efficiency in data and simulation.

	2016–2017	2018
Data	$-13 \text{ ns} < t_{\mu\text{on}} < -7 \text{ ns}$	$-8 \text{ ns} < t_{\mu\text{on}} < -2 \text{ ns}$
Simulation	$-38 \text{ ns} < t_{\mu\text{on}} < -32 \text{ ns}$	$-40 \text{ ns} < t_{\mu\text{on}} < -34 \text{ ns}$

1680        The muon system also measures the cosmic ray muon arrival time. The average  
 1681      of the two two-leg muon arrival times provides the most precise measurement of the  
 1682      cosmic ray muon arrival time. This approach provides a time resolution on the order  
 1683      of 5 ns, whereas the time resolution provided by one-leg muons can be an order of  
 1684      magnitude greater.

1685        The selected one-leg muons with transverse (longitudinal) impact parameter less  
 1686      than 8 cm (20 cm) are used to study the tracking efficiency dependence on cosmic  
 1687      ray muon arrival time. Figure C.1 shows the distribution of the measured arrival  
 1688      time while Fig. C.2 shows the measured downward tracking efficiency as a function of  
 1689      measured arrival time. The disagreement between data and simulation in measured  
 1690      arrival time is simply an artifact of the specified simulation time window. Despite  
 1691      this offset, the efficiency shows a clear peak with a width of approximately 15 ns  
 1692      in both data and simulation. Based on the results of Fig. C.2, muons used in the  
 1693      downward tracking efficiency measurement must also pass the requirements listed in  
 1694      Table C.1. Using the upward efficiency produces similar results that are shifted by  
 1695      approximately 5 ns. The same sample of one-leg muons is also used to measure the  
 1696      downward tracking efficiency as a function of run number. No meaningful dependence  
 1697      is identified.

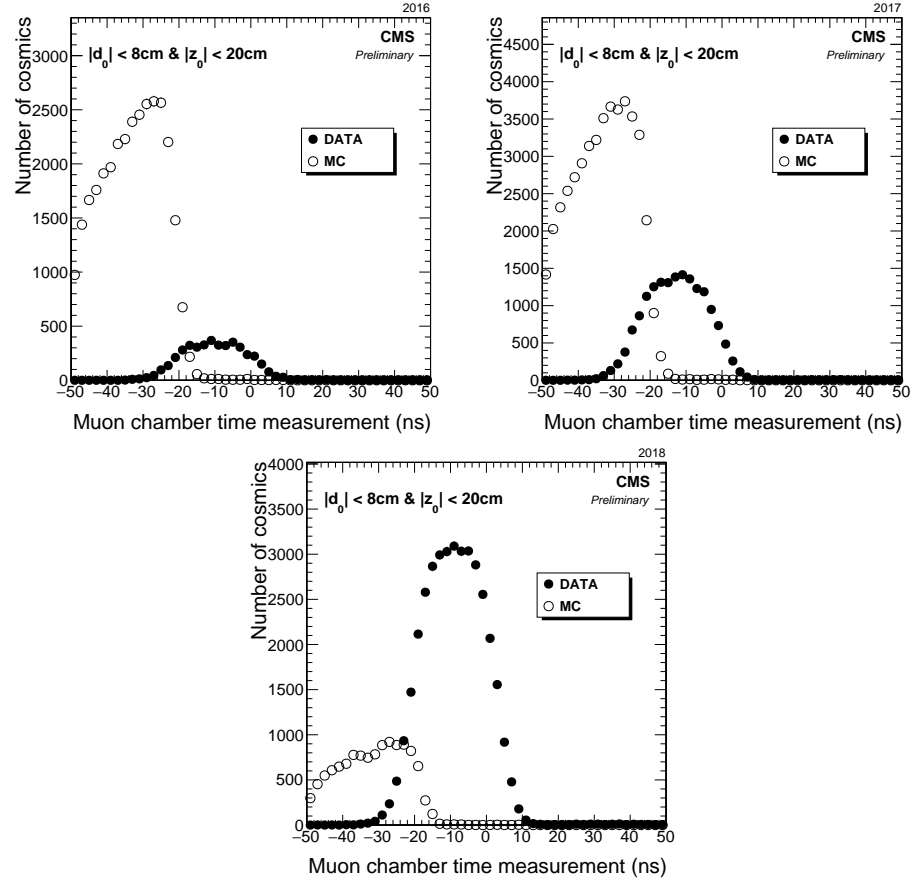


Figure C.1: Distribution of the arrival time of cosmic rays at their point of closest approach to the beamline as measured by the muon system in 2016 (top left), 2017 (top right), and 2018 (bottom) in data and simulation. Only cosmic ray muons with  $|d_0| < 8\text{ cm}$  and  $|z_0| < 20\text{ cm}$  are considered.

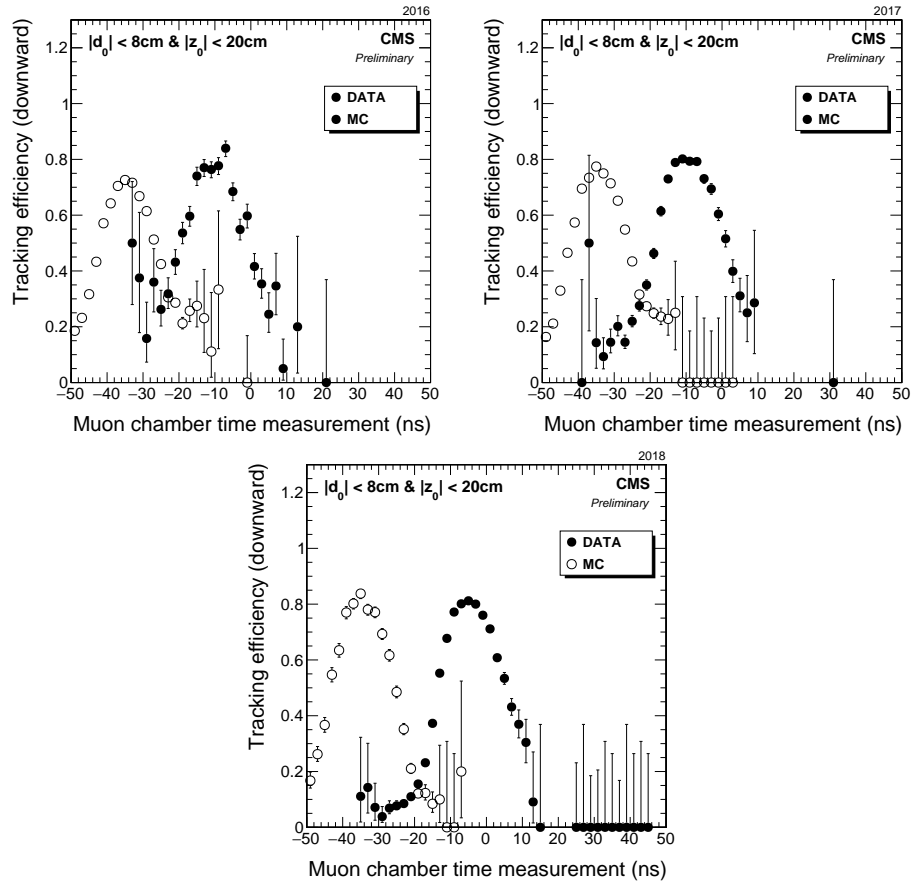


Figure C.2: Measured downward tracking efficiency versus cosmic ray muon arrival time in 2016 (top left), 2017 (top right), and 2018 (bottom) in data and simulation. Only cosmic ray muons with  $|d_0| < 8\text{ cm}$  and  $|z_0| < 20\text{ cm}$  are considered.

1698        The downward tracking efficiency is then measured using all selected one-leg  
 1699        muons that meet the timing requirements specified in Table C.1. The downward  
 1700        tracking efficiency as a function of transverse and longitudinal impact parameter is  
 1701        shown for all three years in Fig. C.3. The tracking efficiency is found to be nonzero  
 1702        out to at least 10 cm (30 cm) in transverse (longitudinal) impact parameter in all three  
 1703        years. We also note that removing the pixel-hit requirement increases this range to  
 1704        approximately 30 cm (50 cm).

1705        The results of Fig. C.3 are used to estimate a systematic uncertainty in the sim-  
 1706        ulated signal efficiency arising from the displaced tracking efficiency. A simulated  
 1707         $\tilde{t}\bar{t} \rightarrow \bar{l}b \bar{l}\bar{b}$  sample with a top squark mass of 1800 GeV and proper decay length  
 1708         $c\tau = 100$  cm is considered as it produces leptons with the largest impact parameters  
 1709        and therefore represents the most challenging scenario for the displaced track recon-  
 1710        struction. To accommodate the pixel hit requirements, only those events in which  
 1711        both top squarks decay within the volume of the pixel detector are considered. First,  
 1712        the transverse and longitudinal impact parameters of both leptons in this subset of  
 1713        signal events are noted. Next, a two-dimensional plot of tracking efficiency as a func-  
 1714        tion of the transverse and longitudinal impact parameters,  $\epsilon(|d_0|, |z_0|)$ , is produced  
 1715        from the cosmic ray muons in data and simulated cosmic ray events. Using this plot,  
 1716        the mean efficiency to reconstruct both lepton tracks in the simulated signal events  
 1717        is evaluated as:

$$\frac{1}{N} \sum_i \epsilon(|d_0|_i^{(1)}, |z_0|_i^{(1)}) \epsilon(|d_0|_i^{(2)}, |z_0|_i^{(2)}) \quad (\text{C.1})$$

1718        where the sum extends over the  $N$  events in the signal sample and the superscripts (1)  
 1719        and (2) denote the two leptons in each event. For each year, the relative systematic  
 1720        uncertainty in the efficiency to reconstruct both lepton tracks is then taken from

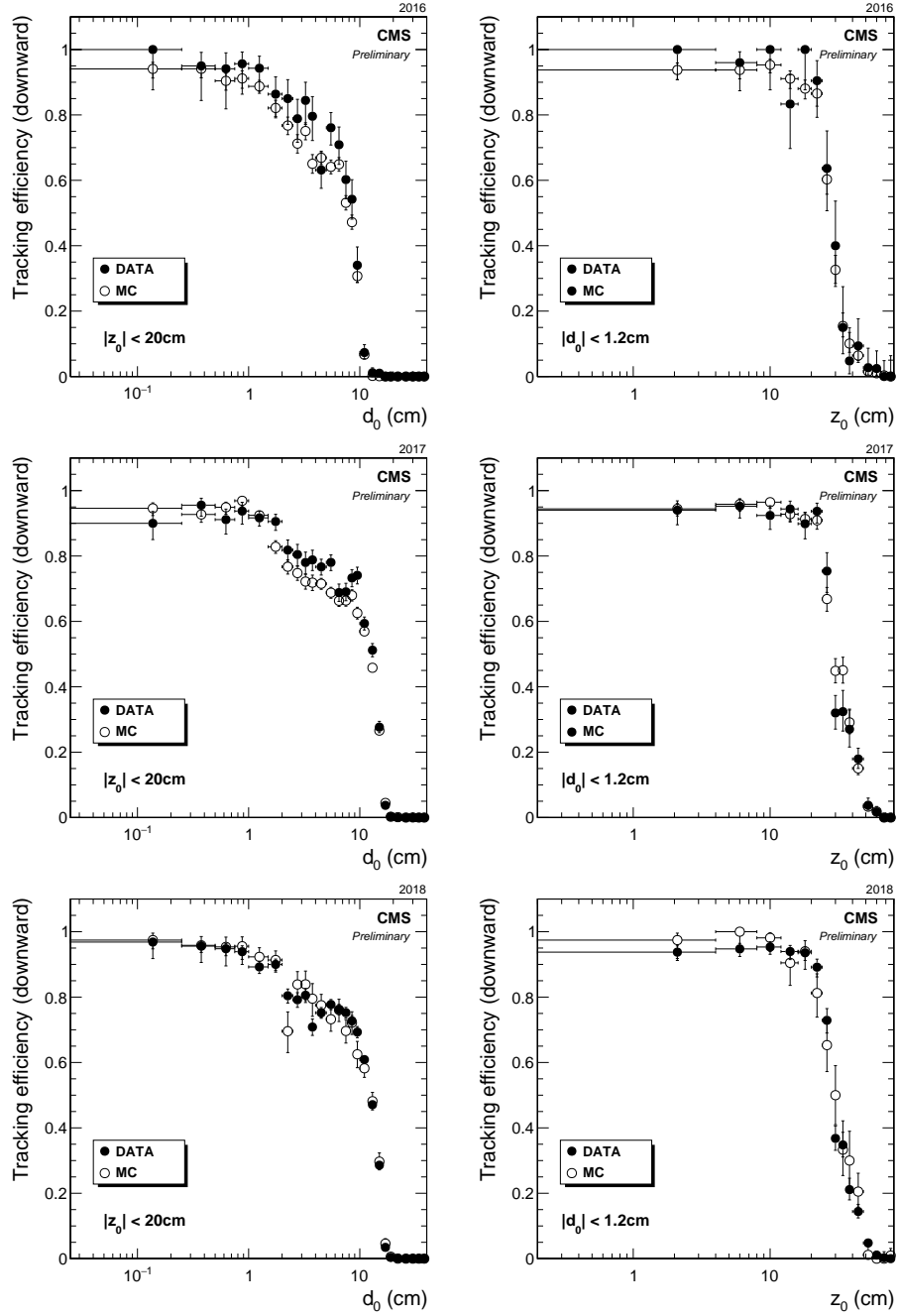


Figure C.3: Measured downward tracking efficiency in 2016 (top), 2017 (middle), and 2018 (bottom) versus transverse impact parameter (left) and longitudinal impact parameter (right) in data and simulation. The longitudinal (transverse) impact parameter is constrained to less than 20 cm (1.2 cm) when plotting against the transverse (longitudinal) impact parameter.

Table C.2: Mean measured efficiency to reconstruct both lepton tracks in simulated  $\tilde{t}\tilde{t} \rightarrow \bar{l}b\bar{l}b$  events in data and simulation and the resulting systematic uncertainty. The top squark mass and proper decay length are assumed to be 1800 GeV and 100 cm.

	2016	2017	2018
Efficiency in data	$57.5 \pm 2.1\%$	$55.3 \pm 1.1\%$	$56.1 \pm 0.7\%$
Efficiency in simulation	$50.3 \pm 1.0\%$	$52.3 \pm 0.7\%$	$57.5 \pm 1.1\%$
Systematic uncertainty	$14.1 \pm 4.3\%$	$5.8 \pm 2.3\%$	$2.4 \pm 2.2\%$

<sub>1721</sub> the ratio of the efficiencies in data and simulation. The resulting efficiencies and  
<sub>1722</sub> systematic uncertainties are listed in Table C.2.

## Bibliography

- [1] Summaries of cms cross section measurements. <https://twiki.cern.ch/twiki/bin/view/CMSPublic/PhysicsResultsCombined>. Accessed: 2021-04-04.
- [2] Cms supersymmetry physics results. <https://twiki.cern.ch/twiki/bin/view/CMSPublic/PhysicsResultsSUS>. Accessed: 2021-04-04.
- [3] Lyndon Evans and Philip Bryant. LHC machine. *Journal of Instrumentation*, 3(08):S08001–S08001, aug 2008.
- [4] Esma Mobs. The CERN accelerator complex - 2019. Complex des accélérateurs du CERN - 2019. Jul 2019. General Photo.
- [5] Jorg Wenninger. Operation and Configuration of the LHC in Run 2. Mar 2019.
- [6] AC Team. Diagram of an LHC dipole magnet. Schéma d'un aimant dipôle du LHC. Jun 1999.
- [7] Tai Sakuma. 3D SketchUp images of the CMS detector (120918). May 2016.
- [8] CMS Collaboration. The CMS experiment at the CERN LHC. The Compact Muon Solenoid experiment. *JINST*, 3:S08004. 361 p, 2008. Also published by CERN Geneva in 2010.
- [9] Run ii pixel performance plots for data and simulation. \textbf{https://lh c-commissioning.web.cern.ch/schedule/LHC-long-term.htm}. Accessed: 2021-04-04.
- [10] The Tracker Group of the CMS Collaboration. The CMS Phase-1 Pixel Detector Upgrade. *JINST*, 16(02):P02027, 2021.
- [11] CMS Collaboration. Observation of a new boson at a mass of 125 GeV with the CMS experiment at the LHC. *PLB*, 716:30, 2012.
- [12] CMS Collaboration. CMS Physics: Technical Design Report Volume 1: Detector Performance and Software. 2006. There is an error on cover due to a technical problem for some items.

- 1749 [13] CMS Collaboration. Particle-flow reconstruction and global event description  
1750 with the CMS detector. *JINST*, 12:P10003, 2017.
- 1751 [14] Image courtesy of Jamie Antonelli.
- 1752 [15] David J. Gross and Frank Wilczek. Asymptotically free gauge theories. i. *Phys.*  
1753 *Rev. D*, 8:3633–3652, Nov 1973.
- 1754 [16] H. Fritzsch, M. Gell-Mann, and H. Leutwyler. Advantages of the color octet  
1755 gluon picture. *Physics Letters B*, 47(4):365–368, 1973.
- 1756 [17] Steven Weinberg. A model of leptons. *Phys. Rev. Lett.*, 19:1264–1266, Nov 1967.
- 1757 [18] Jeffrey Goldstone, Abdus Salam, and Steven Weinberg. Broken symmetries.  
1758 *Phys. Rev.*, 127:965–970, Aug 1962.
- 1759 [19] F. Englert and R. Brout. Broken symmetry and the mass of gauge vector mesons.  
1760 *Phys. Rev. Lett.*, 13:321–323, Aug 1964.
- 1761 [20] Peter Ware Higgs. Broken symmetries, massless particles and gauge fields. *Phys.*  
1762 *Lett.*, 12:132–133, 1964.
- 1763 [21] G. S. Guralnik, C. R. Hagen, and T. W. B. Kibble. Global conservation laws  
1764 and massless particles. *Phys. Rev. Lett.*, 13:585–587, Nov 1964.
- 1765 [22] ATLAS Collaboration. Observation of a new particle in the search for the stan-  
1766 dard model Higgs boson with the ATLAS detector at the LHC. *PLB*, 716:1,  
1767 2012.
- 1768 [23] CMS Collaboration. Combined measurements of Higgs boson couplings in pro-  
1769 ton–proton collisions at  $\sqrt{s} = 13$  TeV. *Eur. Phys. J. C*, 79(5):421, 2019.
- 1770 [24] ATLAS Collaboration. Combined measurements of higgs boson production and  
1771 decay using up to  $80 \text{ fb}^{-1}$  of proton-proton collision data at  $\sqrt{s} = 13$  TeV  
1772 collected with the atlas experiment. *Phys. Rev. D*, 101:012002, Jan 2020.
- 1773 [25] Masataka Fukugita and P. J. E. Peebles. The cosmic energy inventory. *The*  
1774 *Astrophysical Journal*, 616(2):643–668, Dec 2004.
- 1775 [26] Gian Francesco Giudice. Naturally speaking: The naturalness criterion and  
1776 physics at the lhc. *Perspectives on LHC Physics*, page 155–178, Jun 2008.
- 1777 [27] Gerard ’t Hooft. Naturalness, chiral symmetry, and spontaneous chiral symmetry  
1778 breaking. *NATO Sci. Ser. B*, 59:135–157, 1980.

- 1779 [28] Nima Arkani–Hamed, Savas Dimopoulos, and Gia Dvali. The hierarchy problem  
1780 and new dimensions at a millimeter. *Physics Letters B*, 429(3-4):263–272, Jun  
1781 1998.
- 1782 [29] Stephen P. Martin. A supersymmetry primer. *Advanced Series on Directions in*  
1783 *High Energy Physics*, page 1–98, Jul 1998.
- 1784 [30] Nathaniel Craig. The state of supersymmetry after run i of the lhc, 2014.
- 1785 [31] Particle Data Group. Review of Particle Physics. *Progress of Theoretical and*  
1786 *Experimental Physics*, 2020(8), 08 2020. 083C01.
- 1787 [32] Zhen Liu and Brock Tweedie. The fate of long-lived superparticles with hadronic  
1788 decays after lhc run 1. *Journal of High Energy Physics*, 2015(6), Jun 2015.
- 1789 [33] W Kilian, T Plehn, P Richardson, and E Schmidt. Split Supersymmetry at  
1790 Colliders. *Eur. Phys. J. C*, 39(hep-ph/0408088. DESY-04-136. DESY-2004-136.  
1791 CERN-PH-TH-2004-144):229–243. 28 p, Oct 2004.
- 1792 [34] Frank E Paige and J Wells. Anomaly mediated SUSY breaking at the LHC.  
1793 Technical Report hep-ph/0001249, Jan 2000.
- 1794 [35] Peter W. Graham, David E. Kaplan, Surjeet Rajendran, and Prashant Saraswat.  
1795 Displaced Supersymmetry. *JHEP*, 07:149, 2012.
- 1796 [36] Lawrence J. Hall and Mahiko Suzuki. Explicit r-parity breaking in supersym-  
1797 metric models. *Nuclear Physics B*, 231(3):419–444, 1984.
- 1798 [37] Linear accelerator 2. Sep 2012.
- 1799 [38] The Proton Synchrotron Booster. Jul 2012.
- 1800 [39] Proton Synchrotron. 1959.
- 1801 [40] The Super Proton Synchrotron. Jan 2012.
- 1802 [41] CMS Collaboration. CMS Physics: Technical Design Report Volume 2: Physics  
1803 Performance. *J. Phys. G*, 34(CERN-LHCC-2006-021. CMS-TDR-8-2):995–1579.  
1804 669 p, 2007. revised version submitted on 2006-09-22 17:44:47.
- 1805 [42] Cms collaboration. <https://cms.cern/collaboration>. Accessed: 2021-03-28.
- 1806 [43] A et al. Dominguez. CMS Technical Design Report for the Pixel Detector Up-  
1807 grade. Technical Report CERN-LHCC-2012-016. CMS-TDR-11, Sep 2012.
- 1808 [44] Lea Michaela Caminada. Performance and Operation of the CMS Phase 1 Pixel  
1809 Detector. Technical Report CMS-CR-2018-067, CERN, Geneva, Jun 2018.

- 1810 [45] A.M. Sirunyan, A. Tumasyan, W. Adam, F. Ambrogi, E. Asilar, T. Bergauer,  
 1811 J. Brandstetter, E. Brondolin, M. Dragicevic, J. Erö, and et al. Performance of  
 1812 the cms muon detector and muon reconstruction with proton-proton collisions  
 1813 at  $\sqrt{s} = 13$  tev. *Journal of Instrumentation*, 13(06):P06015–P06015, Jun 2018.
- 1814 [46] L. Cadamuro. The cms level-1 trigger system for lhc run ii. *Journal of Instru-*  
 1815 *mentation*, 12(03):C03021, 2017.
- 1816 [47] W Adam, R Fröhwirth, A Strandlie, and T Todorov. Reconstruction of electrons  
 1817 with the gaussian-sum filter in the CMS tracker at the LHC. *Journal of Physics*  
 1818 *G: Nuclear and Particle Physics*, 31(9):N9–N20, jul 2005.
- 1819 [48] CMS Collaboration. Search for displaced supersymmetry in events with an elec-  
 1820 tron and a muon with large impact parameters. *Physical Review Letters*, 114(6),  
 1821 Feb 2015.
- 1822 [49] CMS Collaboration. Search for displaced leptons in the e-mu channel. Technical  
 1823 Report CMS-PAS-EXO-16-022, CERN, Geneva, 2016.
- 1824 [50] Juliette Alimena et al. Searching for long-lived particles beyond the standard  
 1825 model at the large hadron collider. *Journal of Physics G: Nuclear and Particle*  
 1826 *Physics*, 47(9):090501, sep 2020.
- 1827 [51] CMS Collaboration. Search for disappearing tracks in proton-proton collisions  
 1828 at  $s=13$ tev. *Physics Letters B*, 806:135502, Jul 2020.
- 1829 [52] CMS Collaboration. Search for long-lived particles using delayed photons in  
 1830 proton-proton collisions at  $s=13$ tev. *Physical Review D*, 100(11), Dec 2019.
- 1831 [53] CMS Collaboration. Search for long-lived particles using nonprompt jets and  
 1832 missing transverse momentum with proton-proton collisions at  $s=13$ tev. *Physics*  
 1833 *Letters B*, 797:134876, Oct 2019.
- 1834 [54] J. Alwall, R. Frederix, S. Frixione, V. Hirschi, F. Maltoni, O. Mattelaer, H. S.  
 1835 Shao, T. Stelzer, P. Torrielli, and M. Zaro. The automated computation of tree-  
 1836 level and next-to-leading order differential cross sections, and their matching to  
 1837 parton shower simulations. *JHEP*, 07:079, 2014.
- 1838 [55] Rikkert Frederix and Stefano Frixione. Merging meets matching in MC@NLO.  
 1839 *JHEP*, 12:061, 2012.
- 1840 [56] Johan Alwall et al. Comparative study of various algorithms for the merging  
 1841 of parton showers and matrix elements in hadronic collisions. *Eur. Phys. J. C*,  
 1842 53:473, 2008.

- 1843 [57] Stefano Frixione and Bryan R. Webber. Matching NLO QCD computations and  
1844 parton shower simulations. *JHEP*, 06:029, 2002.
- 1845 [58] Paolo Nason. A New method for combining NLO QCD with shower Monte Carlo  
1846 algorithms. *JHEP*, 11:040, 2004.
- 1847 [59] Stefano Frixione, Paolo Nason, and Carlo Oleari. Matching NLO QCD compu-  
1848 tations with Parton Shower simulations: the POWHEG method. *JHEP*, 11:070,  
1849 2007.
- 1850 [60] Simone Alioli, Paolo Nason, Carlo Oleari, and Emanuele Re. NLO vector-boson  
1851 production matched with shower in POWHEG. *JHEP*, 07:060, 2008.
- 1852 [61] Simone Alioli, Paolo Nason, Carlo Oleari, and Emanuele Re. A general frame-  
1853 work for implementing NLO calculations in shower Monte Carlo programs: the  
1854 POWHEG BOX. *JHEP*, 06:043, 2010.
- 1855 [62] Torbjörn Sjöstrand, Stefan Ask, Jesper R. Christiansen, Richard Corke, Nishita  
1856 Desai, Philip Ilten, Stephen Mrenna, Stefan Prestel, Christine O. Rasmussen, and  
1857 Peter Z. Skands. An introduction to PYTHIA 8.2. *Comput. Phys. Commun.*,  
1858 191:159, 2015.
- 1859 [63] Vardan Khachatryan et al. Event generator tunes obtained from underlying event  
1860 and multiparton scattering measurements. *Eur. Phys. J.*, C76(3):155, 2016.
- 1861 [64] CMS Collaboration. Extraction and validation of a new set of CMS PYTHIA8  
1862 tunes from underlying-event measurements. *EPJC*, 80:4, 2020.
- 1863 [65] Johan Alwall, A. Ballestrero, P. Bartalini, S. Belov, E. Boos, et al. A standard  
1864 format for Les Houches event files. *Comput. Phys. Commun.*, 176:300, 2007.
- 1865 [66] B.C. Allanach, M. Battaglia, G.A. Blair, Marcela S. Carena, A. De Roeck, et al.  
1866 The Snowmass points and slopes: Benchmarks for SUSY searches. *EPJC*, 25:113,  
1867 2002.
- 1868 [67] CMS Collaboration. Precision measurement of the structure of the CMS inner  
1869 tracking system using nuclear interactions. *JINST*, 13:P10034, 2018.
- 1870 [68] CMS Collaboration. Precision measurement of the structure of the CMS inner  
1871 tracking system using nuclear interactions with data collected in 2018. *CMS-  
1872 DP-2019-001*, 2019.
- 1873 [69] Jared A. Evans and Jessie Shelton. Long-lived staus and displaced leptons at  
1874 the LHC. *JHEP*, 04:056, 2016.

- 1875 [70] CMS Collaboration. CMS luminosity measurements for the 2016 data taking  
 1876 period. CMS Physics Analysis Summary CMS-PAS-LUM-17-001, 2017.
- 1877 [71] CMS Collaboration. CMS luminosity measurements for the 2017 data-taking  
 1878 period at  $\sqrt{s} = 13$  TeV. CMS Physics Analysis Summary CMS-PAS-LUM-17-  
 1879 004, 2018.
- 1880 [72] CMS Collaboration. CMS luminosity measurements for the 2018 data-taking  
 1881 period at  $\sqrt{s} = 13$  TeV. CMS Physics Analysis Summary CMS-PAS-LUM-18-  
 1882 002, 2018.
- 1883 [73] Lumi POG. Luminosity POG Twiki. [https://twiki.cern.ch/twiki/bin/vi  
 1884 ew/CMS/TWikiLUM#LumiComb](https://twiki.cern.ch/twiki/bin/view/CMS/TWikiLUM#LumiComb).
- 1885 [74] CMS Collaboration. Measurement of the inelastic proton-proton cross section at  
 1886  $\sqrt{s} = 13$  TeV. *JHEP*, 07:161, 2018.
- 1887 [75] Thomas Junk. Confidence level computation for combining searches with small  
 1888 statistics. *Nucl. Instrum. Meth. A*, 434:435, 1999.
- 1889 [76] A. L. Read. Presentation of search results: the  $CL_s$  technique. In *Durham  
 1890 IPPP Workshop: Advanced Statistical Techniques in Particle Physics*, page 2693,  
 1891 Durham, UK, March 2002. [J. Phys. G 28 (2002) 2693].
- 1892 [77] Glen Cowan, Kyle Cranmer, Eilam Gross, and Ofer Vitells. Asymptotic formulae  
 1893 for likelihood-based tests of new physics. *Eur. Phys. J. C*, 71:1554, 2011.
- 1894 [78] The ATLAS Collaboration, The CMS Collaboration, The LHC Higgs Combi-  
 1895 nation Group. Procedure for the LHC Higgs boson search combination in Summer  
 1896 2011. Technical Report CMS-NOTE-2011-005, ATL-PHYS-PUB-2011-11, 2011.
- 1897 [79] B Aa Petersen and C Schwick. Experiment Requests and Constraints for Run 3.  
 1898 Technical report, 2019.
- 1899 [80] Longer term lhc schedule. [https://lhc-commissioning.web.cern.ch/schedu  
 le/LHC-long-term.htm](https://lhc-commissioning.web.cern.ch/schedu<br/>
  1900 le/LHC-long-term.htm). Accessed: 2021-04-04.
- 1901 [81] Robert Bainbridge. Recording and reconstructing 10 billion unbiased b hadron  
 1902 decays in cms. *EPJ Web Conf.*, 245:01025, 2020.
- 1903 [82] W. Adam et al. The effect of highly ionising particles on the CMS silicon strip  
 1904 tracker. *Nucl. Instrum. Meth. A*, 543:463, 2005.
- 1905 [83] M J French, L L Jones, Q R Morrissey, A Neviani, R Turchetta, J R Fulcher,  
 1906 G Hall, E Noah, M Raymond, G Cervelli, P Moreira, and G Marseguerra. Design  
 1907 and results from the APV25, a deep sub-micron CMOS front-end chip for the  
 1908 CMS tracker. *Nucl. Instrum. Methods Phys. Res., A*, 466(2):359–65, 2001.

1909 [84] Data quality group. Documentation on how to produce JSON files. <https://twiki.cern.ch/twiki/bin/view/CMS/InstructionForJSONFileCreation>.  
1910

1911 [85] S. Agostinelli et al. Geant4—a simulation toolkit. *Nuclear Instruments and*  
1912 *Methods in Physics Research Section A: Accelerators, Spectrometers, Detectors*  
1913 *and Associated Equipment*, 506(3):250–303, 2003.